CWP-470
January 2004

Inversion of Gravity Data for Base Salt

Dongjie Cheng

— Master's Thesis —
Geophysics

Defended December 2003

Center for Wave Phenomena
Colorado School of Mines
Golden, Colorado 80401
(1) 303 273-3557

Abstract

The seismic method often has difficulties recovering the geometry of the base salt with steep flanks and diapiric roots because of the complex shape of salt and high impedance contrast across the salt boundary. This problem may lead to incorrect subsalt imaging and inaccurate interpretation of subsalt geological structures. Also, both acquisition and processing of 3D seismic data are expensive and time consuming. Gravity data can often help to construct the base salt. Previous researchers have developed practical methods for inverting gravity data to construct the base of salt. With the increased application of such methods, it is important to understand the factors that influence the final inversion result and its value for subsalt imaging. I address this issue from a practical viewpoint by examining the influence of errors in a set of assumed parameters commonly used in gravity inversions.

To achieve this goal, I first develop an algorithm for inverting gravity data to construct the base of salt. The inversion algorithm is based on Tikhonov regularization, in which an explicit model objective function is incorporated to ensure a final model consistent with all available information. The model parameter in the inversion is the surface defining the base of salt; I represent it by the logarithm of the salt thickness by assuming that the top salt is known.

In most inversion algorithms, the top of the salt and parts of the base of salt are assumed to be accurately imaged by seismic data. The density contrast of the salt body is also assumed to be known. Furthermore, I assume that the gravity data have been reduced so that any factors unrelated to the variation in base salt are removed. In practice, however, these assumptions will invariably have errors that will influence the inversion result. The errors so produced will in turn influence the seismic image of subsalt features.

I use a synthetic salt model to investigate the sensitivity of the inverted base salt to errors in the assumptions used in the gravity inversion and the resulting influence on subsalt imaging. I show that moderate perturbation in any of the prior information, e.g., top salt, known base salt and density contrast, can lead to large errors in the recovered shape of the base salt. Through tests on a 2D acoustic velocity model, the estimated error in subsalt imaging due to the erroneously inverted base salt shows that large error in the inverted base salt does not necessarily imply large error in subsalt imaging. Nevertheless, with errors in the error in the various assumptions, use of gravity inversion can improve subsalt imaging. Because the volume of gravity data generally is much smaller than that of 3D seismic data, gravity inversion costs far less than does the 3D seismic imaging method. By offering additional constraints on the base salt for seismic imaging, use of gravity inversion may speed up and improve the imaging process.

Table of Contents

Acknowledgments

I would like to express my deepest appreciation to my advisors, Dr. Yaoguo Li and Dr. Ken Larner, for their advice, encouragement and support. I specially want to thank Dr. Zhiming Li for his guidance during my summer intern in Unocal, 2002, when the research was started. I thank the members in the advisory committee, Dr. Ilya Tsvankin and Dr. Alex Kaufman for their guidance and encouragement. Also, I want to express my thanks to Dr. Terry Young for his friendly support during my study.

I gratefully acknowledge the Center for Wave Phenomena (CWP) and Gravity and Magnetics Research Consortium (GMRC) for financial and research support during my MS study. I thank Unocal for kindly letting me recode the computer programs for my research developed during my summer internship, 2002. I am greatly indebted to my friends in CWP for interesting discussions and help. I especially thank the CWP staff — Lela Webber, Michelle Szobody and Barbara McLenon — for their support.

My family is always important to me. A special thanks is expressed to my wife, Ms. Chuntao Huang, for her forever support.

Chapter 1

Introduction

Subsalt exploration for oil and gas is attractive in regions such as the Gulf of Mexico where 3D seismic prestack depth-migration can often image the base of salt well. At times, however, it has difficulties in recovering the geometry of the salt base beneath steep flanks, e.g., diapiric roots (e.g., Ratcliff et al., 1992; Ratcliff and Weber, 1997). The main reasons are the complexity of the seismic raypaths and the lack of sufficient seismic energy penetrating the salt because of the complex shape of salt and high impedance contrast with surrounding sediments. This problem may lead to poor imaging and inaccurate interpretation of subsalt geological structures. As illustrated in Figure 1.1, for example, the shape of the base salt may determine whether or not a potential trap exists beneath the salt. Also, Albertin et al. (1998) point out that the misplacement of the salt boundary may lead to false images of subsalt features. Another problem is that processing of 3D seismic data, in particular, 3D seismic prestack depth migration, which must be carried out iteratively, is costly. Perhaps complementary information to reduce the ambiguity in seismic images and help speed up the iterative migration process and model building would be beneficial. Gravity data often serve these purposes in the petroleum industry (e.g., Dejong et al., 2000).

Previous researchers have developed practical methods for inverting gravity data to construct the base of salt (e.g., Jorgensen et al., 2001; Routh et al., 2001). With the increased application of such methods, it is important to understand the factors that influence the final inversion result, in addition to commonly considered issues such as data quality and details of the inversion formulation. In general, we assume that those factors are known in formulating the algorithm, but they inevitably contain errors in practice. When an erroneous inverted base salt is used to define the salt model in subsalt imaging (e.g., Talwani and Kessinger, 1995), the accuracy and quality of the subsalt images is degraded. In this thesis, my goal is to understand the sensitivity of inverted base salt to errors in known factors and then how the subsalt imaging is influenced by the erroneously inverted base salt.

To achieve the goal, I first develop a 3D inversion algorithm that uses the vertical gravity anomaly, $g_z(x, y)$, as data and inverts for the base of salt by Tikhonov regularization (Tikhonov and Arsenin, 1977). The model parameter to be estimated in the inversion is the surface defining the base of salt. I introduce a logarithmic function to represent it. The study in this thesis is problem-dependent and I adopt a synthetic 3D salt model to emulate a salt body in deep water. Throughout the thesis, all the problems are tackled by working with this model.

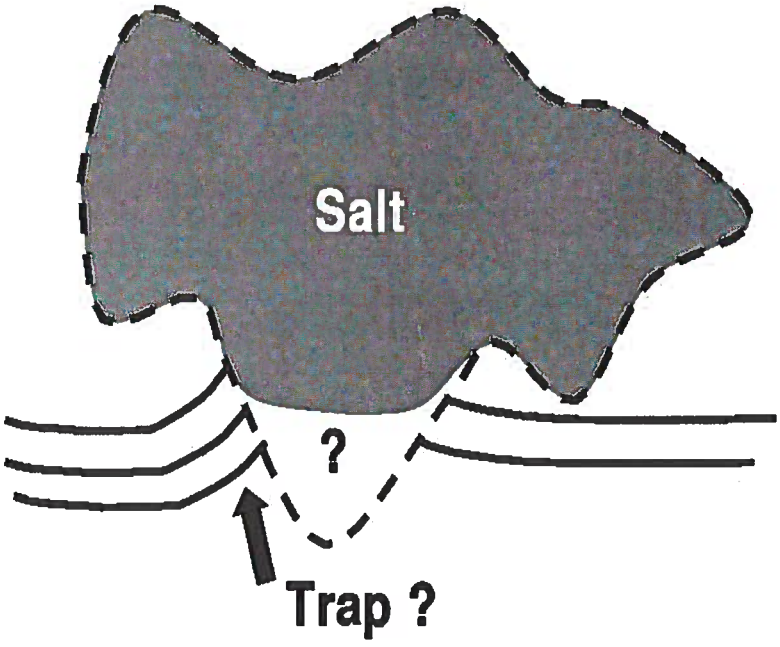

Figure 1.1. Motivation of gravity inversion for base salt. The dashed line delineates the boundary of the salt, and the solid lines represent the subsalt geological features. The region denoted by the question mark is unknown.

In most inversion algorithms, the top of the salt and a part of the base of salt are assumed to be accurately imaged by the seismic method. Also, the density of the background sediments, and thus the density contrast of the salt body, are assumed to be known (e.g., Routh et al., 2001). Furthermore, I assume that the gravity data have been reduced so that any factors unrelated to variation in base salt are removed. In practice, however, these assumptions invariably have errors that will influence the inversion result. Using the algorithm I developed, I investigate the influence of the assumed factors on the inverted base salt.

To date, little work has been done on the sensitivity of gravity inversion to these different assumptions. We can, however, exploit previous work in inverse theory to assess the uncertainties in linear inversion with respect to random data error. Wiggins et al. (1976) introduce an analytical approach to assess the posterior uncertainty of the model for linear problems. For nonlinear problems, Tarantola (1987) derives the covariance matrix and the resolution matrix for Bayesian inversion through a linearized approach. Meanwhile, Menke (1984) derives the same matrices by a different method. Alumbaugh and Newman(1999) apply this linearized approach to the appraisal of the image uncertainty in nonlinear electromagnetic inversion. In addition, Oldenburg and Li (1999) assess the sensitivity of the model solution to data quality. They quantify the uncertainty using the *depth of investigation index* (DOI), which is the difference between recovered models using different reference models. Small values of DOI, for example, imply lower uncertainty. To my knowledge, little work has been done on studying the sensitivity of base salt to prior information, and no work has been done on the influence of errors in presumed known factors in gravity inversion on subsalt imaging when erroneously inverted base salt is used in seismic imaging. My approach is based on linearized approximations following the works of Tarantola (1987), Menke (1984), and Alumbaugh and Newman (1999), and direct evaluation by simulations.

First, to estimate the sensitivity of estimated base-salt shape and position to the presence of random noise in gravity data, I compute estimates of standard deviation and bias in two ways: 1) I derive a linearized approximation for the covariance matrix and bias based on a Bayesian formalism (Tarantola, 1987); 2) in a more practical approach to evaluate the errors directly, I compute the sample standard deviation and bias through 100 realizations of inversion for the same noise level. In addition to the influence of random noise, I study the influence of coherent noise associated with geological noise, specially, inaccurate bathymetry correction. For the sensitivity to coherent data noise and prior information, I simulate possible errors in these factors, conducting the inversion with incorrectly specified bathymetry correction, presumed known positions of the base salt, top salt and density contrast. The error in the shape and position of base salt is directly evaluated by comparison with the best-estimated model in the absence of these four sources of error.

I then evaluate the sensitivity of subsalt seismic imaging to erroneously inverted base salt using a 2D acoustic velocity model through the 3D salt model. Two flat reflectors are added beneath the salt, and the distribution of velocity values with depth follows that of the SEG/EAGE salt model. I directly evaluate the error in subsalt imaging when using velocity models containing the shape of base salt recovered from the error-prone inversions, comparing with the best images and the correct image.

The thesis is organized as follows: Chapter 2 develops the algorithm for gravity inversion. I first formulate the algorithm directly using the base of salt as the model parameter; I then develop a modified algorithm that uses the logarithm of the scaled salt thickness as the model parameter. Chapter 3 examines the sensitivity of the inverted base salt to errors in the gravity data. Chapter 4 investigates the model sensitivity to errors in the prior information, including the presumed known part of base salt, top salt, and density contrast. Chapter 5 assesses the sensitivity of subsalt seismic imaging to error in the inverted base salt. I conclude the thesis with discussion in Chapter 6.

Chapter 2

Algorithm for gravity inversion

In this chapter, I develop an algorithm for inverting gravity data to estimate the shape of the base salt. The algorithm is based on the Tikhonov regularization technique. First, I formulate the inverse problem as an optimization and solve it by the Gauss-Newton method. Second, I introduce a logarithmic parameterization to enforce the physical condition that the base salt must lie below the top. I illustrate the algorithms using a synthetic example.

2.1 Formulation with linear parameterization

As shown in Figure 2.1, let $d_i = g_z(x_i, y_i), \quad i = 1, \cdots, N$ be the vertical gravity data, $h_t(x, y)$ and $h(x, y)$ be respectively the shape of the top and base of the salt body, and $\Delta\rho(z)$ be the density contrast between salt and the sedimentary host. I assume that $h_t(x, y)$ and $\Delta\rho(z)$ are known. I also assume that part of the base salt may be known and fixed during the inversion, termed as *High confidence zone* (HCZ). The inverse problem is then to construct the unknown part of $h(x, y)$ using the gravity anomaly and above-mentioned known information. The surface representing the base salt, $h(x, y)$, is the unknown to be recovered.

Traditionally, the goal of inversion is to find a model that best fits the data subject to a set of conditions. In the least-square approach, the objective function that measures the data misfit is given by

$$\phi_d = ||W_d(\vec{d} - \vec{d}_{obs})||_2^2, \tag{2.1}$$

where $\vec{d}$ is the vector of predicted data, $\vec{d}_{obs}$ denotes the observations, $||\cdot||_2^2$ denotes the squared L_2 norm of a vector, and W_d is a diagonal data-weighting matrix, whose elements are the reciprocal of estimated data standard derivations: $W_d(i, i) = \frac{1}{\sigma_i}$.

Gravity data, however, inevitably contain noise, and we have only a finite number of data measurements from which to recover the base-salt surface; therefore a model exactly fitting the data will over-interpret the data. In addition, inversion itself is an under-determined problem. Therefore, additional constraints need to be incorporated into the objective function. This is achieved here by Tikhonov regularization (Tikhonov and Arsenin, 1977), in which a weighted sum of data misfit and a model objective function is minimized.

Following Li and Oldenburg (1996), I define a model objective function to penalize the

structural complexity of the model as

$$\begin{aligned}\phi_m = \quad & \alpha_s \int_S [h(x,y) - h_{ref}(x,y)]^2 \, dxdy \\ & + \alpha_x \int_S \left\{ \frac{\partial [h(x,y) - h_{ref}(x,y)]}{\partial x} \right\}^2 dxdy \\ & + \alpha_y \int_S \left\{ \frac{\partial [h(x,y) - h_{ref}(x,y)]}{\partial y} \right\}^2 dxdy, \end{aligned} \tag{2.2}$$

where S is the horizontal area over which the unknown base salt is to be defined, and α_s, α_x and α_y are weighting factors that I fix as constants in the optimization process. α_s weights the difference between the objective model and the reference model, while α_x and α_y control the smoothness of the model in the x- and y-directions. h_{ref} denotes a reference model, which is usually formed by the base salt obtained from seismic images.

By Tikhonov regularization (Tikhonov and Arsenin, 1977), the objective function to be minimized is defined as

$$\phi = \phi_d + \beta \phi_m, \tag{2.3}$$

where ϕ_d is the data misfit, ϕ_m is the model objective function, and β is the regularization parameter. The choice of β depends on the noise level in the data.

To perform numerical computation, I discretize both the top and base salt into piecewise constant surfaces defined over a common set of contiguous rectangular cells within S. Such a discretization divides the salt body into a set of contiguous vertical prisms (Figure 2.2). The unknown model is represented as a vector of depth values within cells, $\vec{h} = (h_1, ..., h_M)^T$, where M defines the length of the model vector. Applying the discretization, the model objective function becomes

$$\begin{aligned}\phi_m \quad & = \alpha_s (\vec{h} - \vec{h}_{ref})^T W_s^T W_s (\vec{h} - \vec{h}_{ref}) + \\ & + \alpha_x (\vec{h} - \vec{h}_{ref})^T W_x^T W_x (\vec{h} - \vec{h}_{ref}) + \alpha_y (\vec{h} - \vec{h}_{ref})^T W_y^T W_y (\vec{h} - \vec{h}_{ref}) \\ & = (\vec{h} - \vec{h_{ref}})^T (\alpha_s W_s^T W_s + \alpha_x W_x^T W_x + \alpha_y W_y^T W_y)(\vec{h} - \vec{h}_{ref}) \\ & = (\vec{h} - \vec{h}_{ref})^T (W^T W)(\vec{h} - \vec{h}_{ref}), \end{aligned} \tag{2.4}$$

where the weighting matrices, W_s, W_x and W_y, describe the discrete form of the three operations in equation (2.2); each component of these three matrices is defined explicitly as follows. The simplest term is

$$W_s^T W_s = \Delta x \Delta y \mathbf{I},$$

where, $\mathbf{I}$ is the identity matrix, and Δx and Δy define the dimensions of model cells in the x- and y-directions.

The matrices W_x and W_y are dependent upon the geometric shape of the model area and are thus problem-dependent. The following example matrices assume a model rectangular mesh with uniform discretization, and the unknowns are ordered by rows in the

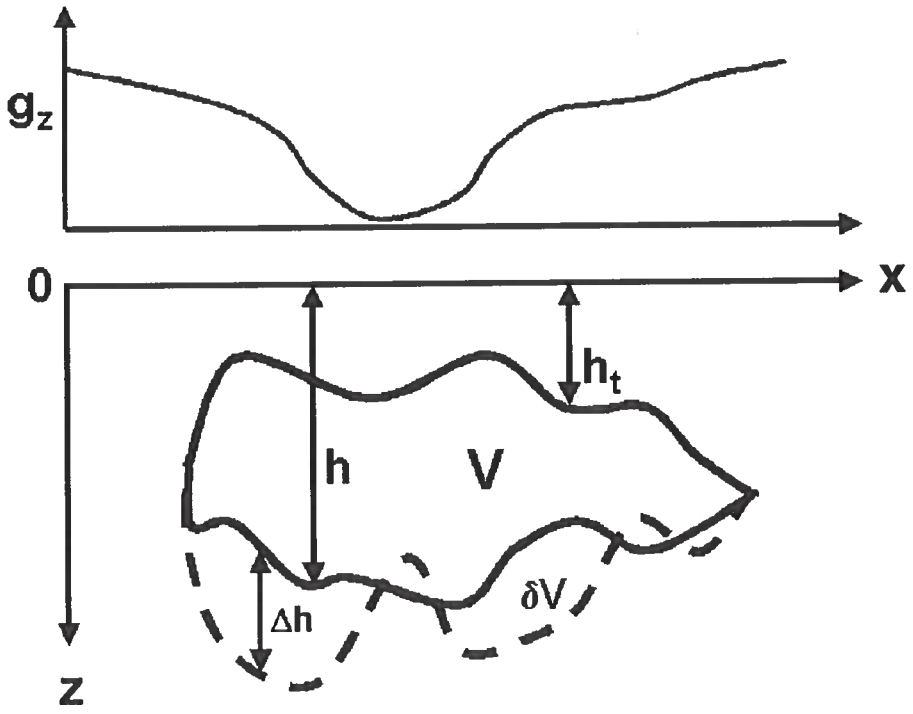

Figure 2.1. Problem definition. g_z denotes the gravity data; V represents the initial salt volume and δV represents the volume perturbation; h_t is the depth of top salt; h and δh are the initial depth and depth perturbation of base salt, respectively.

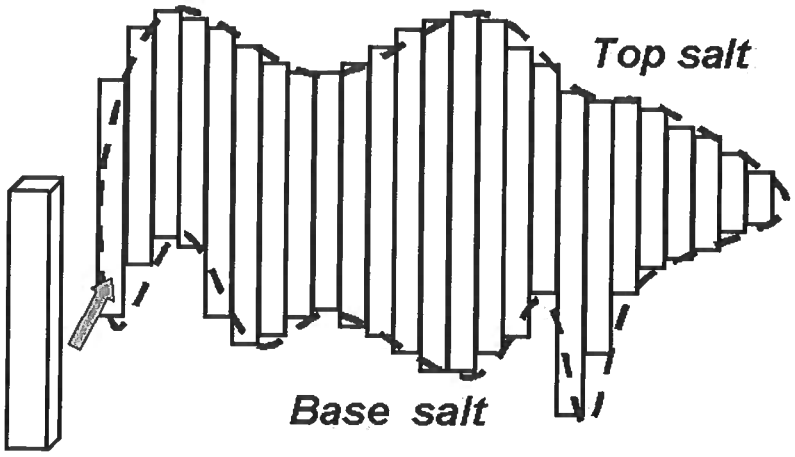

Figure 2.2. Two-dimensional illustration of the model discretization. The salt body is divided into a set of contiguous vertical prisms.

x-direction.

$$W_x^T W_x = \frac{\Delta y}{\Delta x} \begin{bmatrix} 2 & -1 & 0 & \dots & \dots \\ \vdots & \ddots & \dots & \dots & \dots \\ \vdots & -1 & 2 & -1 & \dots \\ \vdots & \vdots & \vdots & \ddots & \dots \\ \dots & \dots & \dots & -1 & 2 \end{bmatrix}. \tag{2.5}$$

$$W_y^T W_y = \frac{\Delta x}{\Delta y} \begin{bmatrix} \overbrace{\begin{matrix} 2 & 0 & -1 \\ 0 & \ddots & \dots \\ -1 & \dots & 2 \\ \vdots & \vdots & \vdots \\ \dots & \dots & -1 \end{matrix}}^{M_y} & \dots & \dots \\ \dots & \dots & \dots \\ \dots & -1 & \dots \\ \ddots & \dots & \\ \dots & 2 & \end{bmatrix}. \tag{2.6}$$

The matrix $W_x^T W_x$ and $W_y^T W_y$ are finite-difference approximations to the second-order derivative. Written in compact form, the model objective function becomes

$$\phi_m = ||W(\vec{h} - \vec{h}_{ref})||_2^2, \tag{2.7}$$

where $W^T W \equiv \alpha_s W_s^T W_s + \alpha_x W_x^T W_x + \alpha_y W_y^T W_y$. Since the weighting coefficients, α_s, α_x

and α_y are user-specified, if the smoothnesses of model in both the x- and y- directions are expected to be equal, a rule of thumb to define these three factors is as follows (UBC-GIF, 2002)

- $\frac{\alpha_x}{\alpha_s} > \Delta x^2$,
- $\frac{\alpha_y}{\alpha_s} > \Delta y^2$,

where Δx and Δy denote the cell size of the model. The discrete objective function in equation (2.3) can then be expressed as

$$\phi = ||W_d(\vec{d} - \vec{d}_{obs})||_2^2 + \beta||W(\vec{h} - \vec{h}_{ref})||_2^2, \tag{2.8}$$

where the predicted or modeled data vector $\vec{d}$ is a function of the depth vector, i.e., $\vec{d} = f(\vec{h})$.

Since the gravity observations on the surface constitute a nonlinear function of the depth of base salt, $\vec{h}$, the minimization of equation (2.8) is a nonlinear process. I apply the Gauss-Newton method to obtain the solution.

Let $\vec{h}^{(k)}$ be the depth of the base salt estimated in the kth iteration and

$$\vec{d}^{(k)} = f(\vec{h}^{(k)})$$

be the predicted data. In the $(k+1)$th iteration, the predicted data can be expressed as a Taylor series expansion:

$$f(\vec{h}^{(k)} + \delta\vec{h}^{(k+1)}) = f(\vec{h}^{(k)}) + G\delta\vec{h}^{(k+1)} + \mathbf{O}(\delta\vec{h}^{(k+1)}), \tag{2.9}$$

where $\mathbf{O}(\delta\vec{h}^{(k+1)})$ denotes the higher-order terms with respect to $\delta\vec{h}^{(k+1)}$, and G is the sensitivity matrix given by

$$G_{ij} = \frac{\partial d_i}{\partial h_j}, \tag{2.10}$$

which will be discussed later in this chapter. Substituting (2.9) into (2.8) and omitting higher order terms yields

$$\phi(\vec{h}^{(k)} + \delta\vec{h}^{(k+1)}) \approx ||W_d(\vec{d}^{(k)} + G\delta\vec{h}^{(k+1)} - \vec{d}_{obs})||_2^2 + \beta||W(\vec{h}^{(k)} + \delta\vec{h}^{(k+1)} - \vec{h}_0)||_2^2. \tag{2.11}$$

Differentiating (2.11) with respect to $\delta\vec{h}^{(k+1)}$ and setting to zero to search for the solution that minimizes (2.11), I obtain

$$(G^T W_d^T W_d G + \beta W^T W)\delta\vec{h}^{(k+1)} = W_d^T G^T W_d(\vec{d}_{obs} - \vec{d}^{(k)}) + \beta W^T W(\vec{h}_0 - \vec{h}^{(k)}). \tag{2.12}$$

Solving equation (2.12) for $\delta\vec{h}^{(k+1)}$, one obtains the model perturbation in the $(k+1)$th iteration

$$\delta\vec{h}^{(k+1)} = (G^T W_d^T W_d G + \beta W^T W)^{-1}\left[W_d^T G^T W_d(\vec{d}_{obs} - \vec{d}^{(k)}) + \beta W^T W(\vec{h}_0 - \vec{h}^{(k)})\right]. \tag{2.13}$$

To solve equation (2.13), I apply the method of conjugate gradients (CG) (Golub and Van Loan, 1989). The conjugate gradient method is an effective method for solving linear symmetric positive-definite systems. The method iteratively proceeds by generating an approximation of the solution, data residuals, and search directions until it converges. Only a small number of vectors need to be kept in memory and the number of iterations required to converge is generally far smaller than the number of unknowns, the CG method is appropriate for large-scale problems. In the following, I present an unpreconditioned approach of CG method used here.

For convenience, let us first rewrite equation (2.12) in compact form,

$$A\vec{x} = \vec{b}, \tag{2.14}$$

where

- $\vec{x} = \delta\vec{h}^{(k+1)}$,
- $A = G^T W_d^T W_d G + \beta W^T W$, and
- $\vec{b} = W_d^T G^T W_d(\vec{d}_{obs} - \vec{d}^{(k)}) + \beta W^T W(\vec{h}_0 - \vec{h}^{(k)})$.

The matrix $A \in R^{M\times M}$ is symmetric positive definite for $\beta > 0$, which can be approved as follows:
Given any $\vec{y} \in R^M$ and $\vec{y} \neq 0$,

$$\begin{aligned} \vec{y}^T A\vec{y} &= \vec{y}^T(G^T W_d^T W_d G + \beta W^T W)\vec{y} \\ &= \vec{y}^T G^T W_d^T W_d G\vec{y} + \vec{y}^T \beta W^T W\vec{y} \\ &= ||W_d G\vec{y}||_2^2 + \beta||W\vec{y}||_2^2 > 0. \end{aligned} \tag{2.15}$$

Therefore, the CG method is ideal for this problem. To solve equation (2.13), I adopt the sequence of steps shown in the pseudo-code below.

- `compute` $\vec{r}^{(0)} = \vec{b} - A\vec{x}^{(0)}$ with the initial guess $\vec{x}^{(0)}$ (e.g, $\vec{x}^{(0)} = \vec{0}$).
- `for` i=1,2,...
  $\theta_{i-1} = \vec{r}^{(i-1)^T}\vec{r}^{(i-1)}$
- `if` $i = 1$
  $\vec{p}^{(i)} = \vec{r}^{(0)}$
- `else`
  $\mu_{i-1} = \frac{\theta_{i-1}}{\theta_{i-2}}$
  $\vec{p}^{(i)} = \vec{r}^{(i-1)} + \mu_{i-1}\vec{p}^{(i-1)}$
- `endif`
  $\lambda_i = \frac{\theta_{i-1}}{\vec{p}^{(i)^T}\vec{q}^{(i)}}$
  $\vec{x}^{(i)} = \vec{x}^{(i-1)} + \lambda_i\vec{p}^{(i)}$

$\vec{r}^{(i)} = \vec{r}^{(i-1)} + \lambda_i \vec{q}^{(i)}$
with $\vec{q}^{(i)} = A\vec{p}^{(i)}$

- `check convergence`
- `end`

Because $A \in R^{M \times M}$ and M is large, if $A\vec{x}^{(0)}$ is carried out directly, one needs large memory to store the matrix A. To avoid this, I expand $A\vec{x_0}$ into the form

$$\begin{aligned} A\vec{x_0} &= (G^T W_d^T W_d G + \beta W^T W)\vec{x_0} \\ &= G^T W_d^T W_d G\vec{x_0} + \beta W^T W \vec{x_0}. \end{aligned}$$

$W^T W$ can be easily calculated since $W^T W$ is sparse. Moreover, since $G^T W_d^T W_d G\vec{x_0}$ can be calculated in three steps as $G^T(W_d^T W_d)(G\vec{x_0})$, we need store only matrix $G \in R^{N \times M}$ rather than A, saving the computer memory since N is generally much smaller than M.

The convergence is governed by the ratio between the L_2 norm of the data residual vector $\vec{r}^{(i)}$ and that of the input data vector $\vec{b}$; that is,

$$\nu \equiv \frac{||\vec{r}^{(i)}||_2}{||\vec{b}||_2} < \eta, \tag{2.16}$$

where η is some chosen small number.

Since the Gauss-Newton method uses a linear approximation to solve the nonlinear problem, although the search direction of the solution may be correct the solved step length could be wrong. In particular, it usually overestimates the model perturbation. I therefore update the base salt in the $(k+1)$th iteration with a limited step length (Murray, W. and Overton, 1979)

$$\vec{h}^{(k+1)} = \vec{h}^{(k)} + \alpha\delta\vec{h}^{(k+1)}, \tag{2.17}$$

where $0 < \alpha \leq 1$ limits the step length. α is determined by a line search to ensure that the objective function is monotonically decreasing.

This base salt solved in equation (2.13) is then used to calculate the predicted data for the $(k+1)$th iteration, and the inversion proceeds to the next iteration. The optimal solution is the model that minimizes equation (2.8). The process continues until convergence, with the condition of convergence defined as

$$\frac{|\phi^{(k+1)} - \phi^{(k)}|}{\phi^{(k)}} < \varepsilon,$$

where ε is a user-specified small number, and $\phi^{(k+1)}$ and $\phi^{(k)}$ denote the objective function in $(k+1)$th and kth iterations.

The above steps outline the minimization process for a fixed regularization parameter, β. Because results depend on the choice of β, we construct the model using a number of β values, so as to choose the solution that is most consistent with data-error estimate. I will discuss this in a later section.

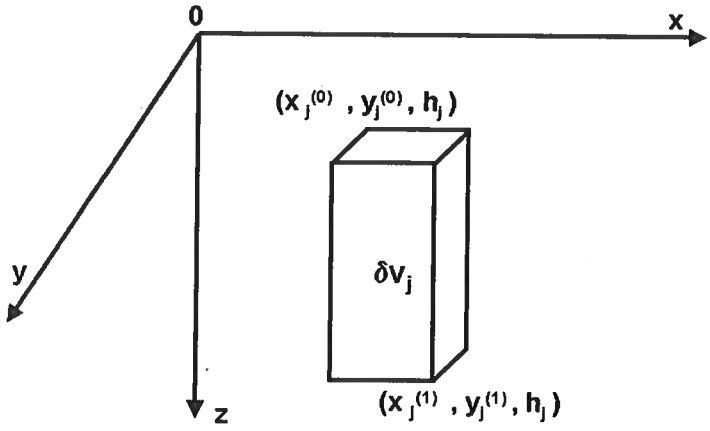

Figure 2.3. 3D view of the perturbation of a rectangular prism of the model.

2.2 Sensitivity matrix

One important quantity in the inversion is the sensitivity matrix G, the partial derivative of the data with respect to the model parameters. In this section, I derive an explicit expression for the sensitivity matrix shown in equation (2.10). To proceed, I adopt a right-handed Cartesian coordinate system, with the z-axis pointing downward. For a salt body with volume V in the subsurface (Figure 2.1), the vertical gravity anomaly at point i on the surface is defined as

$$g_z{}^{(i)} = \gamma \int_V \rho(x,y,z) \frac{\partial}{\partial z_i} \frac{1}{r} \, dx \, dy \, dz \,, \tag{2.18}$$

where $r \equiv \sqrt{(x_i - x)^2 + (y_i - y)^2 + (z_i - z)^2}$, and $\gamma \equiv 6.67 \cdot 10^{-11}$ m^3 /(kg $\cdot$ s^2). If we perturb only the depth of base salt $h(x,y)$ by $\delta h(x,y)$, then the data perturbation at the observation point i can be expressed as

$$\begin{aligned} \Delta g_z^{(i)} =& \gamma \int\int dx\, dy \int_{h_t(x,y)}^{h'(x,y)} \rho(x,y,z) \frac{\partial}{\partial z_i} \frac{1}{r} dz \\ & - \gamma \int\int dx\, dy \int_{h_t(x,y)}^{h(x,y)} \rho(x,y,z) \frac{\partial}{\partial z_i} \frac{1}{r} \, dz \\ =& \gamma \int\int dx\, dy \int_{h(x,y)}^{h'(x,y)} \rho(x,y,z) \frac{\partial}{\partial z_i} \frac{1}{r} dz, \end{aligned} \tag{2.19}$$

where $h'(x,y) \equiv h(x,y) + \delta h(x,y)$. In the discretized model, the salt body is a set of contiguous vertical prisms. For simplicity, let us focus on the jth rectangular prism perturbed by volume δV_j (Figure 2.3). Suppose the depth perturbation δh_j is small, and assume the density contrast is constant within δV_j. Also suppose that the depth of the base salt in this prism is h_j. Then, the data perturbation introduced at the ith point by model perturbation δh_j is the jth cell is given by

$$\delta g_z^{(ij)} = \gamma\rho \int\int dx\, dy \int_{h_j}^{h'_j} \frac{\partial}{\partial z_i}\frac{1}{r} dz\,.$$

Since $\frac{\partial}{\partial z_i}\frac{1}{r} = -\frac{\partial}{\partial z}\frac{1}{r}$, we have

$$\delta g_z^{(ij)} = -\gamma\rho \int\int \frac{1}{r}\Big|_{h_j}^{h'_j} dxdy.$$

For convenience, let $p = \frac{1}{r}$. Performing Taylor series expansion, we have

$$\begin{aligned}
\delta g_z^{(ij)} \quad &\approx -\gamma\rho \int\int \left(p(h_j) + \frac{\partial p}{\partial z}|_{z=h_j} \cdot \delta h_j - p(h_j) \right) dxdy \\
&= -\gamma\rho \int\int \frac{\partial p}{\partial z}|_{z=h_j} \cdot \delta h_j \, dxdy \\
&= \left[\gamma\rho \int\int \left(\frac{\partial}{\partial z_i}\frac{1}{r}|_{z=h_j} \right) dxdy \right] \cdot \delta h_j\,. \qquad (2.20)
\end{aligned}$$

According to the definition, the vertical gravity gradient T_{zz} at the ith observation point on the surface produced by a rectangular prism k having constant density contrast ρ can be expressed as

$$\begin{aligned}
T_{zz}^{(ik)} \quad &= \frac{\partial g_z^{(ik)}}{\partial z_i} \\
&= -\gamma\rho \int\int \frac{\partial}{\partial z_i}\frac{1}{r}\Big|_{h_t^{(k)}}^{h_b^{(k)}} \cdot dxdy, \qquad (2.21)
\end{aligned}$$

where h_t and h_b denote the depth of the top and the base, respectively.

Letting $h_b^{(k)} \to \infty$ and $h_t^{(k)} \to h_j$ in (2.21) yields

$$T_{zz}^{(ik)} \quad = \gamma\rho \int\int \frac{\partial}{\partial z_i}\frac{1}{r}\Big|_{z=h_j} dxdy. \qquad (2.22)$$

Comparing equation (2.22) with equation (2.20), we note that the term inside the square brackets in equation (2.20) is identical to T_{zz} in (2.22). Therefore, interestingly, the sensitivity of the gravity anomaly with respect to the base salt is given by the vertical gravity gradient produced by a rectangular prism whose top is the base salt and whose depth extent

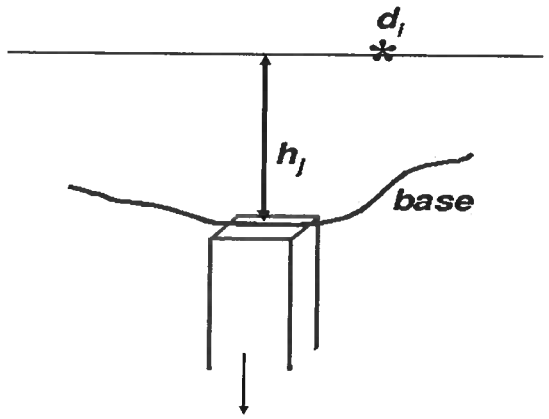

Figure 2.4. The equivalence of the sensitivity to the gravity gradient.

is infinite (Figure 2.4). That is

$$\frac{\partial g_z^{(i)}}{h_j} = T_{zz}^{(ik)}. \tag{2.23}$$

2.3 Logarithmic parameterization

The algorithm using linear parameterization without constraint can lead to the unacceptable result that the inverted base of salt lies above the top salt. For small β, this problem can be severe. As illustrated in Figure 2.5, we could obtain a rapidly oscillating perturbation with large amplitude when β is small. When added to a current model to update it, the updated model could have the base salt shallower than the top salt. Several approaches are available to deal with this problem.

1) Truncate the portion of model that lies above the top salt. This is equivalent to changing the search direction at each iteration of inversion, but could lead to poor convergence.

2) Adopt a new parameterization using a transformed model that naturally ensures a physically plausible method. This is achieved by using a logarithmic parameterization.

3) Apply an inequality constraint on the model. This method has been used widely, but usually incurs a large increase in computational complexity.

I adopt the second option here by using the logarithm of scaled depth difference between the top salt and the base salt as the model parameter to be recovered,

$$m(x,y) = \ln(\frac{h(x,y) - h_t(x,y)}{\tilde{h_0}}), \tag{2.24}$$

where, again, h and h_t are the depth of base salt and top salt, respectively. $\tilde{h_0}$ is an arbitrary constant. The base of salt is thus given by

$$h(x,y) = \tilde{h_0} e^{m(x,y)} + h_t(x,y). \tag{2.25}$$

Working with this transformed model ensures the natural condition that the recovered base of salt unequivocally lies below the top salt. No additional bound constraint is needed. Accordingly, the objective function becomes

$$\phi = ||W_d(\vec{d} - \vec{d}_{obs})||_2^2 + \beta||W(\vec{m} - \vec{m}_{ref})||_2^2, \tag{2.26}$$

where $\vec{m}_{ref}$ denotes the reference model, given by $\vec{m}_{ref}(x,y) = \log(\frac{h_{ref}(x,y) - h_t(x,y)}{\tilde{h_0}})$. Correspondingly, the iterative solution for model perturbation in the $(k+1)$th iteration has a form similar to that of equation (2.13); i.e.,

$$\delta\vec{m}^{(k+1)} = (J^T W_d^T W_d J + \beta W^T W)^{-1} \left[J^T W_d^T (\vec{d}_{obs} - \vec{d}^{(k)}) + \beta W^T W (\vec{m}_{ref} - \vec{m}^{(k)}) \right], \tag{2.27}$$

where J denotes the sensitivity matrix. Each element of the sensitivity matrix J_{ij} can be expressed as

$$J_{ij} \equiv \frac{\partial d_i}{\partial m_j} = \frac{\partial h_j}{\partial m_j} \cdot \frac{\partial d_i}{\partial h_j}. \tag{2.28}$$

From (2.25), we can derive that

$$\frac{\partial h(x,y)}{\partial m(x,y)} = \tilde{h_0} e^{m(x,y)} = h(x,y) - h_t(x,y). \tag{2.29}$$

Equation (2.28) thus becomes

$$J_{ij} \equiv \frac{\partial d_i}{\partial m_j} = (h_j - h_{tj})\, G_{ij}, \tag{2.30}$$

or

$$J = GH, \tag{2.31}$$

where $H = \mathrm{diag}\{\vec{h}_j - \vec{h}_{tj}\}$. The logarithmic parameterization is used widely in electrical and magnetic geophysics, commonly to ensure the positivity of recovered conductivity (e.g., Oldenburg and Li, 1994). Kim et al. (1999) suggest a method for model parameterization, which imposes more general bound constraints using prior knowledge about the upper and

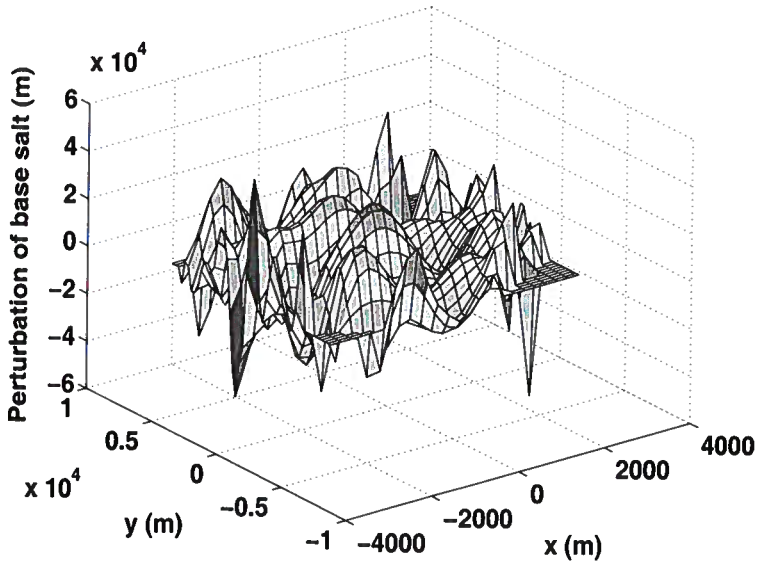

Figure 2.5. The recovered perturbation of base salt using a small value of β 10^{-12}.

lower limits of a model. For the depth of the salt, we can define the model parameter as

$$m(x,y) = \log\left(\frac{h(x,y) - h_1(x,y)}{h_2(x,y) - h(x,y)}\right), \tag{2.32}$$

where,

$$h_1(x,y) < h(x,y) < h_2(x,y).$$

Here $h(x,y)$ represents the base salt, and $h_1(x,y)$ and $h_2(x,y)$ represents the lower and upper limits of base salt respectively. The depth of base salt $h(x,y)$ is given by

$$h(x,y) = \frac{h_2(x,y)e^{m(x,y)} + h_1(x,y)}{1 + e^{m(x,y)}}. \tag{2.33}$$

For this parameterizing, I derive the sensitivity matrix following the method used to obtain equation (2.28). First, taking the derivative of $h(x,y)$ with respect to $m(x,y)$ in equation (2.33) yields

$$\frac{\partial h(x,y)}{\partial m(x,y)} = \frac{(h(x,y) - h_1(x,y))(h_2(x,y) - h(x,y))}{h_2(x,y) - h_1(x,y)}. \tag{2.34}$$

Let J be the sensitivity matrix; then

$$J_{ij} = \frac{\partial d_i}{\partial m_j} = \frac{\partial h_j}{\partial m_j} \cdot \frac{\partial d_i}{\partial h_j} = \frac{(h_j - h_{1j})(h_{2j} - h_j)}{h_{2j} - h_{1j}} G_{ij}. \tag{2.35}$$

The problem can again be solved by equation (2.27).

Although equation (2.32) gives a more general parameterization, it is difficult to specify geophysically reasonable upper and lower limits for this synthetic model with synthetic data. Therefore, I use the logarithmic parameterization in equation (2.24) hereafter.

2.4 Regularization parameters

As in any inversion, the criterion for choosing an optimal regularization parameter is crucial. I have used two approaches: (1) discrepancy principle and (2) L-curve criterion. In the following, I discuss these two methods separately.

2.4.1 Discrepancy principle

Matrix W_d in (2.1) is specified to be a diagonal matrix whose ith element is the reciprocal of the standard deviation of the ith datum. Therefore, assuming that the contaminating noise is independent and Gaussian with zero mean, makes ϕ_d a χ^2 variable with N degrees of freedom, and its expected value is $E(\chi^2) = N$. This provides a target misfit for the inversion, i.e., a model satisfying $E(\phi_d) = N$ is the objective solution. The χ^2 criterion is difficult to apply for this problem, however, because

(1) In practice, we seldom have knowledge of the standard deviation of the data.

(2) Residual geological noise, such as bathymetry error, is often present in the data. Such noise leads to correlated errors in the data and their full covariance matrix cannot be estimated easily.

Therefore, it would be inappropriate to adopt the discrepancy principle for this inverse problem.

2.4.2 L-curve criterion

The L-curve approach (Hansen, 1992) is a robust criterion based on the trade-off between the data misfit and the model objective function. According to Lawson and Hanson (1974), when plotted on a log-log scale the curve of the model objective function as a function of the data misfit can have an obvious corner:

- For regularization parameter values β larger than that of this corner point, the model objective function does not change dramatically, while the data misfit does.
- On the other hand, if the regularization parameter decreases beyond this point, the model objective function increases rapidly, but the data misfit decreases little.

The regularization parameter responsible for the corner point is judged to be the best regularization parameter, and the corresponding model is selected as the optimal solution. Searching for the best regularization parameter can be accomplished automatically because

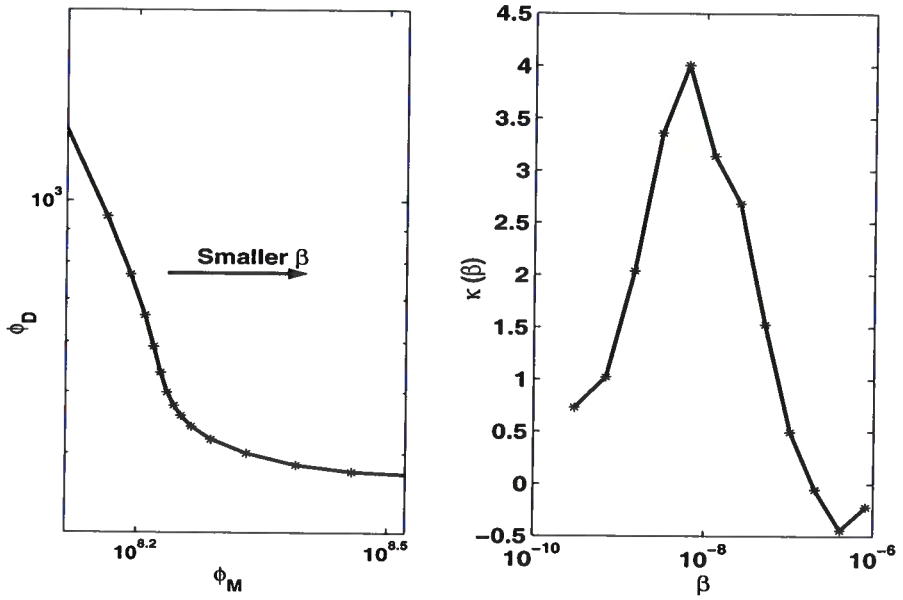

Figure 2.6. Tikhonov curve and its curvature as a function of β. The optimal solution is the model corresponding to the β value for which the curvature is maximum.

the curvature of the Tikhonov curve reaches the maximum at the corner. The curvature of the Tikhonov curve is defined as (e.g., Li and Oldenburg, 1999)

$$\kappa(\beta) = \frac{\varphi_d' \varphi_m'' - \varphi_m' \varphi_d''}{\left[(\varphi_d')^2 + (\varphi_m')^2\right]^{\frac{3}{2}}}, \tag{2.36}$$

where $\varphi_d = \log(\phi_d)$, $\varphi_m = \log(\phi_m)$, and symbols $'$ and $''$ denote the first and second derivatives with respect to β. Therefore, to carry out the inversion, one need only seek the maximum curvature of the Tikhonov curve. Figure 2.6 shows an example of a Tikhonov curve and its curvature as a function of β. The point of maximum curvature representing the optimal solution clearly seen in this example.

Since the data error in most practical applications is unknown, the L-curve is a better choice than is use of the discrepancy principle. I therefore have chosen to use this criterion in the remainder of the thesis.

Although the L-curve criterion was originally developed for linear problems, it can be applied to non-linear problems in two ways.

L-curve applied to the complete solution for a set of β's This is a direct approach for regularized inverse problems. Starting with a reasonably large value of β, the iterative algorithm with logarithmic parameterization derived in Section 2.1 is carried out for a set of β values. Correspondingly, a set of ϕ_d and ϕ_m values are computed at the

solution for each β. The optimal model is then obtained by the L-curve criterion. Specifying a set of β values, the following steps define the flow of implementation:

1 Let $k = 0$ define an initial regularization parameter, β_0, an initial model $\vec{m}_0$, and a reference model $\vec{m}_{ref}$.

2 Compute the value of the right-hand side of equation (2.12) in the kth iteration.

3 Solve equation (2.12) with the conjugate gradient method.

4 Linearly search for a step length α that satisfies $\phi_k < \phi_{k-1}$. The predicted data for each model and value of α are computed nonlinearly to obtain the value of the objective function.

5 If the convergence condition in (2.18) is not met, proceed to the $(k+1)$th iteration by continuing the iteration from step (2). Otherwise, stop the iteration. Set $\vec{m}_0 = \vec{m}_k$; decrease the value of β, and start over from step (1). Stop when the process has been followed for all β values in the specified step.

6 Find the optimal model using the L-curve criterion.

Dynamically choose β at each iteration Li and Oldenburg (1999) present an L-curve-based algorithm different from the one above. Instead of solving the problem completely for β, this method dynamically picks the best β value from the L-curve at each iteration of linearized minimization. Given the series of β's, this algorithm can be carried out in the following steps:

1 For $k = 0$, define an initial model $\vec{m}_0$ and a reference model $\vec{m}_{ref}$. Specify a set of β values, i.e., $\beta_1, \cdots, \beta_n$.

2 Compute the value of right hand side of equation (2.12) in the kth iteration.

3 Solve equation (2.12) with the conjugate gradient method for each β value.

4 Compute the values of linearized data misfit and model objective functions in the kth iteration for all β values. The linearized data misfit and model objective functions are given by

$$\tilde{\phi}_d^{(k+1)} = ||W_d(\Delta\vec{d}_{obs}^{(k+1)} - \Delta\vec{d}^{(k+1)})||_2^2, \tag{2.37}$$

where,

$$\Delta\vec{d}_{obs}^{(k+1)} = \vec{d}_{obs} - \vec{d}^{(k)},$$
$$\Delta\vec{d}^{(k+1)} = G\Delta\vec{m}^{(k+1)}.$$

$$\tilde{\phi}_m^{(k+1)} = (\vec{m}^{(k)} + \Delta\vec{m}^{(k+1)} - \vec{m}_{ref})^T W^T W(\vec{m}^{(k)} + \Delta\vec{m}^{(k+1)} - \vec{m}_{ref}) \tag{2.38}$$

5 Find the optimal model using the L-curve criterion and solve the linear equation.

6 Compute the predicted data for the optimal model by full forward modeling and check the convergence condition defined in (2.18). If the criterion is met, stop the computation. Otherwise, return to step (2).

Of these two approaches, the second method is more efficient. Through the *complete-β* method, one needs to perform full forward modeling in each iteration for every β to obtain the objective functions, and a full inverse solution must be obtained for each β. In the *dynamic-β* method, the regularization parameter is searched linearly. One need carry out full forward modeling only once in each iteration after the best β has been obtained. Because this latter method costs much less than the first one, I choose the dynamic-β method to search for the regularization parameter.

2.5 Numerical example

To illustrate the performance of the algorithm, I use the synthetic salt model shown in Figure 2.7. The density contrast (Figure 2.8) varies in the vertical direction only, and the model is assumed to lie below the nil-zone, where the density contrast between the salt and the sediments is close to zero. Therefore the salt body has a negative density contrast that increases in magnitude with depth. To simulate observed data, I generate 400 observations and contaminate them with Gaussian random noise having a standard deviation of 0.1 mGal. These data are shown in gray-scale contours in Figure 2.9. To emulate field data, I assume that the part of the base of salt shown by the gray contours in Figure 2.10 is known as the high confidence zone (HCZ). The unknown model to be recovered is defined over the central region in Figure 2.10. The base of the salt in the reference model (also initial model) has a 4000-m constant depth so the maximum difference between the true and the reference model is 1500 m. The top and the base of salt are discretized into 250-m square cells, and I choose $\alpha_s = 10^{-4}$, $\alpha_x = \alpha_y = 50$, according to the rules described in Section 2.1. In addition, to evaluate the difference between the two algorithms deriving β by different methods, I carry out two inversions applying the L-curve criterion in the two different ways.

Figure 2.11 shows the recovered model, using the complete-β method. The horizontal plane through the model shows the depth of the base salt in the initial model. The recovered model has the base salt extended downward and closer to the true position of the base. A clearer view about the recovered model can be seen in Figure 2.12, in which a contour map shows the difference between the true model and the recovered model.

Also, I apply the dynamic-β method on the same model and the same data under same conditions. The best obtained β in each iteration turns out to be the same: 1.28×10^{-1}, which shares the same values of the best β obtained using the complete β method. As shown Figure 2.12, the difference between the inverted solutions using two different methods has a maximum error of only 7 m. making the outcome from these two algorithms comparable. The latter method, however, is more efficient, requiring about only half the computation time.

To illustrate further the efficiency of the method using the dynamic-β approach, I carry out another experiment by not fixing a HCZ in the inversion. Now a larger region of base salt needs to be recovered, requiring that number of cells increases from 507 to 1010. Again, I perform inversions using the two different algorithms. Figure 2.14 shows the difference between the recovered depths using two different algorithms. The maximum error here is only 0.8 m, and the CPU time is reduced from 50 minutes to 8 minutes when the dynamic-β approach is used. In general, the larger the problem, the more the saving produced by the dynamic-β method.

2.6 Summary

In this chapter, I have developed an algorithm to perform inversion of gravity data for base salt. The numerical example shows that this algorithm could improve the definition of shape of the base salt. Also, as shown in Figure 5.13 in Chapter 5, using the recovered base salt in Figure 2.11 produces 2D comparable quality of subsalt seismic image to that using the true salt model, based on a 2D synthetic velocity model through the 3D salt model. Inversion with this algorithm, thus, could give models that aid in seismic imaging.

The algorithm that uses the logarithmic parameterization and chooses β dynamically based on the L-curve criterion turns out to be a good combination that is numerically stable and computationally efficient.

The result from the first numerical example can be considered as the best model from the inversion since all the assumptions made are correct, with modest random error included in the data. This model is used as the basis for comparisons in the sensitivity studies treated in Chapter 4.

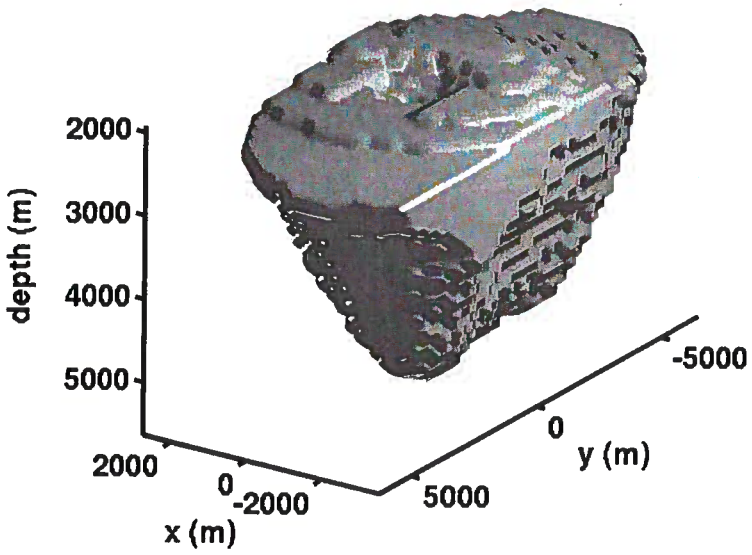

Figure 2.7. 3D view of the true salt model. The staircase appearance reflects the model discretization used in the inversion.

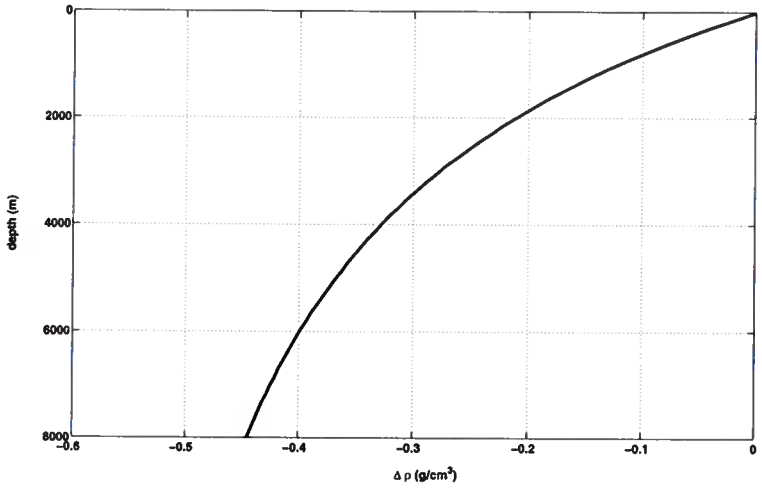

Figure 2.8. Curve of the density contrast between the salt and the sedimentary host. The density contrast here varies only in the vertical direction.

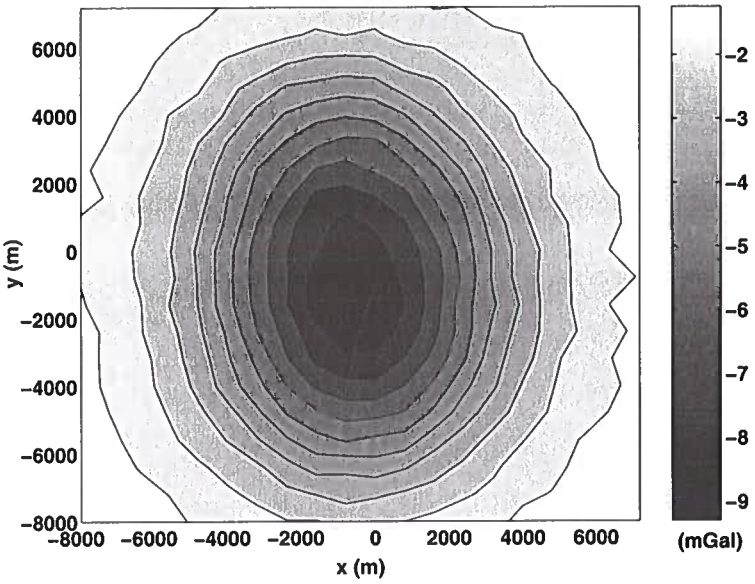

Figure 2.9. Synthetic gravity data contaminated with Gaussian noise whose standard deviation is 0.1 mGal, i.e., about 1% of the maximum size of the gravity anomaly.

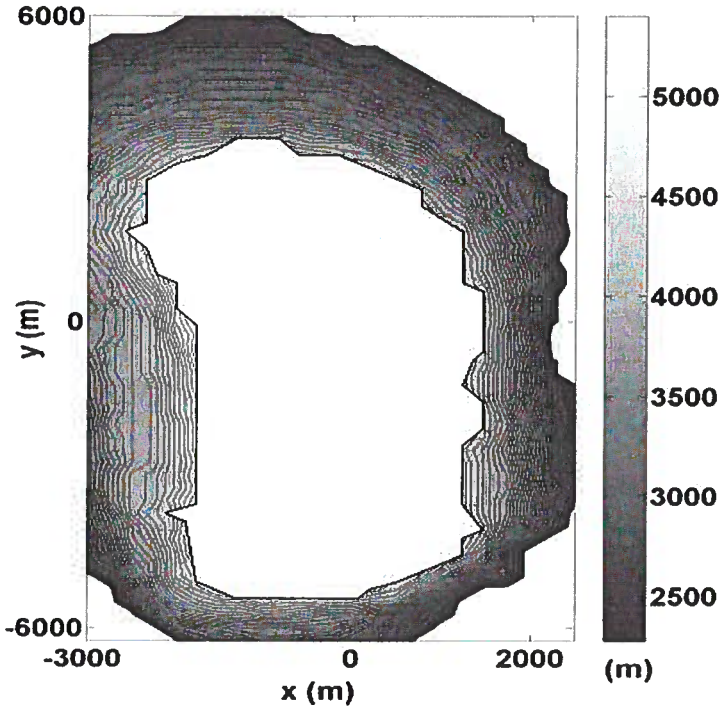

Figure 2.10. Plan view of base salt in which the contoured region shows the known portion of the base of salt while the blank region in the center is the area of unknown base of salt to be recovered from the inversion. The region of known base of salt is the HCZ.

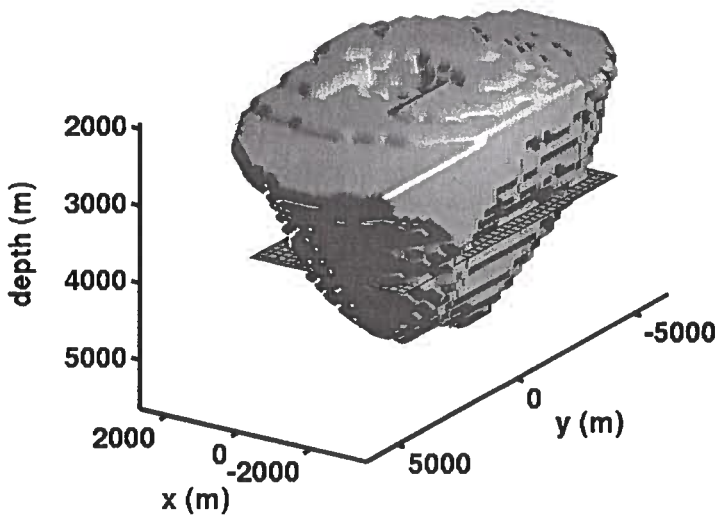

Figure 2.11. 3D view of the recovered model. Compared with the structure of the true model in Figure 2.7, the base salt is extended downward toward the correct base salt from the reference base salt, which is represented by the horizontal plane through the salt body.

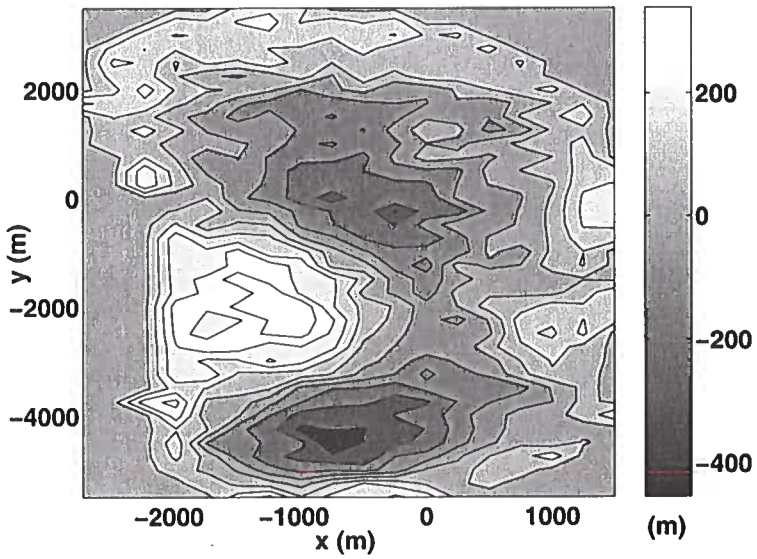

Figure 2.12. Contour map showing the difference between the depth of the true and recovered base salt. The maximum error is 450 m, while the RMS error is approximately 170 m.

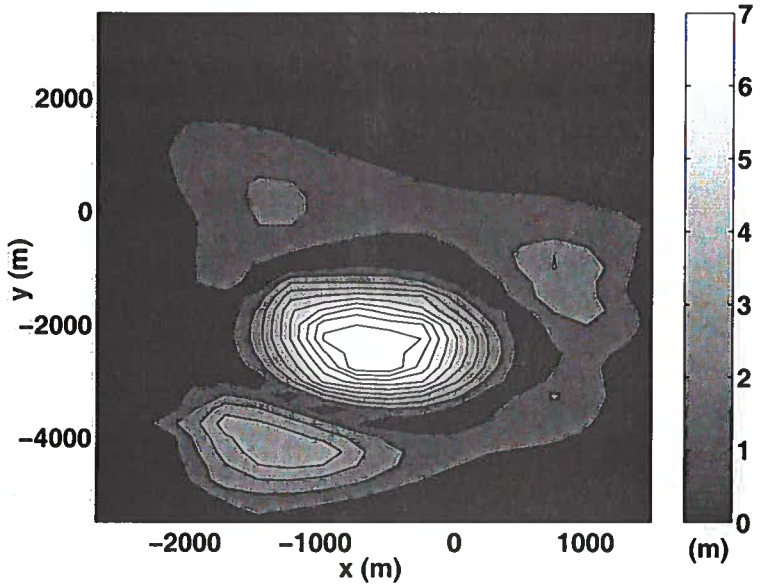

Figure 2.13. Contour map showing the difference between the recovered base salt using the complete-β and dynamic-β methods with fixed HCZ. The maximum difference is 7.2 m.

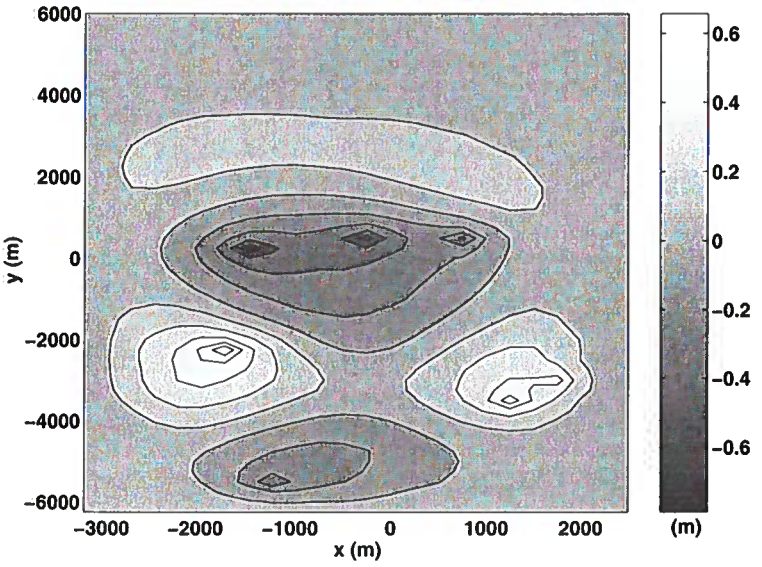

Figure 2.14. Contour map showing the difference between the recovered base salt reconstructed using the complete-β and dynamic-β respectively without fixing an HCZ. The maximum difference is 0.8 m.

Chapter 3

Error analysis: data error

In this chapter, I examine the sensitivity of the model to data errors, which include uncorrelated random noise and correlated noise related to geology. In particular, I concentrate on additive Gaussian random noise and correlated noise simulating inaccurate bathymetry correction. For random noise, I derive two Bayesian-style linearized formulas for standard deviation and bias of model and apply them to the salt inversion. Second, I quantify both the sample standard deviation and bias of the model by carrying out a sequence of inversions for each noise level. For correlated noise, I introduce spatially correlated perturbations to the bathymetry to simulate geological noise and quantify the inversion error as a function of perturbation. I use the same synthetic salt model that used in Chapter 2.

3.1 Uncorrelated random noise

Uncorrelated random data noise can come from several different sources, including (Clarke, 1969) random measurement errors, shallow distributed masses, and errors in corrections for terrain and elevation. Such noises can propagate into the inverted results and increase the uncertainty of inverted models. In practical applications, field gravity data are contaminated by many contributing error factors. It is therefore reasonable to assume that the noise is Gaussian, independently and identically distributed based on the central limiting theory. Moreover, the assumption of Gaussian random noise is widely used as the major type of data error in gravity inversion studies (e.g., Reamer and Ferguson, 1989; Li and Oldenburg, 1998). Therefore I adopt the same assumption in the following. I evaluate the standard deviation and bias of the recovered base salt as a function of the amplitude of additive Gaussian random noise in the gravity data.

I approach this topic in two different ways. First, I derive linearized formulas for standard deviation and bias of inverted models. Second, for each noise level I carry out 100 inversions each with 100 different realizations of the additive noise. The six levels of noise have standard deviation of 0.05, 0.1, 0.2, 0.3, 0.4 and 0.5 mGal, as compared with a maximum gravity anomaly of about 10 mGal. Based on the test results, I estimate the behavior of errors in the model and the accuracy of the linearized approximation.

3.1.1 Linearized analysis

In this section, I derive an analytical solution for the standard deviation and bias of an inverted model based on the Bayesian approach and linearization around the final inverted

model. By definition in equation (2.3), a model is governed not only by the input data, but also by the incorporated reference model. According to Scales and Snieder (1997) this kind of problem is Bayesian since the reference model serves as the prior information of the model. Alambaugh and Newman (1999) present a posterior covariance matrix for the model and model resolution matrix (MRM) for a regularized inverse problem incorporating no reference model. Similarly, I derive the covariance matrix and the resolution matrix by linearized approximation for the base-salt inversion, but incorporating a reference model. Then, I compute estimates of the standard deviation and bias of models.

Following Tarantola (1987), if we assume that the observation is independent of priori information of model parameters and that the distributions of data and prior information of model parameters both are Gaussian, the posterior probability density of the model can be expressed as

$$\sigma_M(\vec{m}) = C \cdot e^{-\frac{1}{2}\left[(F(\vec{m})-\vec{d})^T C_d^{-1}(F(\vec{m})-\vec{d})+(\vec{m}-\vec{m}_0)^T C_m^{-1}(\vec{m}-\vec{m}_0)\right]}, \tag{3.1}$$

where C is a constant, $\vec{d}$ denotes the observations, $F(\vec{m})$ denotes the predicted data, C_d and C_m are the data covariance and *a priori* model covariance matrices, and $\vec{m}_0$ represents a reference model. To find the maximum *a posterior* probability (MAP) model, one performs a Bayesian inversion to maximize the *a posterior* probability density of model parameters, $\sigma_M(\vec{m})$. This is equivalent to minimizing

$$\Phi(\vec{m}) = \left[\left(F(\vec{m}) - \vec{d}\right)^T C_d^{-1}\left(F(\vec{m}) - \vec{d}\right) + (\vec{m} - \vec{m}_0)^T C_m^{-1}(\vec{m} - \vec{m}_0)\right]. \tag{3.2}$$

The Bayesian inversion in equation (3.2) is the same as the regularized inversion problem defined in Chapter 2 if $W_d = C_d^{-1}$ and $\beta W^T W = C_m^{-1}$. Bayesian error analysis thus is applicable to uncertainty study for the regularized inverse problem under the assumptions above.

According to Tarantola (1987), if the forward operator is not too nonlinear, i.e., $F(\vec{m})$ is linearizable in the vicinity of the MAP model, i.e., $\vec{m}_{MAP}$, then the *a posterior* probability density in the model space is approximately Gaussian:

$$\sigma_M(\vec{m}) \propto C \cdot e^{(\vec{m}-\vec{m}_{MAP})^T C_M^{-1}(\vec{m}-\vec{m}_{MAP})}, \tag{3.3}$$

and

$$C_M \cong \left(G_{MAP}^T C_D^{-1} G_{MAP} + C_m^{-1}\right)^{-1}, \tag{3.4}$$

where $\vec{m}_{MAP}$ is a maximum *a posterior* probability model, and G_{MAP} is the sensitivity matrix evaluated at $\vec{m}_{MAP}$, $C_d^{-1} = W_d^T W_d$ and $C_m^{-1} = \beta W^T W$.

Appendix A gives the derivation of the covariance matrix. Since the absolute value of variance is given by the scaled diagonal elements in the covariance matrix, we have the variance as

$$\sigma_m^2(i) = \lambda C_M(i,i), \qquad i = 1, 2, ..., M, \tag{3.5}$$

where λ is a scalar, dependent on the data error, reference model, and regularization parameter, and M is the length of the model vector. Further, the depth of the base salt $h(i)$ is given by [equation (2.25)]

$$h(i) \quad = \tilde{h}_0 e^{m(i)} + h_t(i), \qquad i = 1, 2, ..., M. \tag{3.6}$$

Therefore, the first-order approximation of the standard deviation of the solution for the base salt is given by

$$\sigma_h(i) \quad \cong \tilde{h}_0 e^{m(i)} \sigma_m(i), \qquad i = 1, 2, ..., M. \tag{3.7}$$

Because $m(i) = \log(\frac{h(i)-h_t(i)}{\tilde{h}_0})$, equation (3.7) becomes

$$\sigma_h(i) \quad \cong (h(i) - h_t(i))\sigma_m(i), \qquad i = 1, 2, ..., M. \tag{3.8}$$

In Appendix B, I obtain the linearized approximation for the bias of the recovered model. When we reach the MAP model, the model bias can be expressed approximately as

$$\vec{m} - \vec{m}_{true} = \left[\left(G_{MAP}^T C_d^{-1} G_{MAP} + C_m^{-1} \right)^{-1} G_{MAP}^T C_d^{-1} G_{MAP} - I \right] (\vec{m}_{true} - \vec{m}_0), \tag{3.9}$$

where G_{MAP} is the sensitivity matrix evaluated at $\vec{m}_{MAP}$. from equation (2.24), we derive $m_{MAP}(x,y) - m_{true}(x,y) = \log \frac{h_{MAP}(x,y)-h_t(x,y)}{h_{true}(x,y)-h_t(x,y)}$. Therefore, the estimated bias of the depth of the base salt can then be computed

$$h(x,y) - h_{true}(x,y) = (h_{true}(x,y) - h_t(x,y))e^{m_{MAP}(x,y)-m_{true}(x,y)} - (h_{true}(x,y) - h_t(x,y)). \tag{3.10}$$

To illustrate the results in equation (3.7) and (3.10), I carry out a sequence of inversions for the model defined in the numerical example in the preceding chapter. The input data are the synthetic anomaly produced by the salt model contaminated with six different levels of random noise. The standard deviations are respectively 0.05, 0.1, 0.2, 0.3, 0.4 and 0.5 mGal. Again, I assume independent identically-distributed Gaussian random noise and use the anomaly observed on the surface at the same 400 points shown in Figure 2.9. The noisy data are defined as follows

$$\vec{d}_{obs} \quad = \vec{d}_{true} + \sigma_d N(0,1), \tag{3.11}$$

where $N(0,1)$ denotes Gaussian random noise with unit standard deviation, σ_d denotes the standard deviation, and $\vec{d}_{true}$ represents the true anomaly by salt. Through inversion, I obtain a set of recovered depths of base salt (Figure 3.1) corresponding to different noise levels and assume that they are the maximum *a posterior* probability models.

Using equation (3.7) and (3.10), I compute the linearized estimates of standard deviation and bias of model while setting $\lambda = 1$ arbitrarily. The contoured results are shown in Figure 3.2 and Figure 3.3, respectively.

The predicted standard deviation in Figure 3.2 is quite correlated with the thickness

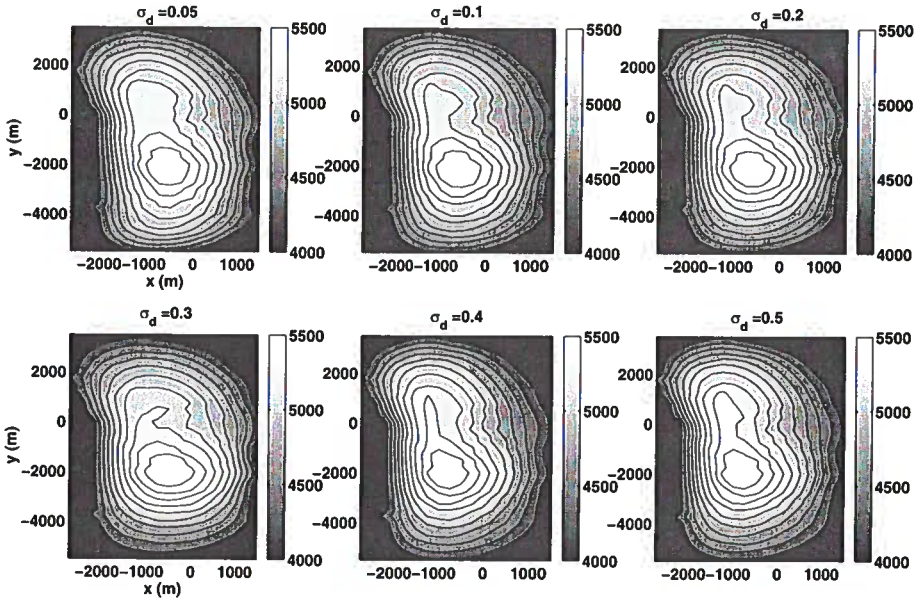

Figure 3.1. Recovered depths (m) of base salt for different levels of random noise. The numbers shown on the top of each panel represent the standard deviation of the noise (m).

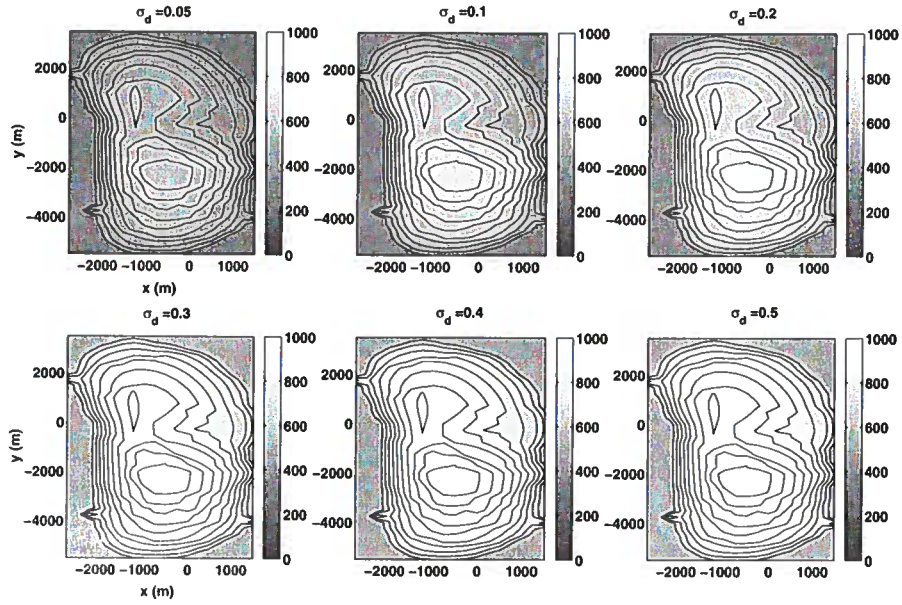

Figure 3.2. Linearized approximation of the standard deviation (m) for recovered base of salt for different levels of random noise. The numbers shown on the top of each panel represent the standard deviation of the noise (m).

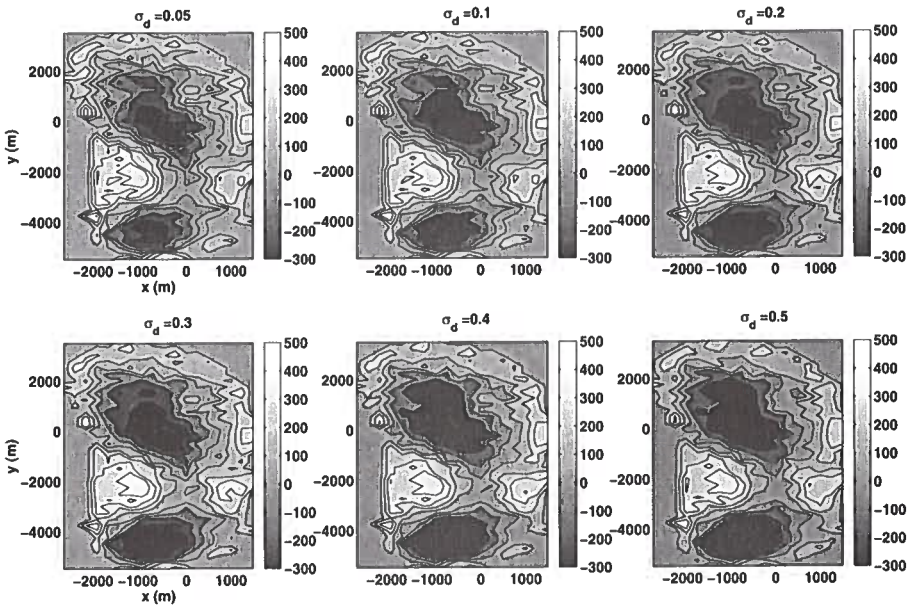

Figure 3.3. Linearized approximation of the bias (m) for recovered base of salt for different levels of random noise. The numbers shown on the top of each panel represents the standard deviation of the noise (m).

of the salt: the thicker the salt, the larger the standard deviation. Given the noise level, the standard deviation of the base salt defined in equation (3.8) depends on both the thickness of the salt and the covariance matrix, which is evaluated at the MAP solution of the logarithm of the salt thickness (model parameter) [equation (3.4)]. Therefore, the salt thickness primarily determines the distribution of the standard deviation of the recovered base salt. Further, in order to ascertain the relationship between the standard deviation of the solution and noise levels, Figure 3.4 shows the computed RMS values for the standard deviation of the model for each noise level. Not surprising, the error increases with the noise level.

The contoured maps of the estimated bias exhibit a uniform pattern for different noise levels in Figure 3.3. The positive values along the edge of the model indicate that the base salt in the recovered model deeper than the true one in those regions. In contrast, negative values of bias concentrate in two areas in the center of the model. Clearly, then, the recovered base salt should be flatter than the true model. The RMS values for the bias in Figure 3.5 increase with the noise level. The increment, however, decreases with the increase of noise, and the difference between the maximum and minimum bias is only about 45 m. It appears that the bias of the model does not vary significantly when the random noise level changes. 155-m RMS bias, however, is large when the data standard deviation is 0.05 mGal. This is because the recovered depth of base salt is not only governed by the input gravity data but also the incorporated reference model. Specified in equation

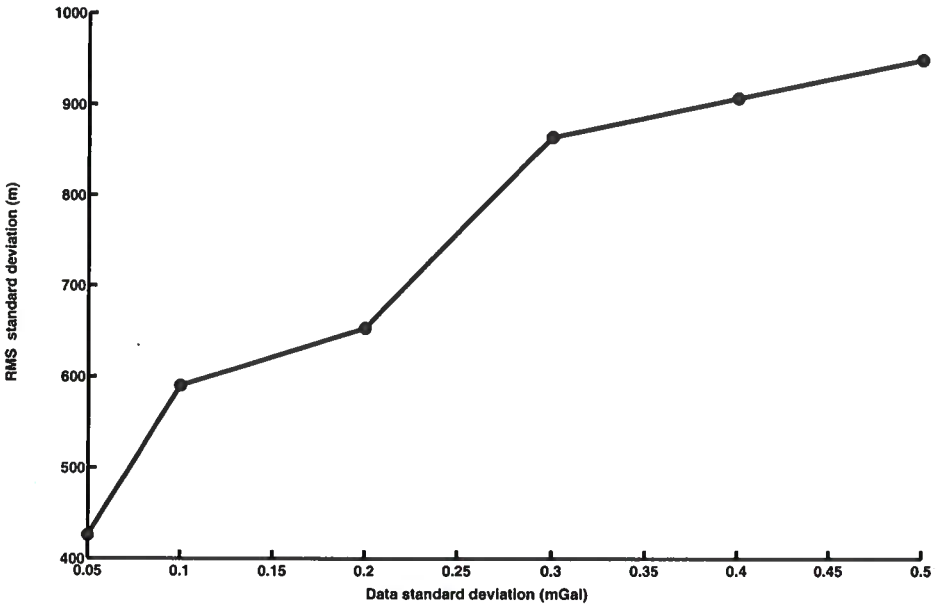

Figure 3.4. RMS error estimated from the linearized approximation of standard deviation for the recovered base of salt versus the standard deviation of the added random noise in the data.

(2.2), the expected model has minimum difference from the reference model, which has large difference from the true model here. Therefore, the recovered base salt largely biased from the true position although the noise level is not too high.

The standard deviation and bias may not reflect the true values since the linearized analysis is based on a number of assumptions. These estimates, however, provide a qualitative measure of the reliability and indicate the relative reliability in different parts of the model.

3.1.2 Direct evaluation

The above analysis illustrates the behavior of uncertainty of base salt by linearized approximation. A more accurate method is to evaluate the standard deviation and bias directly by carrying out a sequence of inversions using datasets contaminated by different realizations of noise with the same standard deviation. When the number of realizations is sufficiently large, one can expect an accurate estimate of the standard deviation and bias. Corresponding to the linearized-approximation study above, I use data with six different levels of noise. The standard deviations are 0.05, 0.1, 0.2, 0.3, 0.4 and 0.5 mGal. I generate 100 realizations of the noise for each level of standard deviation and invert data contaminated by each realization.

Once all 100 inversions are done, for each noise level I compute the sample standard deviation and bias of the model relative to the true model.

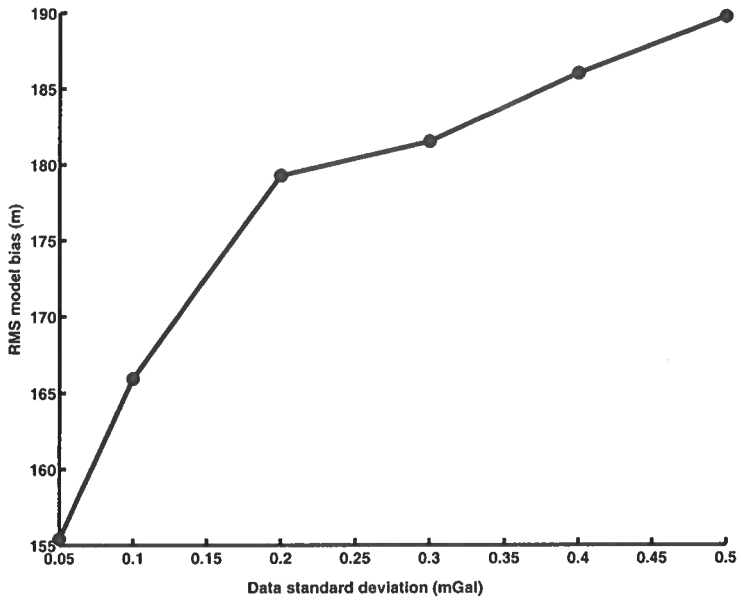

Figure 3.5. RMS error estimated from the linearized approximation of bias for the recovered base of salt with respect to the random noise versus the standard deviation of the added random noise in the data.

1. Sample standard deviation:

$$\sigma'_{hj} = \sqrt{\frac{1}{N-1}\sum_{i=1}^{N}(h_{ij} - h_{avej})^2}, \quad j = 1, ..., M \tag{3.12}$$

where h_{ij} denotes the depth for the jth cell in the recovered base salt for ith realization, $\vec{h}_{avej}$ represents the average depth of the base salt at jth cell, and $N = 100$ is the number of realizations.

2. Bias

$$\theta' = \vec{h}_{ave} - \vec{h}_{true}, \tag{3.13}$$

where $\vec{h}_{true}$ denotes the true depth of the base salt.

The computed sample standard deviations as a function of the data error are shown in Figure 3.6. These contour maps show that the standard deviation increases with increasing noise level, as expected. They, however, show a pattern that differs in detail from that in the linearized approximation shown in Figure 3.1.

Figure 3.7 summarizes the estimated standard deviation by both the linearized approximation and the direct evaluation, showing RMS values for the standard deviation for different noise levels. The RMS value for the sample standard deviation corresponding to the maps in Figure 3.5 not surprisingly increases with the noise level. Moreover, the result

by linearized approximation is generally consistent with the computed values in terms of the trend (Figure 3.7). The values differ approximately by a constant scaling factor $\frac{1}{8}$, which is not surprising since the covariance matrix provides only a relative estimate of the standard deviation [recall that we used an arbitrary choice for λ (i.e., λ =1) in equation (3.5)]. Therefore, linearized approximation can be helpful for estimating the trend of the errors of models with different levels of random noise in data.

The bias in the depth of the recovered base salt is summarized in Figure 3.8. The contour maps indicate that the evaluated bias is close to that of the linearized approximation shown in Figure 3.3. Figure 3.9 further illustrates this conclusion. This indicates that the linearized approximation can be used (with a scale factor) to quantify the bias in the inversion.

Note again that the standard deviation and the bias do not change significantly when the noise level changes. Because we have added uncorrelated Gaussian noise and no geologically reasonable base-salt structure at a depth of several kilometer can produce highly variable noise on the surface, random noise is not a serious factor in inversion. This can be further illustrated by the Tikhonov curves for different levels of noise in Figure 3.10. For large β values the curves flatten out because the recovered models fit more noise with increasing the level of data noise. The locations of the quite distinctive knees of all curves, however, are almost same; changing the level of the random noise does not change the model solutions significantly, i.e., the models solutions are not sensitive to the change of the level of noise. Therefore, the standard deviation and the bias may not vary rapidly with the increasing of the level of noise. Purely uncorrelated noise, of course, is not common in the practice. I will address the issue of correlated noise in a later section.

In summary, in the presence of random noise both the bias and standard deviation of recovered models increase with increasing data noise level, since the model attempts to fit the increased noise. Increasing the level of random noise, however, does not significantly increases the uncertainty of the recovered depth of the base salt.

3.2 Geological noise

In addition to uncorrelated random noise, correlated noise often is present in gravity data. Sources of the correlated noise include error in density contrast, in bathymetry correction, and in residual regional correction. Unlike uncorrelated random noise, correlated noise can lead to large-scale spurious structures in gravity inversion. It is, however, difficult to investigate this kind of error in general without problem-dependent information. Instead, I focus on one type of correlated noise that can often happen in practical applications: the data error caused by inaccurate bathymetry correction.

I simulate the error in bathymetry correction by using correlated random noise to perturb the bathymetry, and then add the computed gravity anomaly produced by the perturbation of bathymetry to the gravity data of the salt body.

For simplicity, I assume that the correct bathymetry plane is located at the depth of 1200 m, with constant density contrast, and the erroneous bathymetry departs from this plane by correlated Gaussian random noise having four different standard deviations: 5, 10,

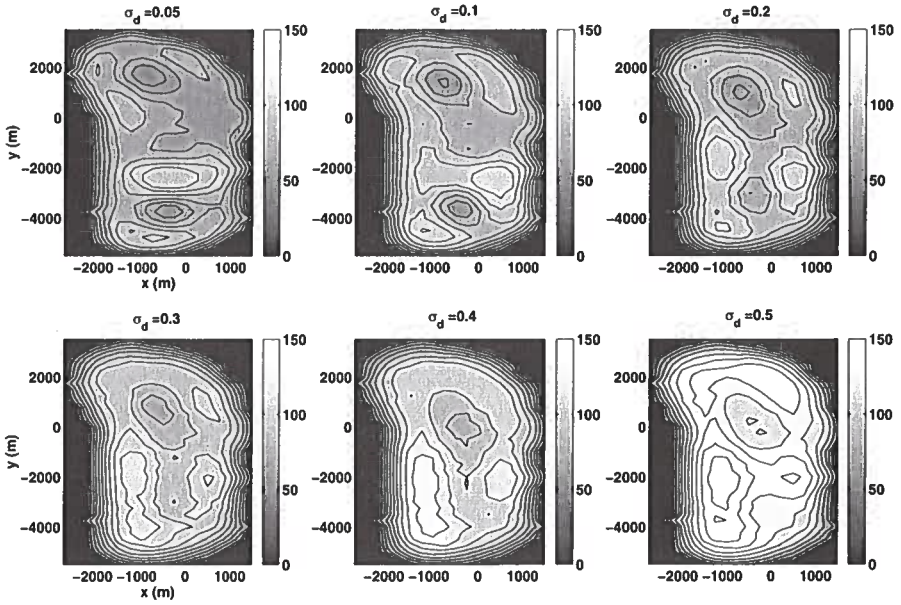

Figure 3.6. Computed standard deviation (m) of recovered salt models for different levels of random noise. The numbers shown on the top of each panel represent the standard deviation of the noise (m).

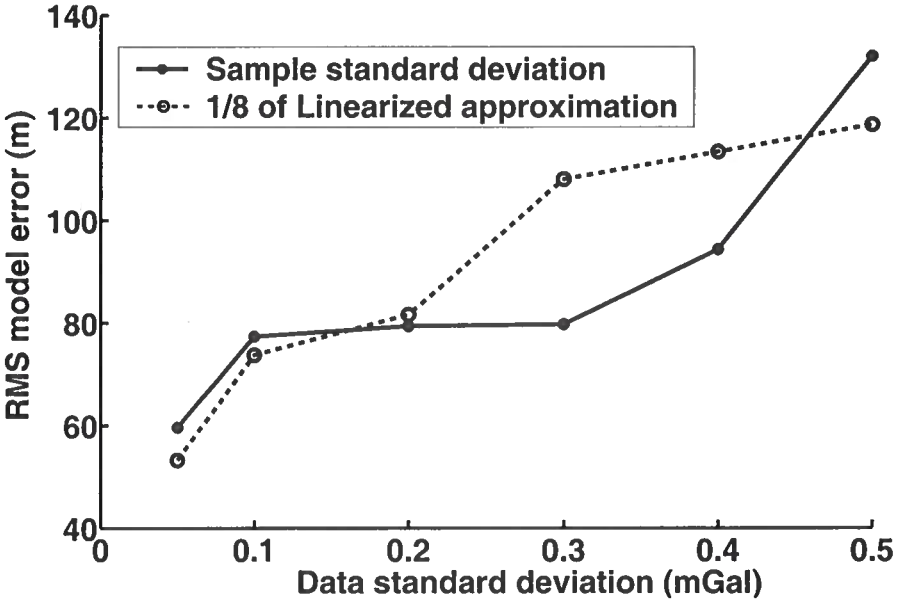

Figure 3.7. RMS value of the measured standard deviation of depth of recovered base salt versus standard deviation of added random data noise.

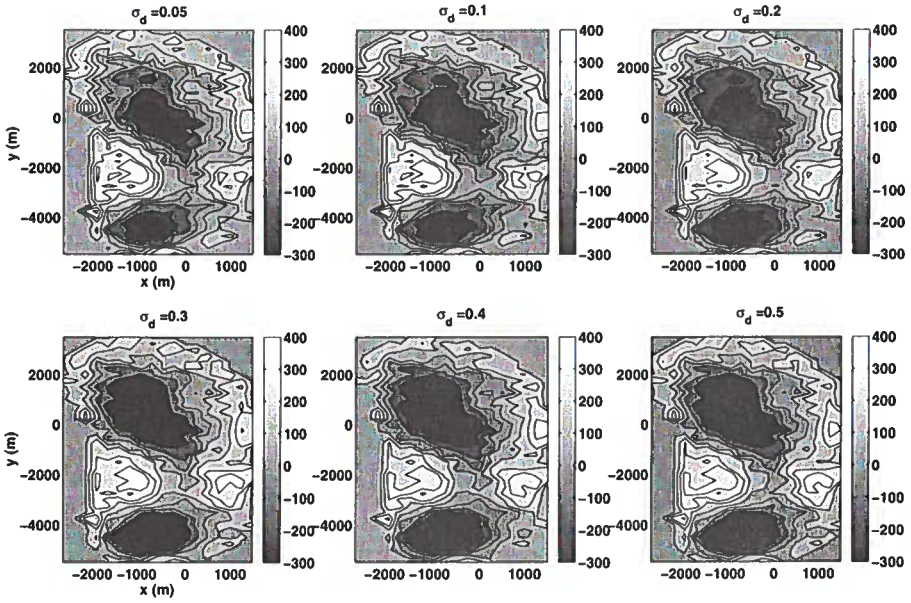

Figure 3.8. Measured bias of depths of base salt (m) for different levels of added random data noise. The numbers shown on the top of each panel represent the standard deviation of the noise (m).

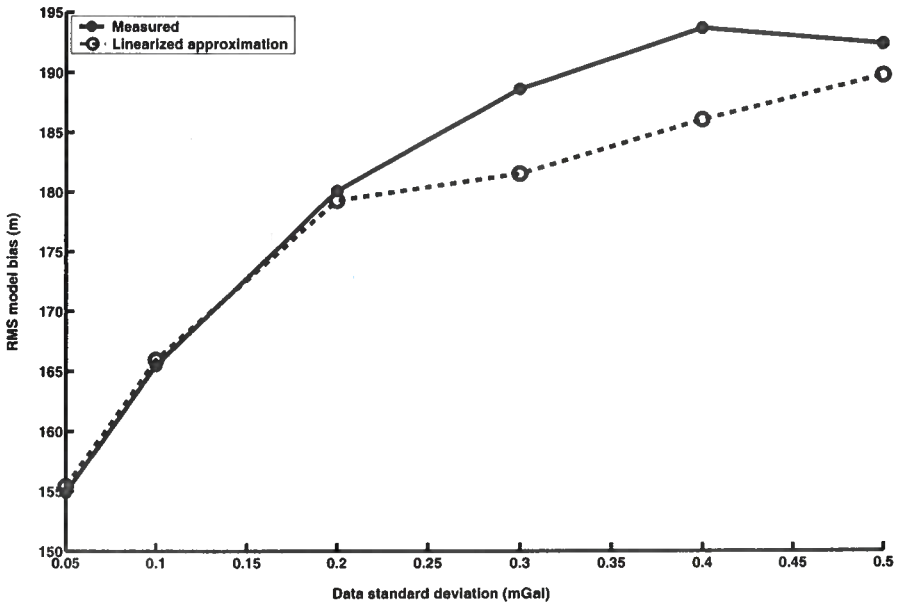

Figure 3.9. RMS value of measured bias in recovered depth of base salt (m) versus the standard deviation of additive random noise in the data.

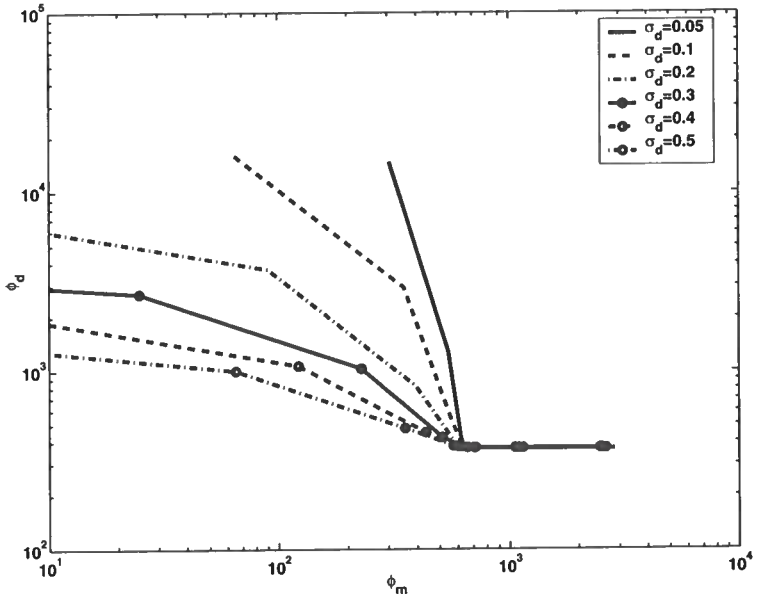

Figure 3.10. Log-log plot of the data misfit, ϕ_d, as a function of the model objective function, ϕ_m, for different levels of nose.

15 and 20 m, with a correlation radius of 400 m.

The perturbation is simulated by a geostatistical approach, the FFT method described by Easley et al. (1990). The autocovariance function of this perturbation model is given by,

$$a(x,y) = \lambda^2 e^{-\frac{1}{2}(\frac{x^2}{L_x^2}+\frac{y^2}{L_y^2})}, \tag{3.14}$$

where λ is the standard deviation of the perturbation data, and L_x and L_y denote the correlation lengths in x- and y-directions. Fourier transform of $a(x,y)$ gives the power spectrum

$$P(\omega_x,\omega_y) = \mathcal{F}_{xy}(a(x,y)),$$

where $\mathcal{F}_{xy}$ denotes the 2D Fourier transform. In the Fourier domain the spectrum of the perturbation is given by

$$\tilde{b}(\omega_x,\omega_y) = \sqrt{P(\omega_x,\omega_y)}e^{i\theta}, \tag{3.15}$$

where θ is the phase. Each random number is produced by one realization of random phase θ, which is uniformly distributed between 0 and 2π. To obtain the numerical results of the bathymetry perturbation, I create a model by unit standard deviation, and then scale this model with four different levels of standard deviations, 5, 10, 15 and 20 m. Therefore, all perturbations have the same statistical properties except for amplitude.

Figure 3.12 shows the bathymetry perturbation introduced into the model for a stan-

dard deviation of 5 m. I add the gravity anomaly (see Figure 3.13) produced by bathymetry perturbations having different levels of standard deviation to the noise-free gravity data and invert the contaminated data to obtain an estimate of the base salt. To assess the error for various perturbed models, I evaluate the difference between the best model and the recovered models.

The best model here refers to the model reconstructed by inverting the noise-free data. Ideally, it is the model that best fits the data. Equation (2.3) becomes

$$\phi = \phi_d = ||(\vec{d} - \vec{d}_{obs})||_2^2. \tag{3.16}$$

Since an inversion algorithm can be carried out only discretely, numerical error inevitably occurs. Models that exactly fit data that contain numerical error cannot be the best model. Therefore, it is reasonable to use a regularized model. Here, I assume that the best model is the one recovered from the noise-free data incorporating a reference model as in equation (2.26). I carry out the inversion with an L-curve criterion, with W_d being an identity matrix. The inverted model is shown in Figure 3.14.

I conduct one realization of gravity inversion for each of the four different levels of noise. Figure 3.15 shows the contour maps of the difference between the depth of base salt for the best estimated model and the recovered models. As expected, the error of the base salt increases monotonically with the bathymetry perturbation. This kind of error is problem-dependent, e.g., the large positive anomaly on the upper side of the contour map in Figure 3.13 leads to a large pull-up in the base salt shown toward the top left-side of the contour map in Figure 3.15. The error has the same pattern for different amplitudes of bathymetry perturbation because the statistical pattern for all the bathymetry perturbations is same in this study. The curve of RMS difference (see Figure 3.16) also demonstrates that the error of the recovered base salt increases monotonically with the perturbation. With 10-m perturbation, for example, the RMS difference exceeds 200 m. In this sense, the correlated geological noise can demonstrably cause large error in base salt.

3.3 Summary

I have investigated the influence of uncorrelated random data error and correlated data error on gravity inversion. Change in the levels of the uncorrelated random data noise has only small influence on the standard deviation and bias of the recovered base salt. In contrast, the recovered base salt is more sensitive to the amplitude of the bathymetry perturbation. Therefore, one should pay more attention to the correlated data noise introduced by geological features. Moreover, the linearized approximation of the uncertainty shows that the linearized covariance matrix can provide a qualitative understanding of the error in the model. The biases computed by both linearized approximation and numerical testing are consistent with one another.

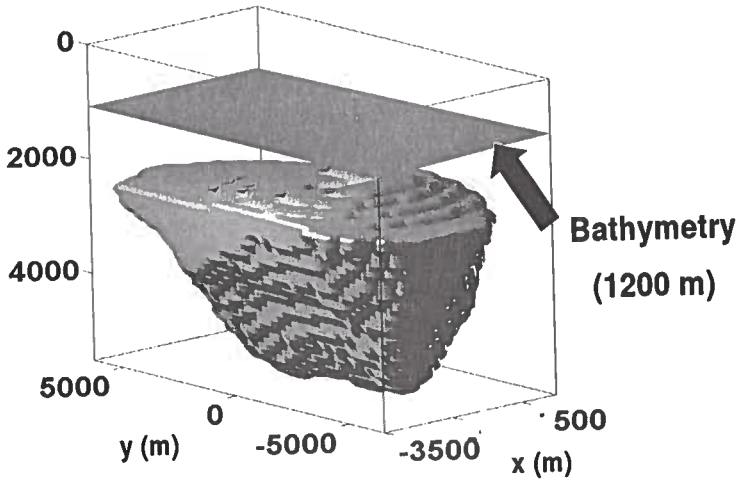

Figure 3.11. 3D view of salt model in the presence of horizontal bathymetry. The bathymetry is assumed be constant at depth of 1200 m.

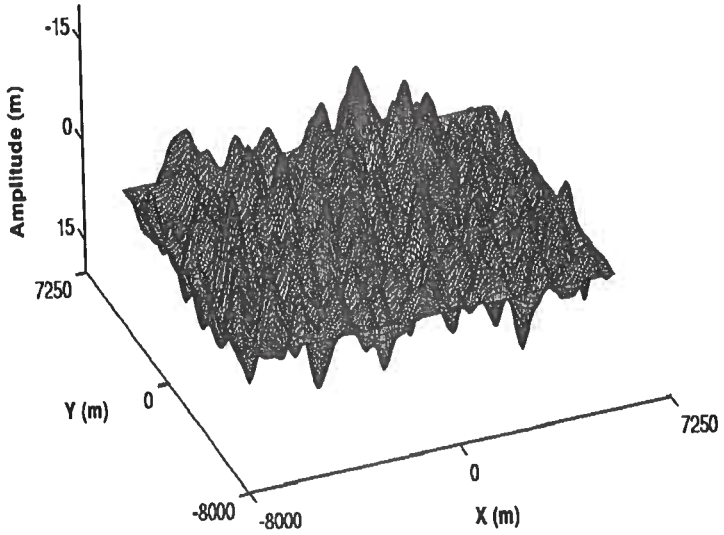

Figure 3.12. Bathymetry perturbation: correlated Gaussian random noise having the standard deviation of 5 m.

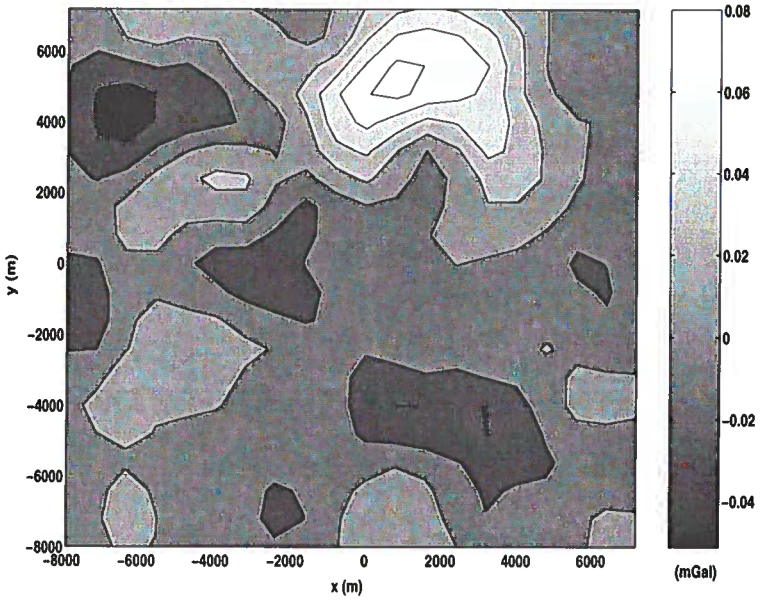

Figure 3.13. Data noise introduced by a variable bathymetry simulated using a correlated random perturbation with standard deviation of 5 m.

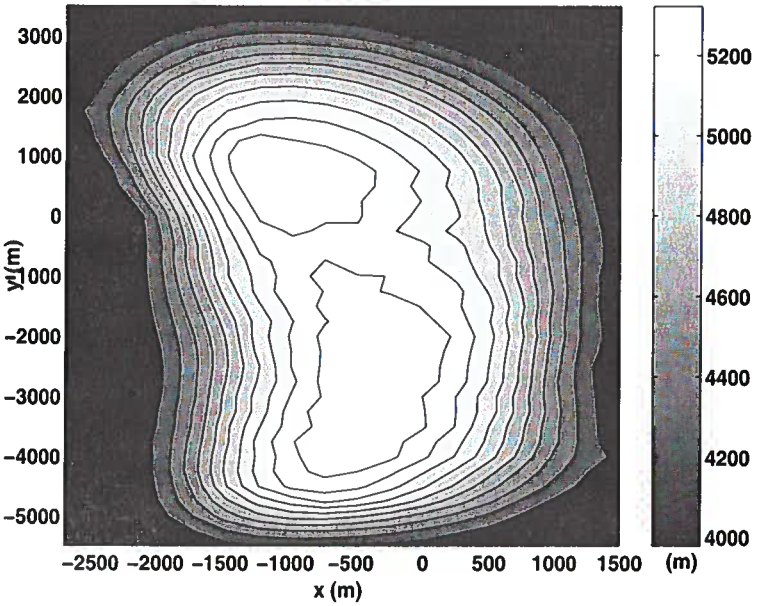

Figure 3.14. Best estimated model of the base salt inverted from noise-free data.

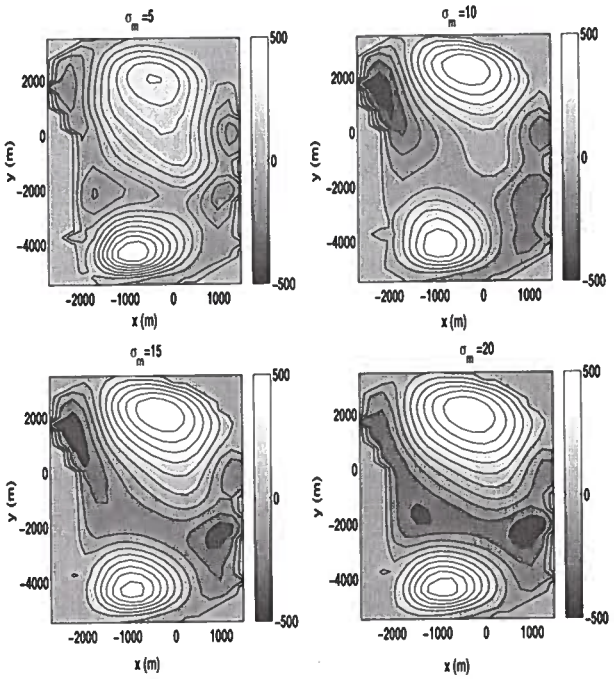

Figure 3.15. Contour maps of the difference between the depth of the best-estimated base salt and the recovered base salt for different levels of bathymetry perturbation.

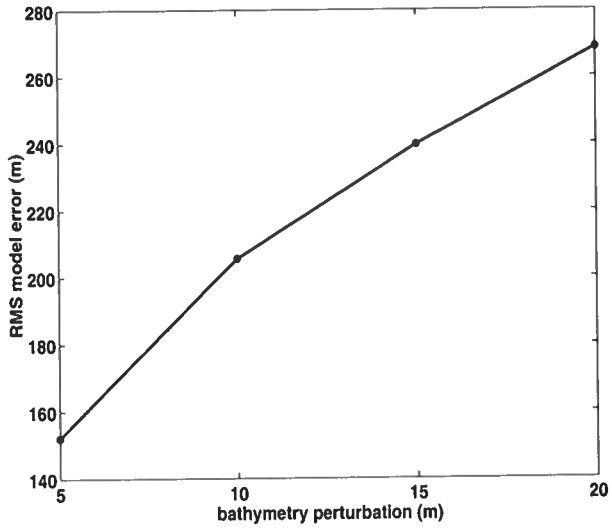

Figure 3.16. RMS difference between best and the recovered base salt as a function of geological noise.

Chapter 4

Error analysis: prior information

The inversion algorithm assumes that top salt, density contrast, and a portion of the base salt, the high confidence zone (HCZ), are known. In practical applications, these model parameters are obtained through different geophysical methods and thus inevitably contain errors. Inaccurate assumptions for these presumed-known quantities degrade the quality of the inverted base salt. It is of practical importance to assess the sensitivity of the model to errors in prior information about the model. I examine the influence by inverting the gravity anomalies and quantifying the errors in the inverted models produced by each of these three types of errors.

To understand the influence of errors in the model globally, I used the root-mean-square error of the recovered base of salt relative the best-estimated model as a numerical measure. The RMS error is defined as

$$e_{rms} = \sqrt{\frac{1}{M}\sum_{i=1}^{M}(h_{best}(i) - h_{rec}(i))^2}, \tag{4.1}$$

where, h_{best} denotes the best-estimated model depth and $h_{rec}(i)$ the recovered model depth. The best-estimated model refers to the model recovered from the same data without any error in the above assumptions. The input data, however, are still contaminated by Gaussian noise.

The synthetic gravity data are the same as those used in Chapter 2, and the contaminating Gaussian random noise has a standard deviation of 0.1 mGal.

4.1 High confidence zone (HCZ)

In practice, one often fixes a portion of the base of salt (e.g., Figure 2.10) that is believed to be accurately known; this portion of the salt might, for instance, be obtained from seismic imaging. This part of the base of salt is the so-called high confidence zone (HCZ). In gravity inversion, this part of the model is fixed and excluded from the unknown model to be recovered. Correct specification of the HCZ can reduce the uncertainty of the model since it provides an additional constraint, as illustrated in Figure 4.1. The HCZ is the same as that defined in Figure 2.10 in Chapter 2. Figure 4.1a shows the difference between the base-salt depth in the true model and that the recovered model with an HCZ constraint; Figure 4.1b shows the difference between the true model and the recovered model without the HCZ constraint. Clearly, the HCZ has helped reduce the model error.

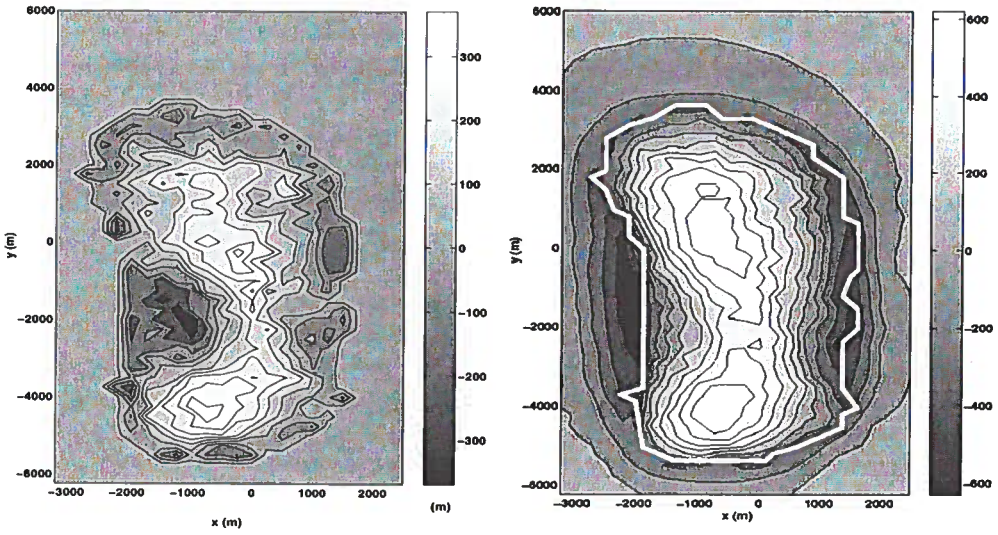

(a) (b)

Figure 4.1. Comparison between the base-salt depth in the true model and in the recovered model (a) with HCZ, and (b) without fixing an HCZ. The maximum error in (a) is about 400 m, whereas it is larger than 600 m in (b). Within the white curve in (b) is the unknown model area in (a).

If the HCZ is incorrectly specified, however, results can be greatly degraded. Error in the HCZ is transmitted to the recovered base salt in the unknown area and can produce large errors. For instance, Figure 4.2 shows the recovered model when the HCZ is shifted to shallower depth by 2.5%. The maximum difference in depth between this and the best model is as large as 600 m. It is therefore important to understand the magnitude of error that can be caused by such input errors.

I assess the sensitivity of the recovered model to HCZ errors by perturbing the HCZ by $\pm 2.5\%$, $\pm 5\%$ and $\pm 10\%$ from the true depth. Figure 4.3 shows a cross-section through the center of the 3D salt model in the x-direction (the location of the cross-section is shown as the dashed line in Figure 5.1). I pretend that the perturbed HCZ is correct and carry out the inversion based on different incorrect HCZs. For each level of perturbation, one realization of inversion is applied. Figure 4.4 shows plan-view contour maps of the recovered base salt for different perturbations to the HCZ. I again define the best-estimated model as the model recovered from the data without errors in HCZ, and use it as the reference to compute the error in the recovered model. Figure 4.5 shows the difference between the best-estimated model and the recovered models for the six levels of perturbations.

As one might expect, the recovered models move in the opposite direction as the HCZ is perturbed up or down.The influence of error in HCZ is dramatic: perturbing upward by

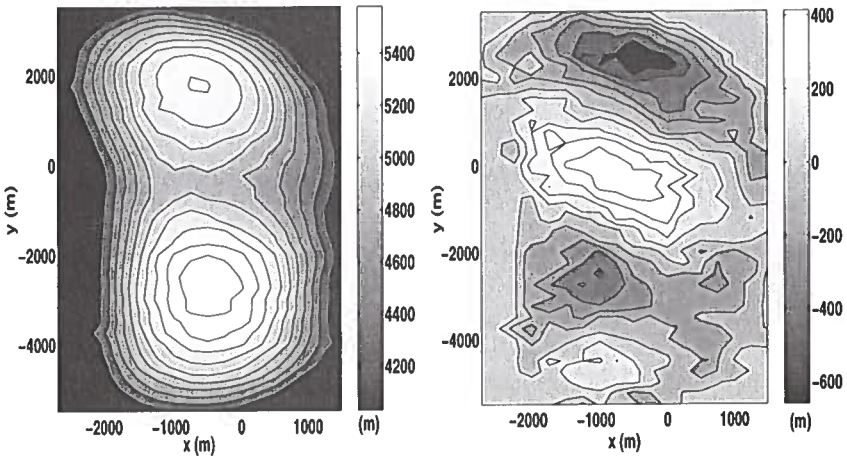

Figure 4.2. Influence of incorrect HCZ on the inversion for the depth of base salt. (a) The recovered model for the HCZ is shifted up by 2.5%. (b) The difference between the recovered base-salt depth when the HCZ is shifted up by 2.5% and the recovered base salt wihout error in HCZ. The maximum error can be larger than 600 m.

5% produces a maximum difference of more than 1000 m from the best-estimated model. Although this error is problem-dependent, this large number does give an indication of the magnitude that can be expected in general.

To summarize the error dependence on HCZ errors, Figure 4.6 shows the RMS difference between the best-estimated model and the models recovered with incorrect HCZ. The curve is asymmetric, indicating that shifting HCZ upward leads to larger error compared to shifting downward by the same perturbation. This is because gravity data are more sensitive to shallow geology, since gravity anomalies decay with distance squared.

Erroneous HCZ does not necessarily lead to larger error in the inverted model than does inversion without fixing an HCZ. Figure 4.7 shows the contoured difference between the true base salt and the recovered base salt with HCZ that is 5% deeper than the true value. The maximum error in Figure 4.7 is about 600 m, close to the maximum error without fixing an HCZ (Figure 4.1b). However, the RMS value of the error caused by the erroneous HCZ is 262 m whereas it is 312 m for the case without HCZ specified. The RMS value of the error, however, exceeds 360 m when the HCZ is 5% shallower than the true value. This indicates that when the error in the HCZ is within certain range, e.g., less than 3% or 4%, its use still can improve the base salt salt. Both underestimating and overestimating the HCZ depth by more than that amount can lead to large errors in inverted depth of base salt, the effect being more severe for the former.

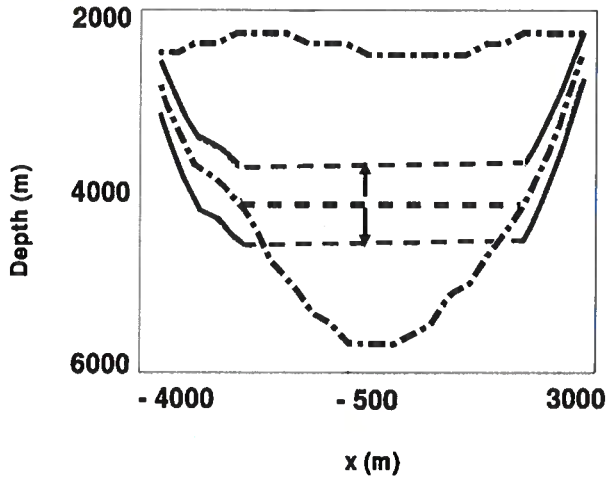

Figure 4.3. 2D cross-section through the 3D salt model showing the definition of HCZ perturbations. The dash-dotted lines represent the true top salt and base salt and the solid lines represent the perturbed HCZ. As the HCZ is shifted from its true location, the initial model changes accordingly. The three dashed lines represent the true initial model (bold line), and upper and lower limits of the perturbed initial models.

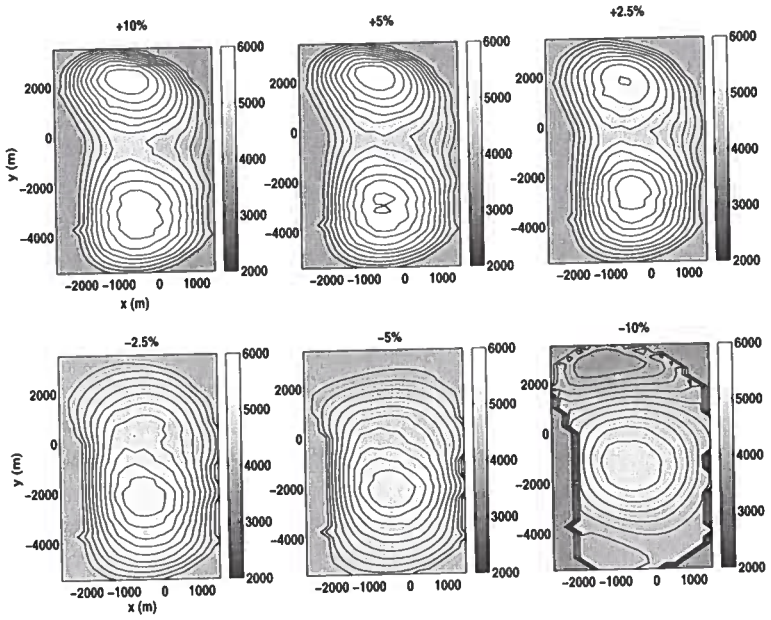

Figure 4.4. Base-salt depth (m) recovered using different incorrect HCZs. The numbers shown on the top of each panel represent the perturbation of the HCZ in percent.

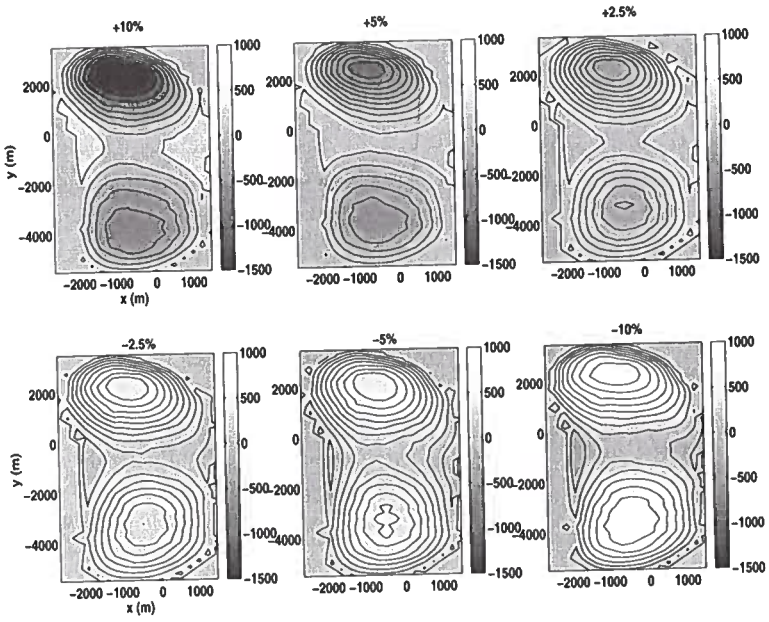

Figure 4.5. Base-salt depth difference (m) between the best model and models recovered using incorrect HCZ. The numbers shown on the top of each panel represent the perturbation of the HCZ in percent.

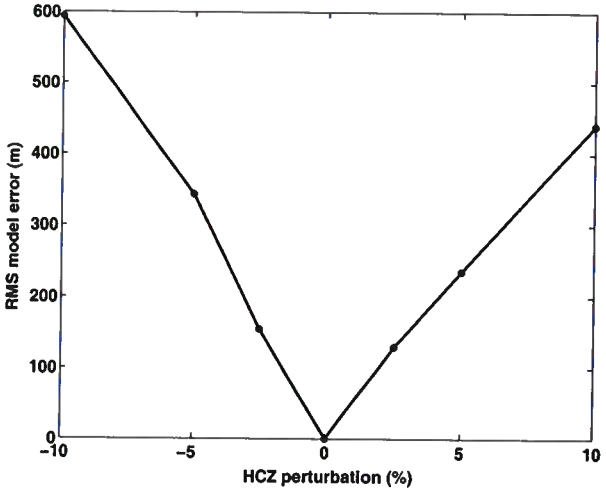

Figure 4.6. RMS depth differences between the best recovered model for base salt and those using incorrect HCZ. Here, "+" means pushed downward.

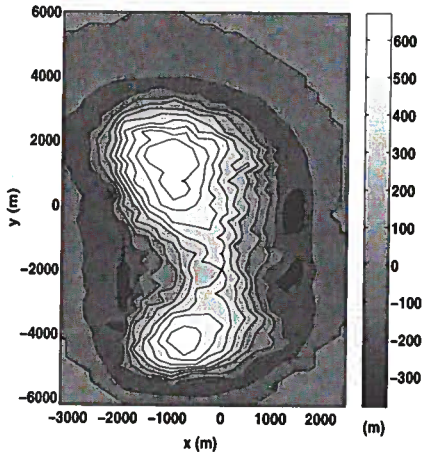

Figure 4.7. Base-salt depth difference between the true base salt and the base salt recovered while the HCZ is shifted down by 5%. The RMS error is 262 m.

4.2 Error in top of salt

In seismic prestack depth migration, the seismic reflection data are migrated to construct an image of subsurface geological features based on models for migration velocity. The error in overburden velocity in the migration-velocity model can cause depth errors and quality degradation in the image of the top of salt. One dominant result can be a DC shift in depth of the entire salt image. In the 3D synthetic salt example, this implies that the top salt is erroneously defined, so that both the top salt and HCZ used are incorrect.

I simulate this kind of error by perturbing the top salt by a constant, moving the known top salt, together with the HCZ, up or down in depth while preserving its shape. Specifically, I perturb the depth of salt by ± 50, ± 100, and ± 200 m. Figure 4.8 shows the same 2D vertical-section as in Figure 4.3 through the 3D salt model illustrating the definition of such perturbation. The "+" means shifted downward. I pretend that these perturbed top salt and HCZ positions are correct and fix them in the inversion. Moreover, as shown in Figure 4.8, the initial model for the base salt also changes with the perturbation. Following inversion for each of these perturbed models, the recovered models for base salt corresponding to different top-salt perturbations are shown in Figure 4.9, and the differences between the best-estimated and the recovered depth of base salt in Figure 4.10. Because shifting the top salt upward adds more salt above the true top salt, the recovered base salt loses the keel-shaped feature to fit the introduced anomaly. On the other hand, shifting the top salt downward leads to a deeper keel. The constant error in top salt also introduces complex structures into the recovered base salt (Figure 4.10), which can lead to erroneous interpretation, and as we shall see, degraded seismic imaging of the section beneath the salt. The RMS differences for all perturbations between the best-estimated model and the recovered models are summarized in Figure 4.11. Note the asymmetry of the curve, i.e., shifting the top salt upward leads to larger error in the base salt than does shifting downward by the same amount. This is again because gravity data are more sensitive to shallower features. Because the imaging error in top salt is less than 100 m for good quality of data, a 200-m perturbation to the top salt is a large amount in practice. The evaluated errors shown here suggest that a possible large error in base salt may occur caused by the DC-shift error in top salt. Meanwhile, the maximum error in Figure 4.11 caused by the reasonable top-salt error ($\leq$ 100 m) is smaller than 170 m, which is small, comparing with the errors caused by HCZ error ($\leq$ 5% in general) shown in Figure 4.6.

4.3 Error in density contrast

In practice, the background density in the sedimentary host is typically obtained from density logs in sparsely located wells in the general vicinity of the salt body. A single density profile is often used throughout an entire 3D model region even though the background density may well be laterally variable. The single well measurement may not be an accurate enough representation of the density for the area. Incorporating inaccurate density information in gravity inversion will cause error in the recovered model. In this section, I introduce a simple error in the background density by perturbing the density contrast to

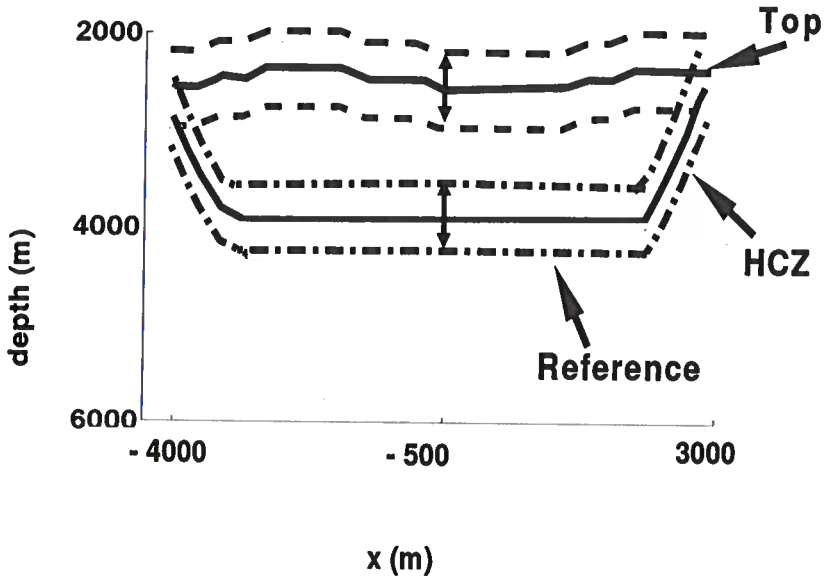

Figure 4.8. 2D cross-section through the 3D salt model showing the top salt and perturbations. The dotted lines represent the limits of the perturbed top salt and the dash-dotted lines represent the corresponding changed HCZ and base salt in the initial model.

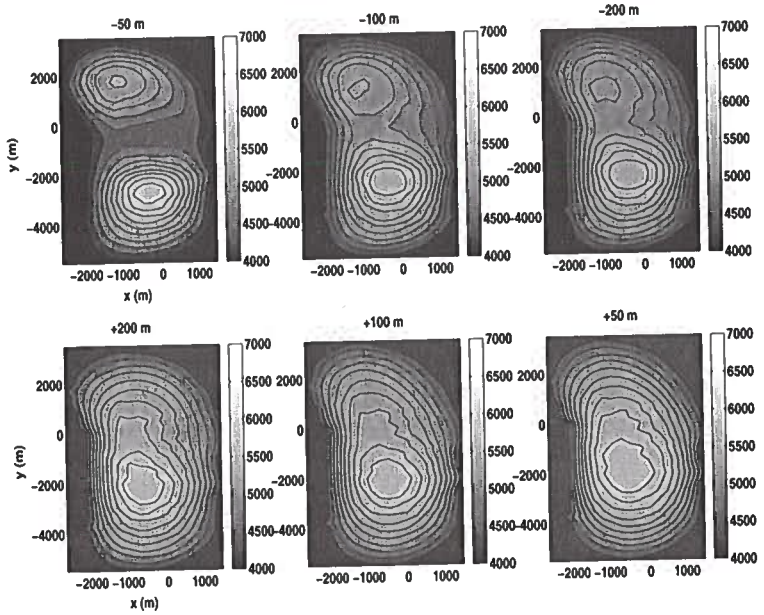

Figure 4.9. Recovered depth of base salt (m) for different incorrect depths of top salt. The numbers shown on the top of each panel represent the perturbation of the top salt.

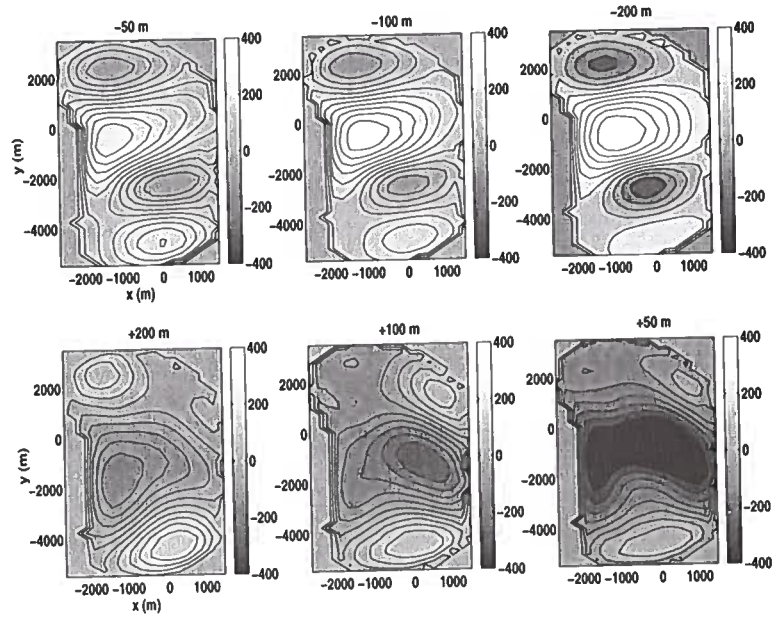

Figure 4.10. Difference in depth of base salt (m) between that for the best model and those for models using incorrect top salt. The numbers shown on the top of each panel represent the perturbation of the top salt.

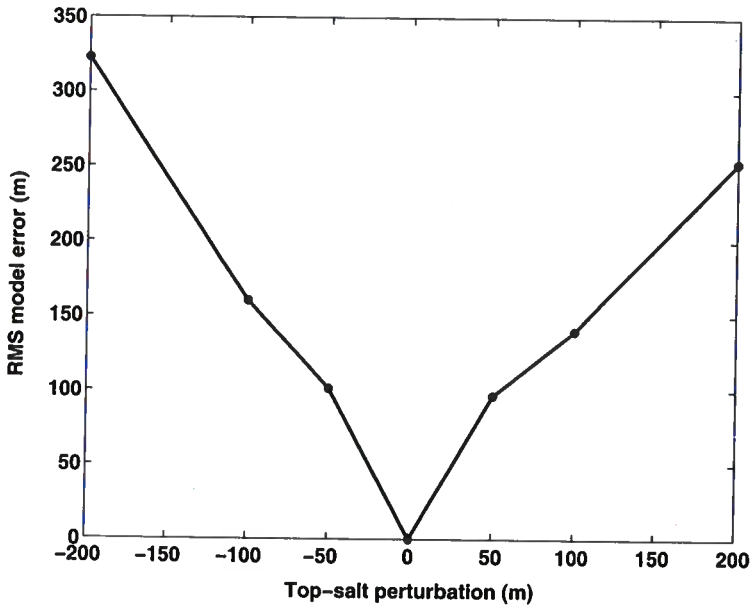

Figure 4.11. RMS base-salt depth difference between the best estimated model and models with incorrect top salt position.

evaluate the influence of this kind of error on the recovered base salt.

I carry out a sequence of simulations by perturbing the density contrast as a function of depth in Figure 2.8 by ±10% and ±20% (Figure 4.12), while keeping the HCZ and top salt at their correct position. Figures 4.13 and 4.14 show the plan-view contour plots of recovered depth of base salt and the difference between the depth for the best model and the models recovered with incorrect density contrast. The influence of error in the density contrast is relatively simple — the depth of the base of salt increases as the density contrast decreases — but no complex structure is introduced (Figure 4.14). The explanation for these trends is that when the density contrast is underestimated, more salt is required to fit the gravity anomaly. Figure 4.15 shows an asymmetric curve of RMS difference as a function of the density contrast. Because the gravity anomaly corresponding to the underestimated density contrast is negative, the base salt is extended deeper to fit the data. Since the amplitude of gravity anomaly is inversely proportional to the square of the depth of the masses, more salt is needed than when the density contrast is overestimated. Further, a 10% error in density contrast, which is reasonable small error to expect in practice (Starich et al., 1994), leads to an RMS error of about 300 m. A small error in density can thus introduce large error in the base salt. Compared to the RMS errors in recovered base-salt depth caused by incorrect HCZ and top salt, the errors in recovered base-salt depth due to incorrect density may be the most severe problem in practice.

In summary, an accurately estimated sedimentary density is key to successful gravity inversion. In practice, therefore, one must collect as much information as possible to define

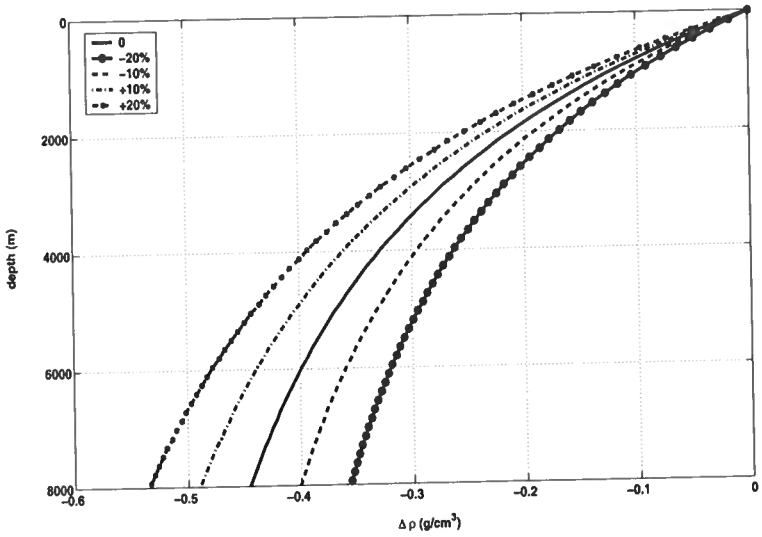

Figure 4.12. Perturbation of density contrast by $\pm 10\%$ and $\pm 20\%$. $\Delta\rho_0$ denotes the correct density contrast.

the density contrast acceptably prior to applying gravity inversion. Furthermore, it might be better to err on the side of overestimating the magnitude of density contrast since it leads smaller error in the inverted model.

4.4 Summary

Using this newly developed algorithm, I have quantitatively assessed the errors in the inverted depth of base salt produced by three different types of prior information for gravity inversion. Seemingly small errors in these input parameters can lead to significant errors in the recovered base salt. The results also demonstrate that underestimating any one of the three input factors produces larger error in base-salt depth than does overestimating them. This is attributed to the larger sensitivity of gravity data to the shallow features than to deep ones. One must provide these input parameters that are as accurate as possible, and especially avoid underestimating them, in order to enhance the reliability of inverted depths for base salt. The error curves here provide an indication of errors to be expected in the inverted base-salt depth in practical applications, and serve as a guide to data preparation so that the inverted base salt can aid in seismic imaging of base salt and, thereby, of subsalt structure.

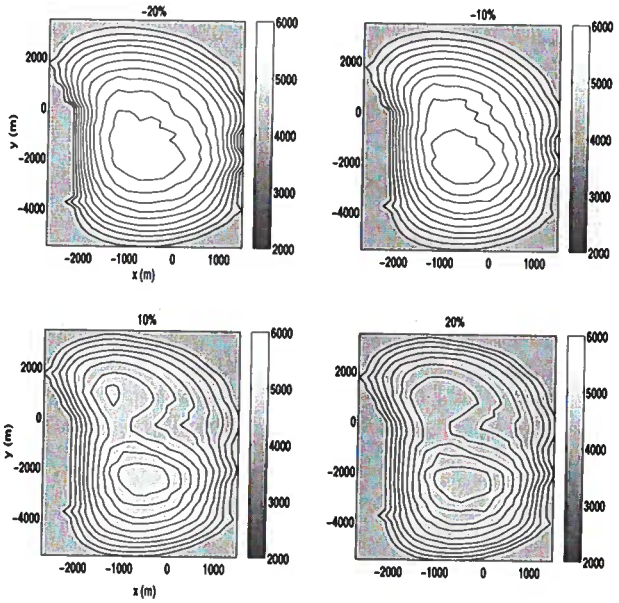

Figure 4.13. Recovered depth of base salt using incorrect density contrast. The numbers shown on the top of each panel represent the perturbation of the density contrast in percentage of the true density contrast.

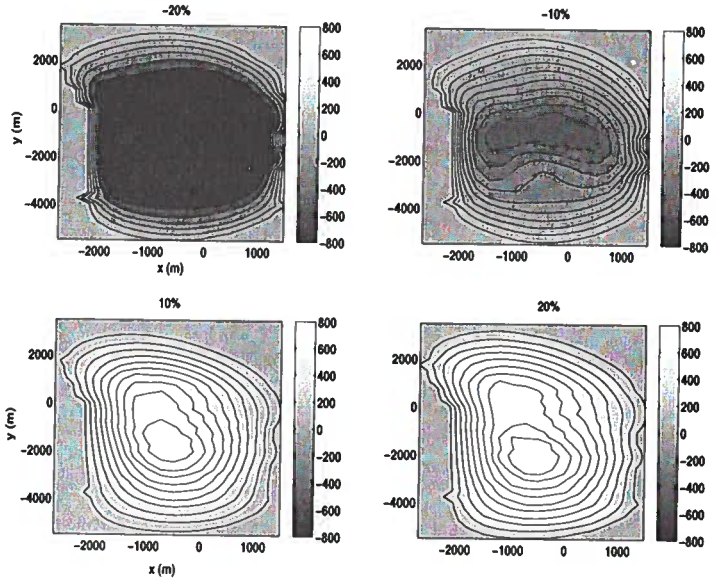

Figure 4.14. Base-salt depth difference between the best estimated model and models using incorrect density contrast. The numbers shown on the top of each panel represent the perturbation of the density contrast in percentage of the true density contrast.

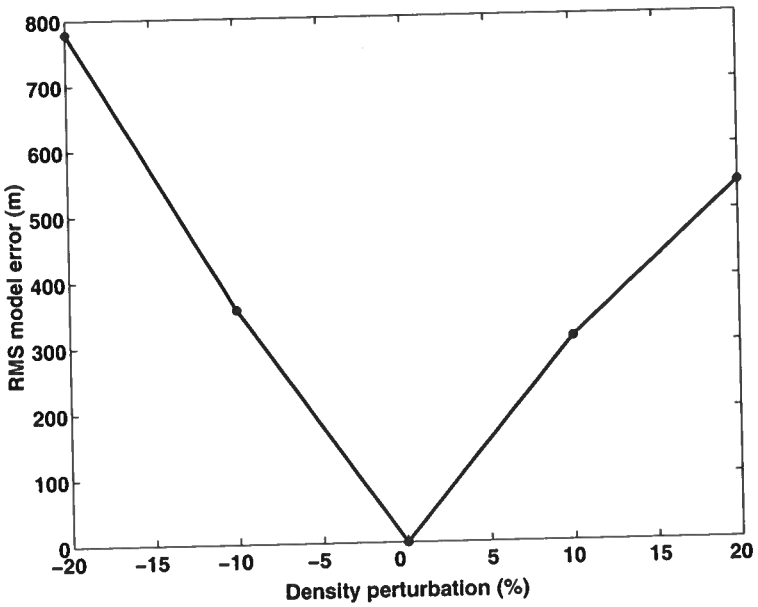

Figure 4.15. RMS depth difference between the best model and models with incorrect density contrast.

Chapter 5

Sensitivity of subsalt seismic imaging to erroneous base salt

In this chapter, through a seismic synthetic example, I evaluate an aspect of the feasibility of applying gravity inversion to aid in subsalt seismic imaging. To do this, I choose a vertical 2D cross section through the 3D salt model (Figure 5.1) studied above and fabricate a 2D acoustic velocity model that passes through the center of the keel-shaped structure. The cross-section for this model, shown in Figure 5.2, has a velocity distribution similar to that of the SEG/EAGE salt model (e.g., Aminzadeh et al., 1994). The irregular salt body, located in the central area of the velocity model, has a constant velocity of 4500 m/s. In addition to the salt body are three flat reflectors. The horizontal water bottom lies above the salt body at a constant depth of 1200 m, and the water velocity is set at 1500 m/s. Below the salt are two reflectors: S_1 is at a depth of 6000 m, and S_2 is a dipping plane reflector whose depth varies from 6500 m to 7000 m. The velocities in the layers above and below S_2 are 4000 m/s and 4500 m/s. The velocity of the sediments enclosing the salt between the water bottom and S_1 is given by

$$v(z) = 2000 + 0.3125(z - 1200) \qquad \text{m/s}, \tag{5.1}$$

where $1200 \leq z \leq 6000$ m. Based on this model, I first assess how well gravity inversion can help subsalt imaging if the gravity data are contaminated by additive random noise. To address this problem, I assess the depth error of prestack migrated images of subsalt features when the base salt recovered in the first numerical example in Chapter 2 (Figure 2.11) is adopted to construct the migration-velocity model. Second, to examine the influence of errors in the assumed-known prior information in gravity inversion on subsalt imaging, I conduct a sequence of seismic migration experiments in which a number of erroneously inverted estimates of base salt are set in the sedimentary velocity models, and then assess the quality of 2D depth-migrated images of the subsalt features.

5.1 Synthetic seismogram and migration

In this section, I discuss the approach used to create synthetic seismic data and seismic migrations.

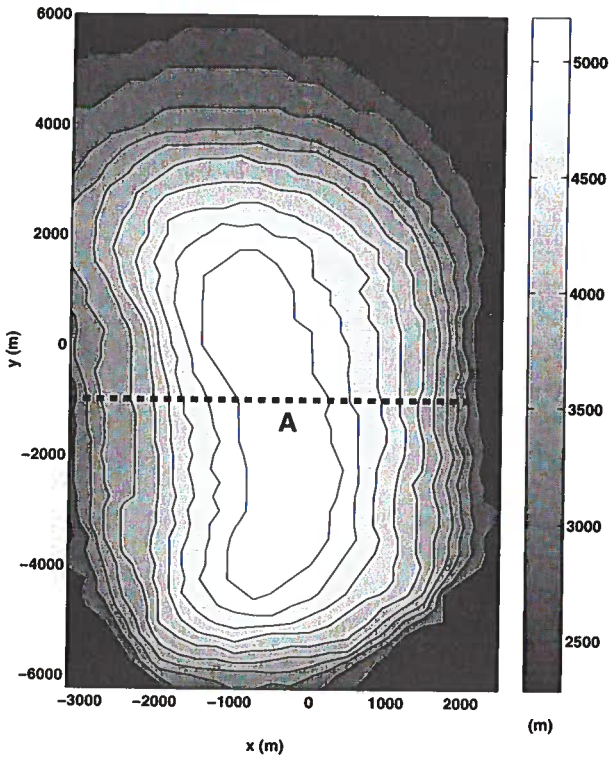

Figure 5.1. Plan view showing the location of the 2D cross-section (dashed line) through the model used for the tests of seismic imaging. Contoured here is the depth of the base of the salt model.

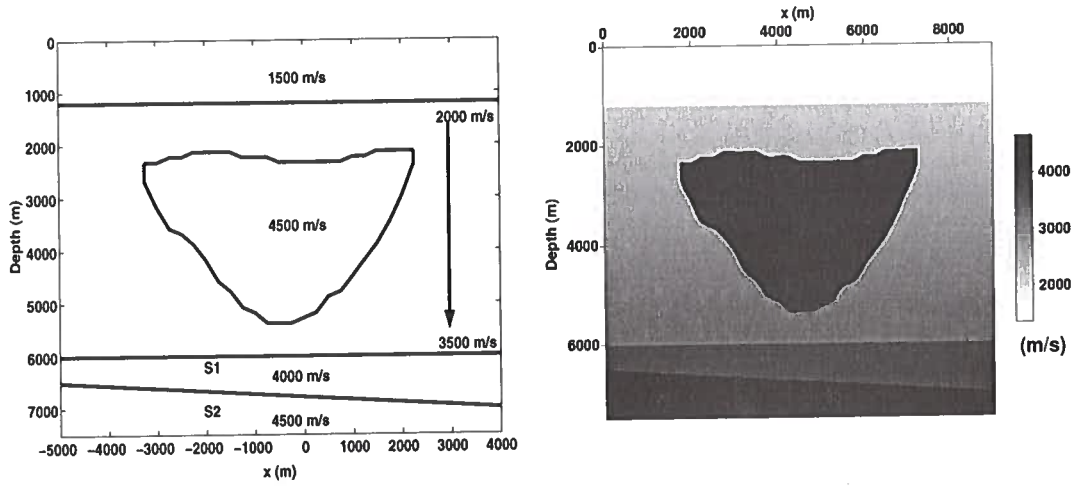

(a) Velocity model.

(b) Velocity model displayed in gray scale.

Figure 5.2. Acoustic velocity model, which extends 9000 m laterally and 7500 m vertically.

5.1.1 Seismic forward modeling

First, to obtain observations over the acoustic velocity model, I generate a set of synthetic seismic data using 2D finite-difference (FD) modeling with flux-corrected transport (FCT) (Fei, 1994). As compared with the conventional FD approach, this method requires fewer points per wavelength of the upper half-power frequency (e.g., Scales, 1995) for the same order of operator. Alford et al. (1974) and Kelly et al. (1976) state that to eliminate the numerical dispersion in conventional FD methods requires at least 11 points per wavelength of the upper half-power frequency for the second-order and 5.5 points for the fourth-order operator. In contrast, Fei (1994) points out that the FCT method can produce comparably accurate results with only 5 points per wavelength of the upper half-power frequency for second order and 3.7 points for fourth order. Therefore, the FCT method improves the efficiency of computation.

Here, I adopt the fourth-order FCT method, and specify a Ricker source wavelet having peak frequency of 27 Hz. Considering the computation cost, I use 2.7 points per wavelength of upper half-power frequency rather than 3.7 points. Fei (1994) has shown that 2.7 points per wavelength of upper half-power frequency can give an acceptable result. Accordingly, I discretize the model into a grid of contiguous squares, with cell size of 15 m $\times$15 m. The snapshots of the wavefield in Figure 5.3 indicate no strong numerical dispersion with this setup. Also, Figure 5.4 shows three shot records, whose sources are located at 300 m, 4500 m and 8700 m in the x-direction, with no obvious dispersion present. Apparently, then, this parameterization of the forward modeling is acceptable. To emulate field-scale data, I used the acquisition parameters for the synthetic data shown in Table 5.1. The zero-offset

Parameter	Value
no. of shots	300
shot spacing	30 m
group interval	15 m
maximum offset	3000 m
sampling interval	4 ms
record length	9 s

Table 5.1. Acquisition parameters for modeled data.

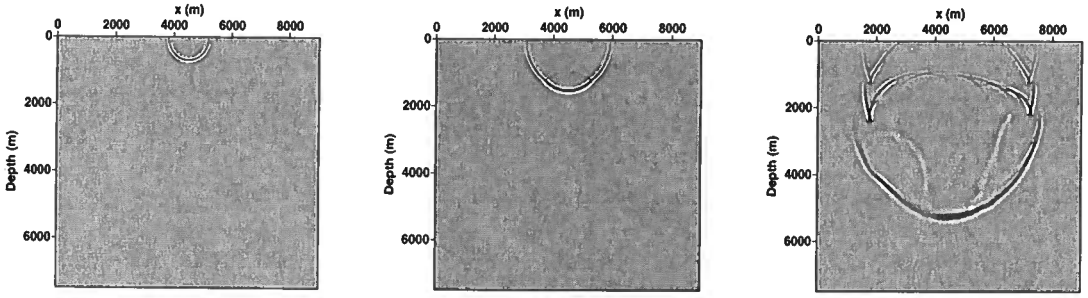

(a) 500 ms (b) 1000 ms (c) 2000 ms

Figure 5.3. Depth-section showing snapshots of the wavefield at different times computed by the FCT-corrected FD method. The source is located at the surface and 4500 m in the x-direction.

section obtained with these parameters, in Figure 5.5, displays clear reflections without severe numerical error. The features diagonally crossing over the section are artifacts from incompletely absorbing boundaries at the vertical sides of the model.

5.1.2 Seismic migration

I did tests with both finite-difference and Kirchhoff approaches to prestack depth migration. Based on comparison tests, my choice for subsequent portions of the study was to use Kirchhoff prestack depth migration (coded in SUKDMIG2D in SU, Liu, 1993). Kirchhoff migration is a ray-based or high-frequency method. Its advantage is that it is computationally much faster than the finite-difference method, while retaining generally good quality of imaging. The Kirchhoff method, however, has shortcomings for models with strong velocity contrast; the velocity model must be smoothed to minimize artifacts from the ray tracing. Even then, it has difficulties in the presence of multi-pathing. To smooth the velocity model illustrated in Figure 5.2, I apply the damped least-square method

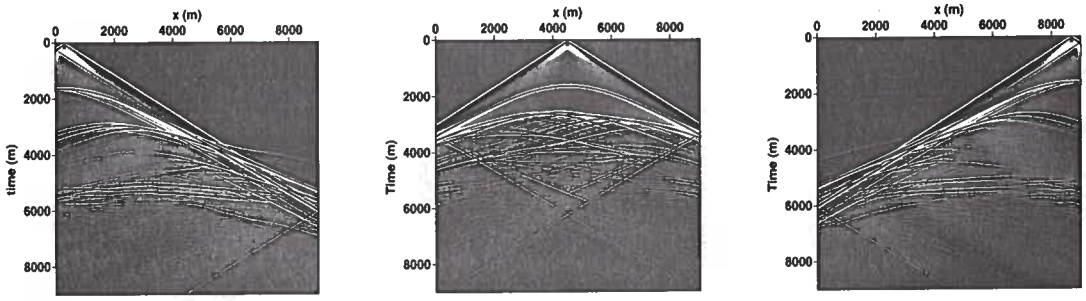

(a) (b) (c)

Figure 5.4. Shot records obtained at different source locations using FCT-corrected FD. The sources are located at x-coordinate (a) 400 m, (b) 4500 m, and (c) 8700 m.

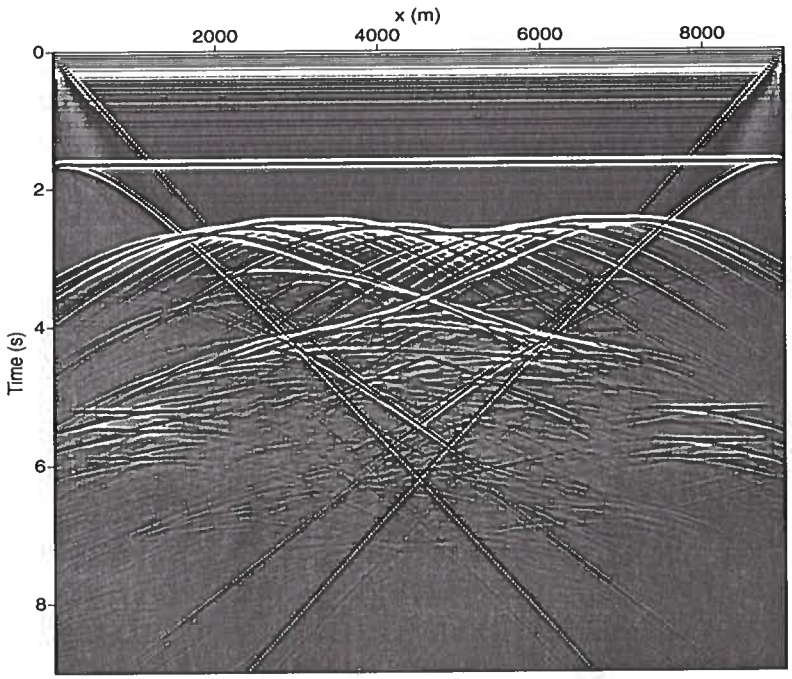

Figure 5.5. Zero-offset seismic data.

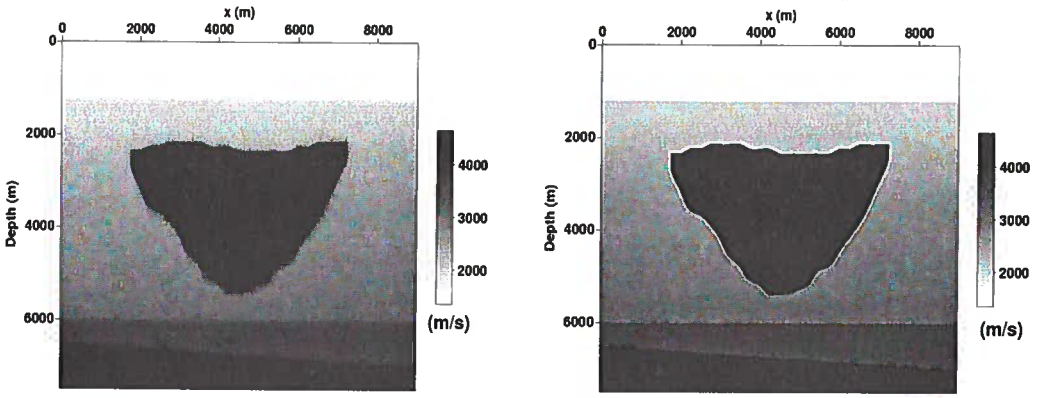

(a) (b)

Figure 5.6. (a) Velocity model smoothed with a two-dimensional operator having the length of nine points in both the x-and z-directions, and (b) the unsmoothed velocity model.

of Liu (1993), which is similar in action to a two-dimensional Gaussian spatial smoothing filter.

The traveltimes for the Kirchhoff method are obtained via paraxial ray-tracing. A model smoothed with nine points, i.e., 120 m, in both x- and z-directions, yields good imaging quality without excessively changing the velocity model for the models studied. Figure 5.6 shows both the smoothed and unsmoothed velocity models. I fix the length of smoothing window hereafter at 120 m in both x- and z-directions.

Considering the computation cost, a main concern is whether or not the imaging of zero-offset (or, any single common-offset) data can provide acceptable images of subsalt features because prestack migration, which involves many offsets, costs much more than does poststack migration. Figure 5.7 shows common-offset depth-migration profiles for a range of offsets. The images of the subsalt features for all the offsets show large discontinuities, with distortions that vary with offset. Since the imaging of zero-offset data is based on the exploding-reflector model, one possible source of the discontinuities is the multi-pathing problem, such as may happen in zero-offset data at the edges of salt as in Figure 5.8. This might be the reason why the quality of the subsalt imaging of zero-offset data is poorer than that for much of the nonzero-offset data, as seen in Figure 5.7. Migrated zero-offset data by finite-difference migration (Fei, 1994) in Figure 5.9b, however, shows that both the finite-difference and Kirchhoff methods yield a similar pattern of discontinuities. These shortcomings in imaging for each offset are thus likely caused by shadow zones beneath the edges of the salt (Muerdter et al, 1996), and cannot be attributed to the choice of migration

approach used.

In contrast, prestack migration using a wide range of offsets produces much better quality of subsalt imaging. Figure 5.10 shows a prestack Kirchhoff depth-migration profile obtained using 100 offsets from 0 to 3000 m. The image of the subsalt features has much better quality than that in any single common-offset result in Figure 5.5 although it too exhibits artifacts in these features. A reason is illustrated by the common-image gather in Figure 5.11. The coherence for both S_1 and S_2, which varies with offset, is somewhat higher at far offsets than at near ones. The regions of weak amplitude can be attributed to the problem of shadow zones. Concentrating attention on raypaths near the left flank of the salt in Figure 5.12 shows that the rays from the three sources poorly cover the area (marked by the circle) where the subsalt reflectors are also poorly imaged. Being out of the scope of this study, I will leave this illumination problem open for future study. The averaging of results for a range of offsets in prestack migration improves the subsalt imaging quality because the locations of the imaging shortcomings associated with shadow zones varies with offset. Although the imaging quality of deep reflectors still is imperfect, it is now good enough to study the influence of choice of model for the salt body on subsalt imaging. Subsequently, all the experiments of subsalt imaging are based on results of full-offset prestack depth-migration by the Kirchhoff method.

5.2 Dependence of subsalt seismic imaging on the shape of the salt body estimated from inversion of gravity data

The numerical examples in Chapter 2 illustrate that gravity inversion can improve the definition of the base of salt as compared to that of the initial model, which might have been assumed based on none-to-good prior knowledge of the base salt. Then the question arises as to whether the subsalt imaging can be improved by applying a model recovered by gravity inversion. To answer this question I compare prestack migration results using the initial base salt and the base salt recovered by gravity inversion. Because additive random noise generally is present in the gravity observations, the base salt I choose for the recovered model is from the first numerical example (Figure 2.11) in Chapter 2, in which the base salt is inverted from data contaminated by uncorrelated white random noise having a standard deviation of 0.1 mGal. Since the best image of all features is that obtained when the true salt model is used in the migration-velocity model, I use the depth image of the subsalt reflectors in Figure 5.10 as the standard for comparison of the imaging results for other models tested.

In the tests, as shown in Figure 5.13, I first work with two velocity models, one containing the initial base salt and the other the one recovered from 3D gravity inversion. Then I smooth the velocities in these two models using the smoothing parameters described above and apply prestack Kirchhoff depth migration. The resulting depth-migration profiles are shown in Figure 5.14. In both profiles, the salt body and the subsalt features are clearly imaged. For the initial model, the deep portion of salt is absent and replaced by the low-velocity background medium; as a result, the computed traveltimes are much larger than the true values. Therefore, the subsalt image in Figure 5.14a exhibits a large subsalt pull-up

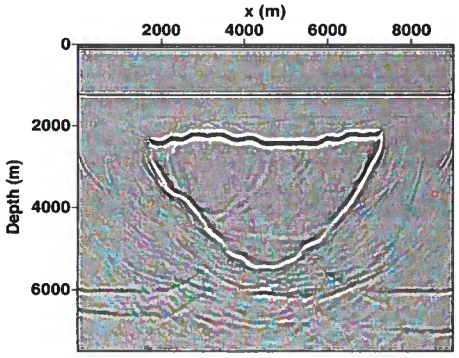

(a) offset: 0 m

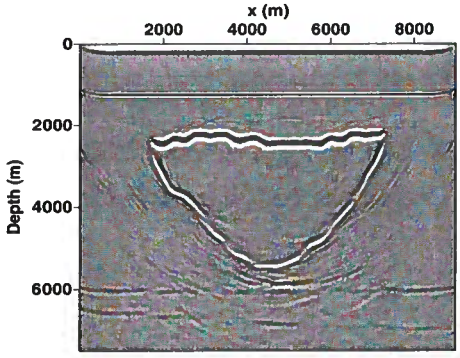

(b) offset: 1005 m

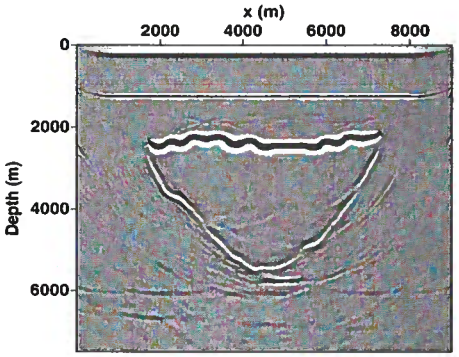

(c) offset: 1500 m

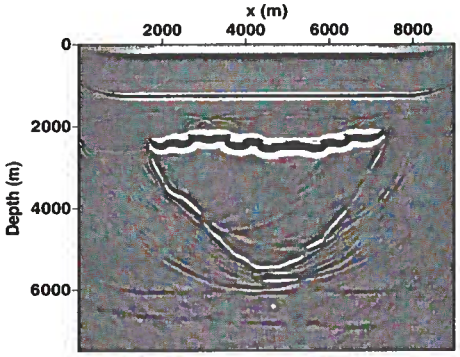

(d) offset: 1995 m

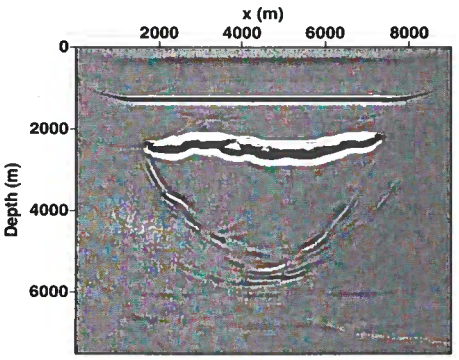

(e) offset: 2505 m

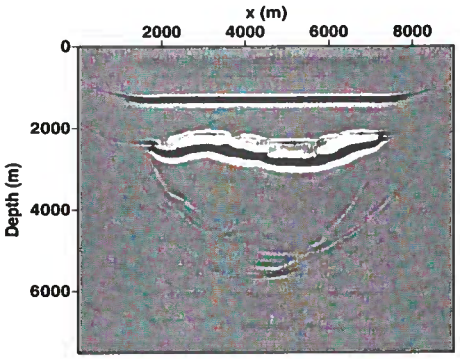

(f) offset: 3000 m

Figure 5.7. Seismic sections by common-offset Kirchhoff migration with the true velocity model.

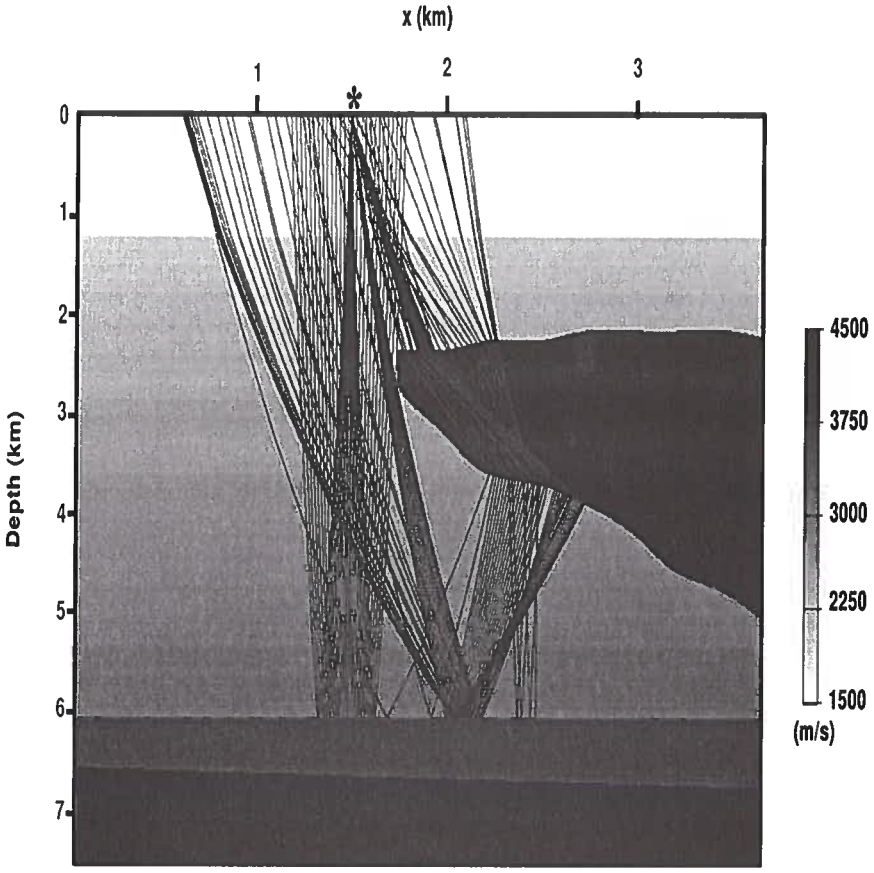

Figure 5.8. Depth-section with reflection raypaths superimposed on a velocity model. The rays from the source located at 1.5 km (denoted by the asterisk) illustrate the multi-pathing problem at the edges of the salt; i.e., the high-velocity region toward the right.

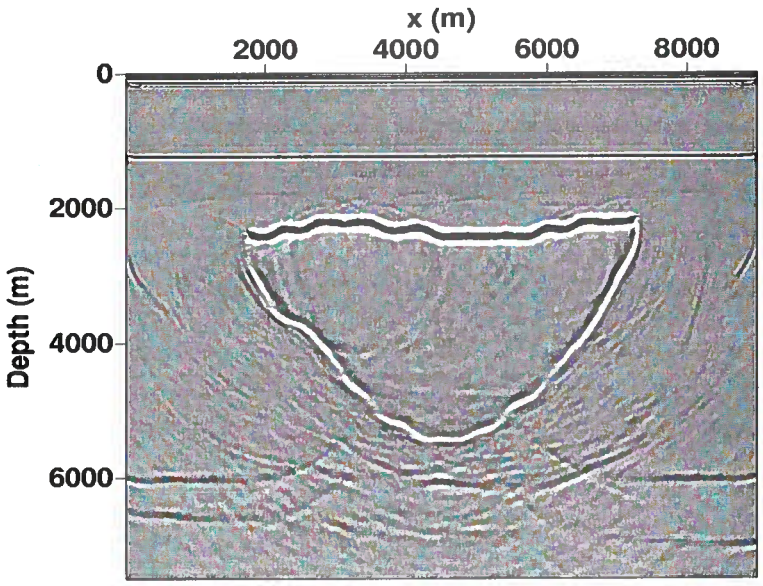

(a)

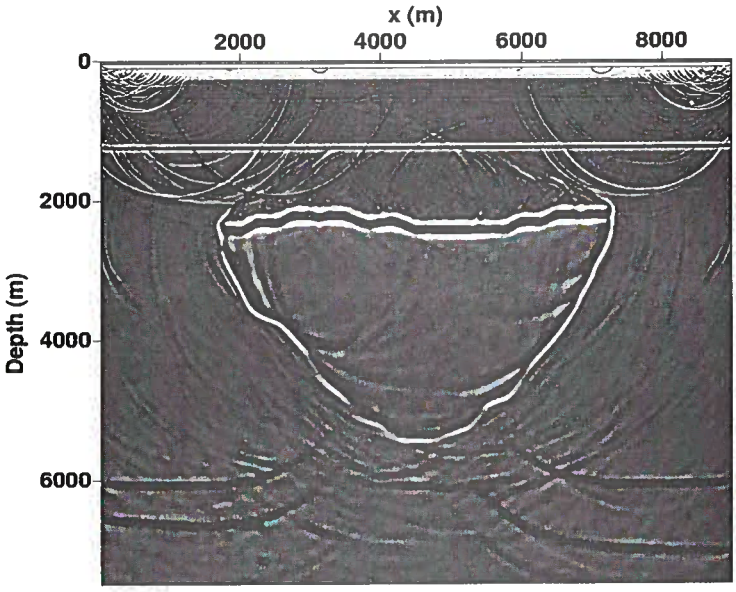

(b)

Figure 5.9. Zero-offset migration by (a) the Kirchhoff method, and (b) the finite-difference method

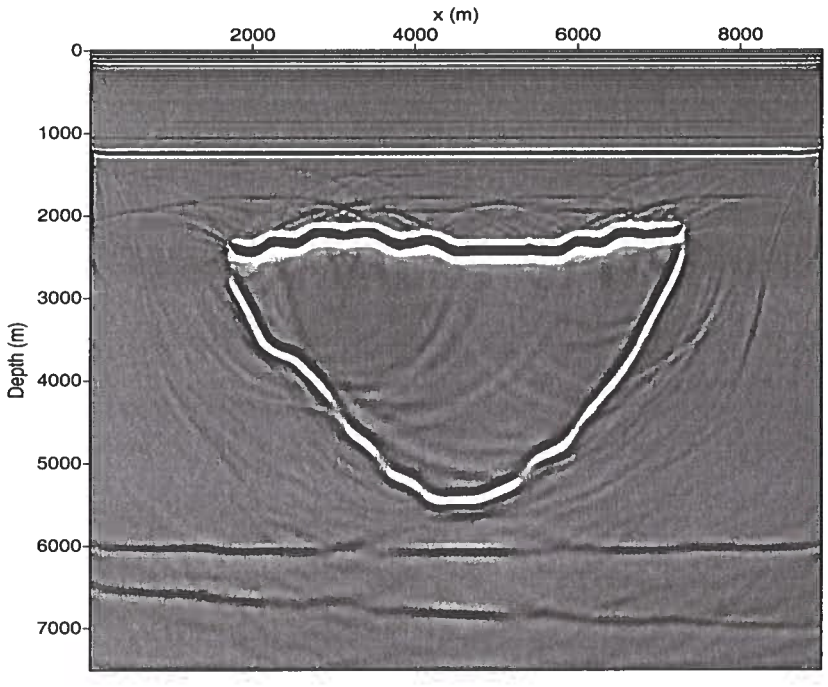

Figure 5.10. Prestack migration profile using the true velocity model.

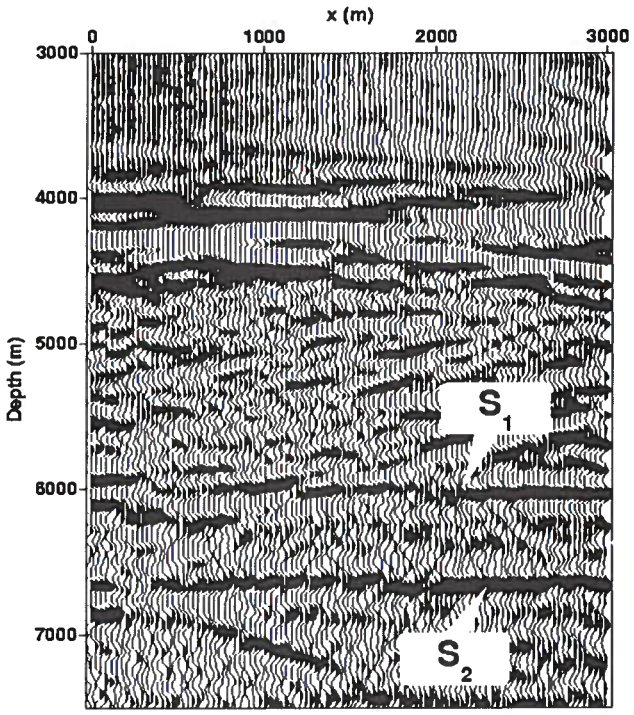

Figure 5.11. Common-imaging gather (AGC applied) at x-coordinate 3000 m. The imaging quality for both S_1 and S_2 is higher at far offsets than near, perhaps because large-offset raypaths traverse the salt body only once.

feature, directly beneath the salt, without loss of continuity. In contrast, the imaging using the recovered model gives a more nearly accurate shape for the subsalt reflectors (Figure 5.14b), although the base salt in the recovered velocity model differs from the true position. Because use of the initial model leads to much larger error for the subsalt images than does that of the recovered model, the gravity inversion has helped improve subsalt imaging in this test, with the data contaminated by uncorrelated additive random noise.

Also, let us recognize a possible discrepancy here. Basically, we have assumed that the initial base salt was obtained from unclear seismic imaging. The seismic image of the base salt, however, is quite clear in Figure 5.14 even when the highly erroneous initial base salt is used in the model for migration velocities. This is contradictory to the assumption that initial seismic imaging failed to give a clear reflection from the base of salt. Since the causes of poor imaging of base salt are complicated and out of the research scope of this study, I shall assume that base salt was not clearly imaged in the original seismic processing and focus only on the improvement of subsalt imaging when a better-defined base salt is applied.

5.3 Imaging error due to error in bathymetry

I concentrate next on distortions in subsalt imaging that can be introduced by various errors in our models of the overburden. First, let us suppose that the bathymetry information is inaccurate, thereby contaminating the inversion of the gravity data for the shape of the base salt. I created two velocity models containing the base salt recovered from 3D inversion of the gravity data contaminated by the minimum ($\sigma_{bat} = 5$ m) and maximum ($\sigma_{bat} = 20$ m) bathymetry errors treated in Chapter 3. Because the best-estimated model and migrated image of deep reflectors are those obtained from the noise-free data in Figure 3.14, I use for comparison the best velocity model and corresponding migration profile in Figure 5.15.

The velocity models with the base salt inverted from gravity data contaminated by inaccurate bathymetry correction are shown in Figure 5.16. Following smoothing of the inverted models and prestack Kirchhoff depth migration, Figure 5.17 shows the corresponding migrated results. Because the HCZ is correctly defined here, errors in subsalt imaging are caused mainly by the error in the central unknown portion of the base salt. Because the base salt is distorted more when the standard deviation of bathymetry error is 20 m than when it is 5 m, the image of subsalt features in Figure 5.17b has larger distortion than in Figure 5.17a (compare both with the image in Figure 5.15b). Also, because the 2D cross-section passes through an area of the model with relatively small errors for base salt (Figure 3.15), the error in the subsalt images is not pronounced, though the standard deviation of 20 m is sizable. One could expect larger errors in subsalt imaging in portions of the inverted 3D salt model with large errors for base salt caused by erroneous bathymetry. Nevertheless, the images of subsalt features in Figure 5.17 show more error from the correct image in Figure 5.10 than does the best-estimated image in Figure 5.15b. Therefore, the bathymetry error can be considered an important source of error subsalt imaging.

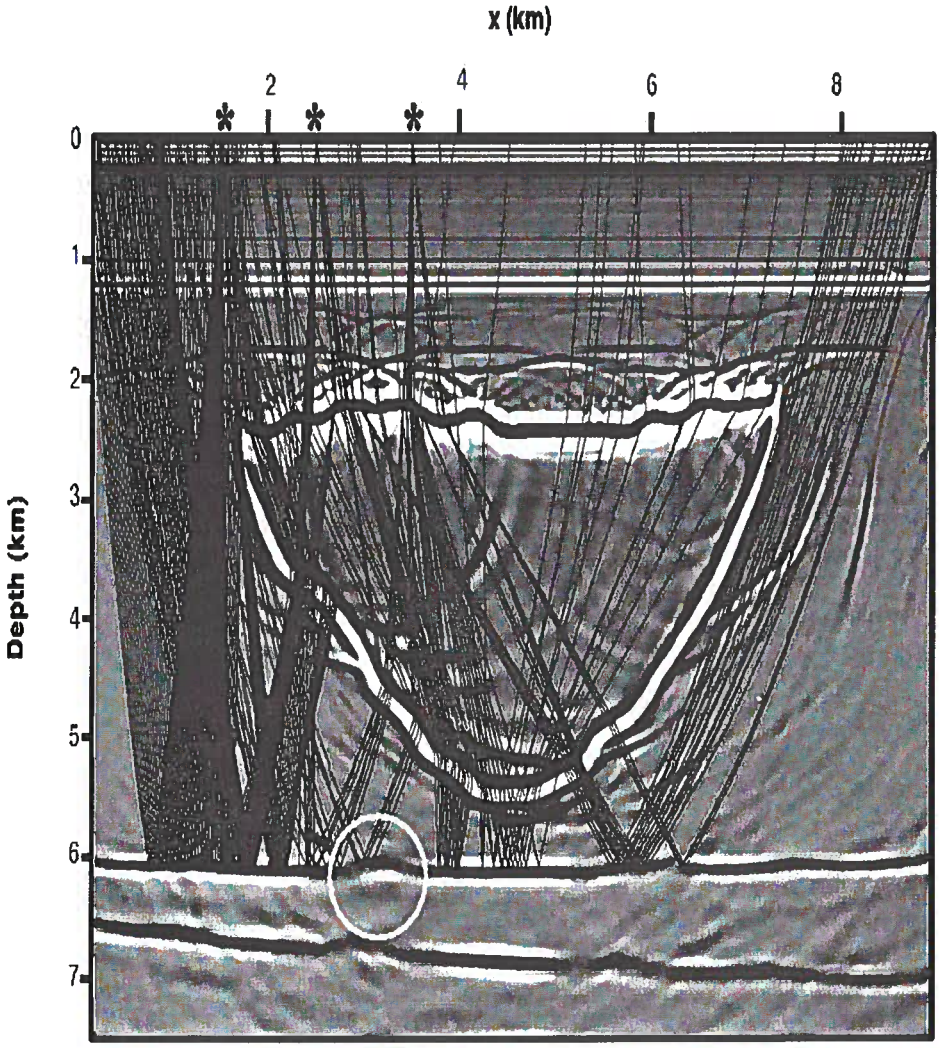

Figure 5.12. Prestack migration profile with rays from three sources marked by "*" superimposed. The rays have poorly covered the area marked by the white colored circle, where the imaging quality is poor.

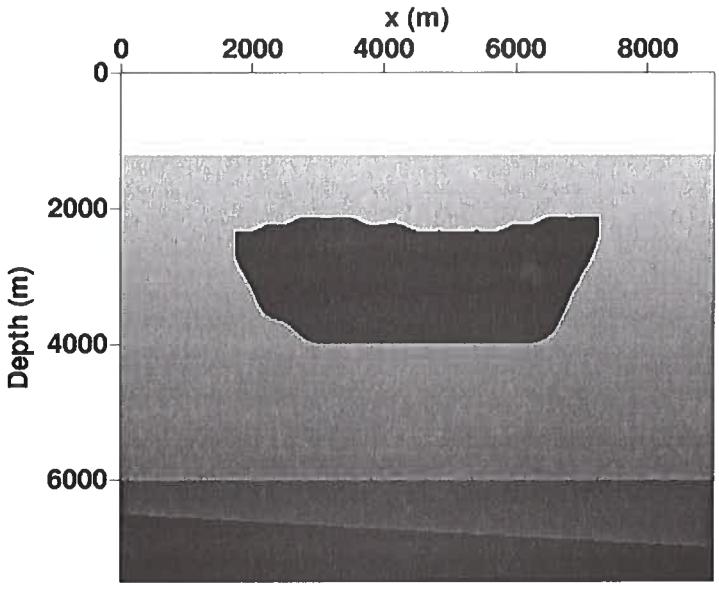

(a)

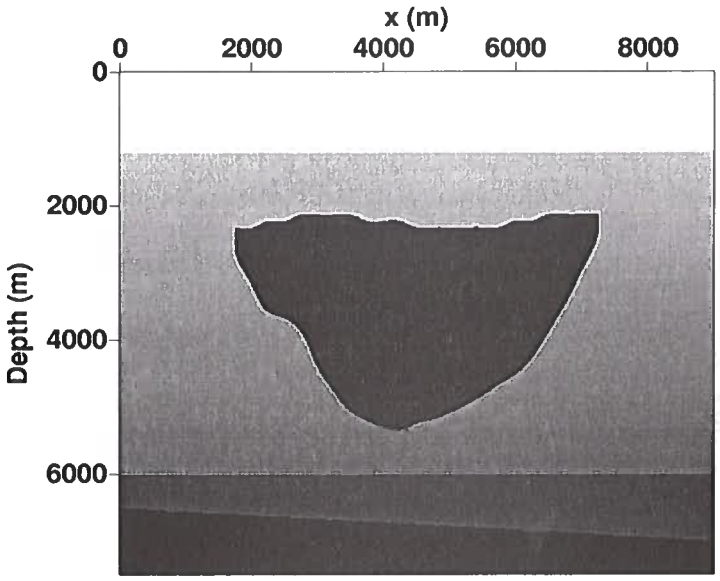

(b)

Figure 5.13. Velocity sections containing: (a) the initial base salt, and (b) the recovered base salt (see Figure 2.11) based on inversion of gravity data contaminated by random noise.

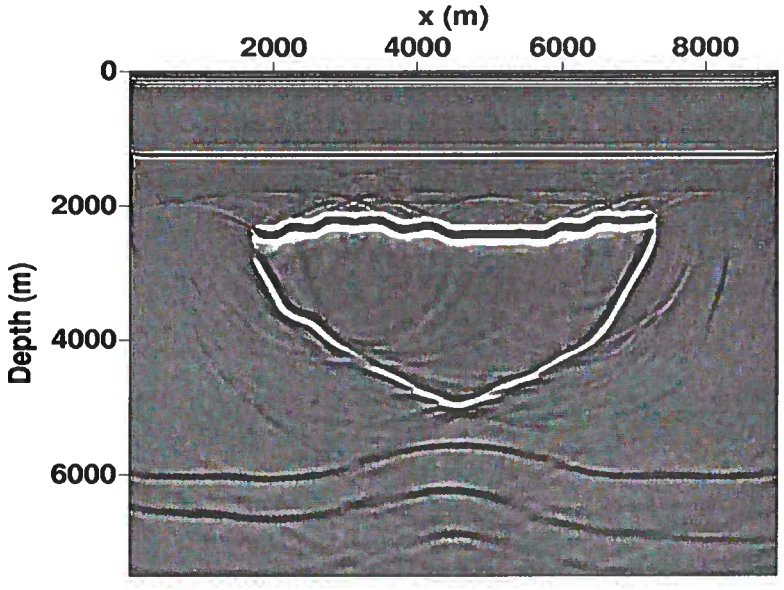

(a)

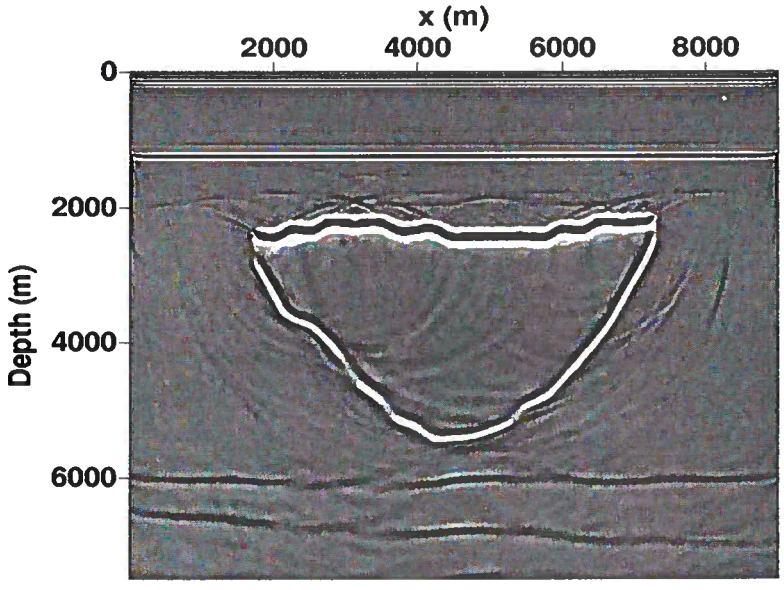

(b)

Figure 5.14. Migration results obtained by using smooth versions of the velocity model containing (a) the initial base-salt model, and (b) the recovered base-salt model.

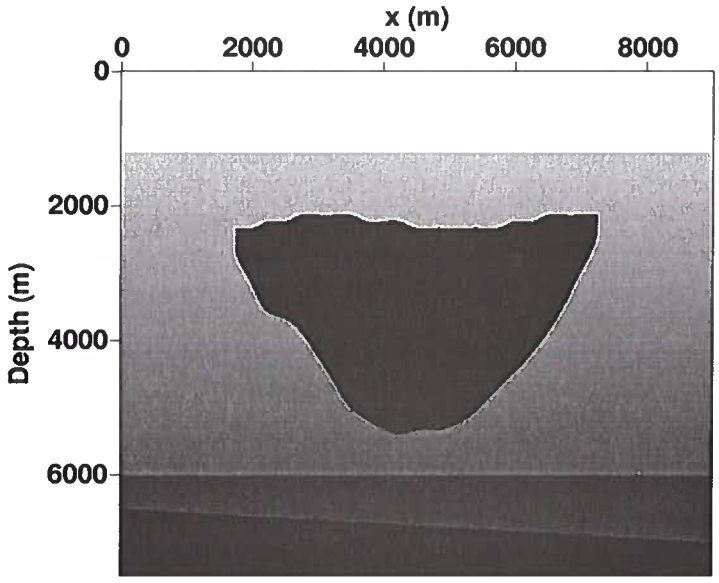

(a)

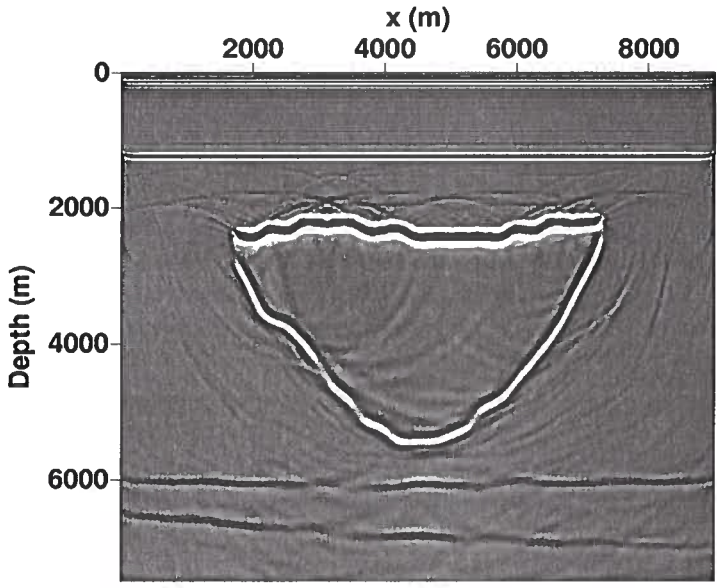

(b)

Figure 5.15. (a) Velocity-depth section for the salt model inverted from error-free data, and (b) the prestack migration result based on this model.

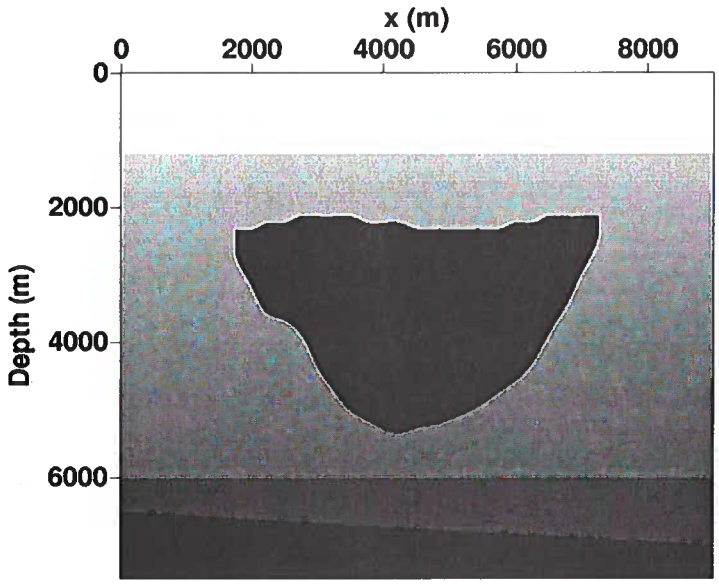

(a)

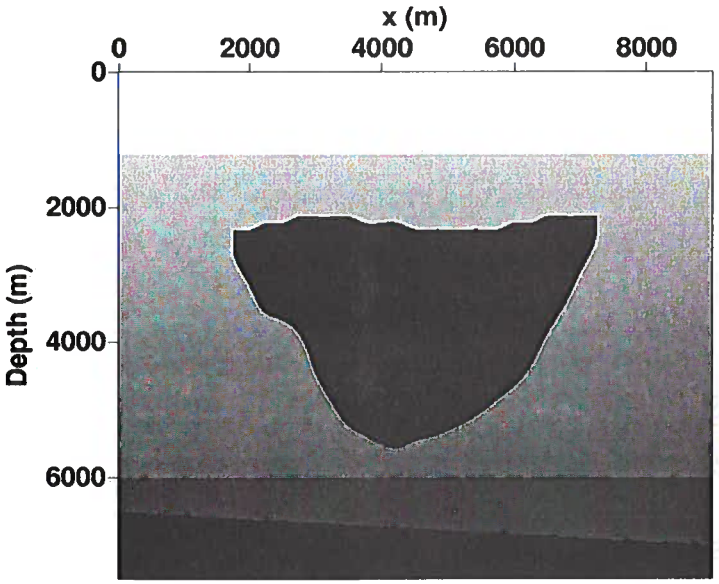

(b)

Figure 5.16. Inverted velocity models obtained from data with bathymetry errors of (a) 5-m and (b) 20-m standard deviation.

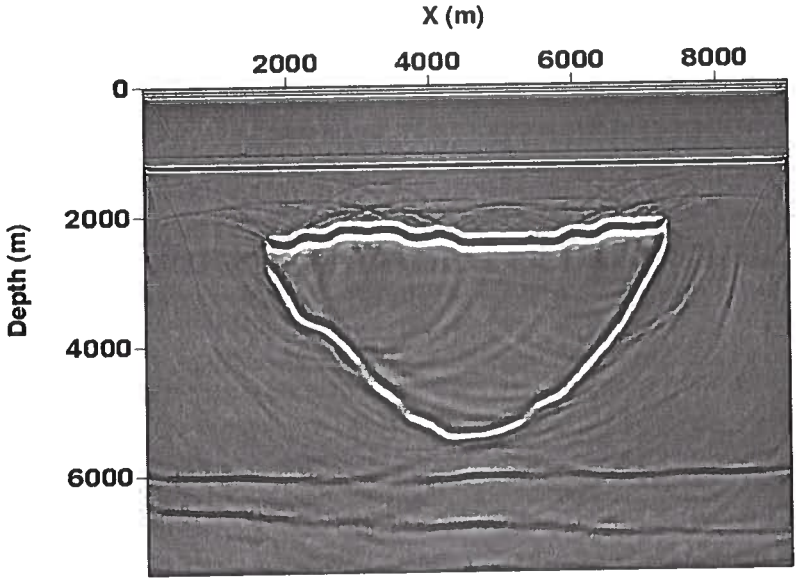

(a)

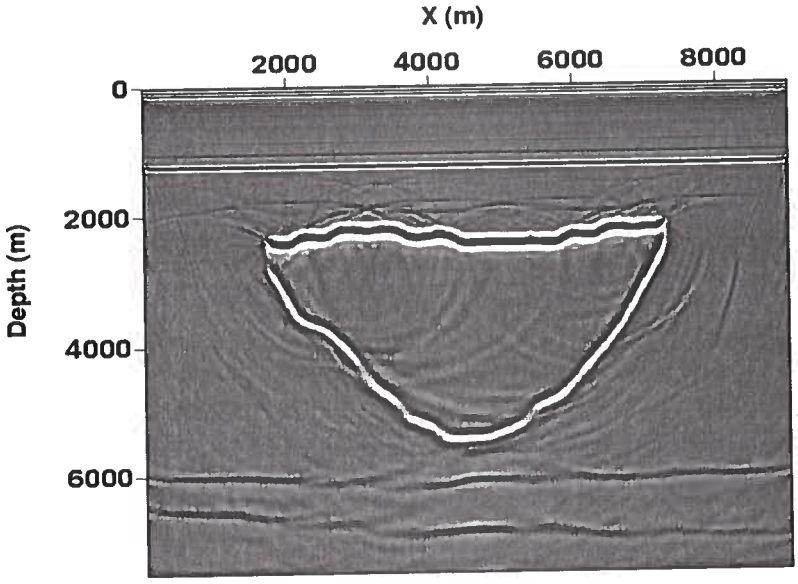

(b)

Figure 5.17. Prestack migration results for bathymetry errors having (a) 5-m and (b) 20-m standard deviation.

5.4 Imaging error due to errors in prior information

In this section, I assess the sensitivity of subsalt imaging to errors in presumed prior information, in particular in the HCZ, top salt, and density. Since the input data in Chapter 4 are contaminated by uncorrelated Gaussian random noise having standard deviation of 0.1 mGal, I use the migration result in Figure 5.14b hereafter as the reference best achievable image for subsequent comparison.

5.4.1 HCZ error

Recall that in inversion for the base salt, one might sometimes presume and fix the position of a portion of the flank of the salt feature. Such a portion, the HCZ, may nevertheless have error. To measure the influence of error in the HCZ, I use migration-velocity models (Figure 5.18) containing two different inverted results for the base salt, corresponding to the models in Figure 4.4 with largest HCZ error, i.e., $\pm 10\%$ of the depth of the HCZ. The maximum error of the HCZ is 400 m. As above, after prestack depth migration using a smoothed version of the inverted velocity model, I obtain the migration results shown in Figure 5.19. In Figure 5.19a, the events of the subsalt features in the inverted portion are pulled up because of the missing salt, whereas the portion directly under the HCZ is pushed down because of the extra salt. The results in Figure 5.19b, however, show opposite behavior because the HCZ is shallower than the correct position. Again, since the 2D cross-section does not pass through the areas in the salt model where the error in base salt is large, the images of subsalt features do not show significant difference relative to the correct subsalt images in Figure 5.10 and the best-estimated image in Figure 5.14b. However, the error in the subsalt images in Figure 5.19 shows that use of incorrect HCZ can harm subsalt imaging. Furthermore, pushing down the HCZ may lead to larger error in subsalt imaging than does perturbing the HCZ upward. The choice of the location of the 2D section here prevents us from determining the largest subsalt imaging error. Therefore, to further understand the influence of the erroneous HCZ, 3D or more 2D seismic imaging is desired.

5.4.2 Error in top salt

Similarly, I used for the migration the two inverted models in Figure 4.9, corresponding to the two largest top-salt perturbations tested, i.e., a constant ± 200 m in the depth of the top salt. Because this type of error arises from errors in the overburden velocity, both the top and the HCZ are shifted in the velocity model. Figure 5.20 shows the velocity models, and Figure 5.21 the migration results obtained from these models. Because the top of salt in the erroneous model is deeper than that in the correct velocity model, the top salt is imaged with erroneous velocity (the velocity of the sediments rather than that of salt). The top-salt image in Figure 5.21a is in the correct position, but it shows somewhat squeezed relief because the top salt is imaged with the background velocity. In Figure 5.21b, on the other hand, because the modeled top salt is shallower than the position in the correct velocity model, the top salt is imaged inside the modeled salt body. The image of top salt

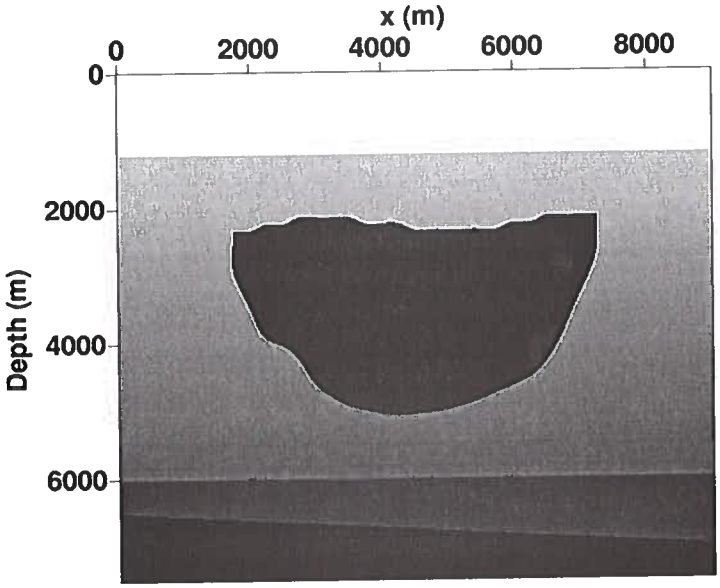

(a)

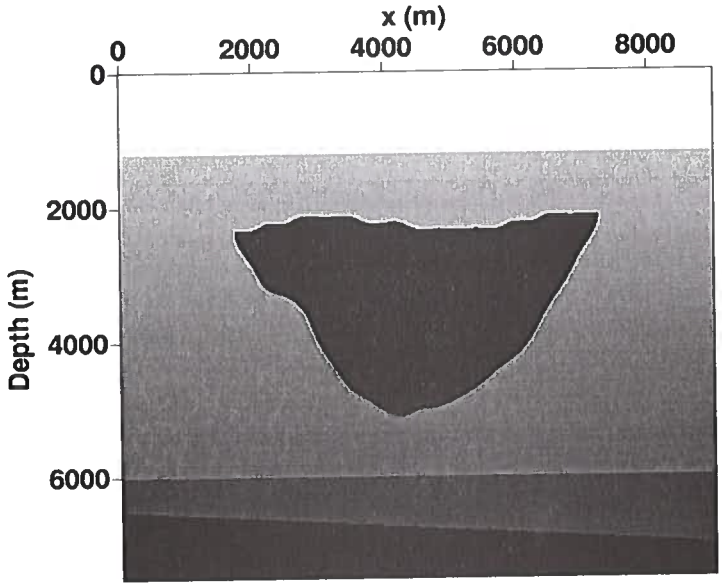

(b)

Figure 5.18. Velocity models inverted using gravity data, but with (a) +10% and (b) −10% error in the HCZ, where the maximum error of HCZ is about 400 m.

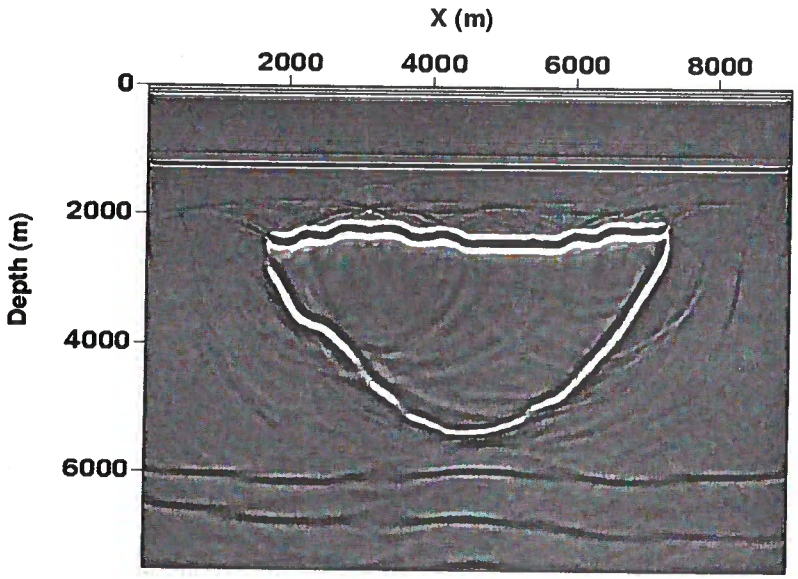

(a)

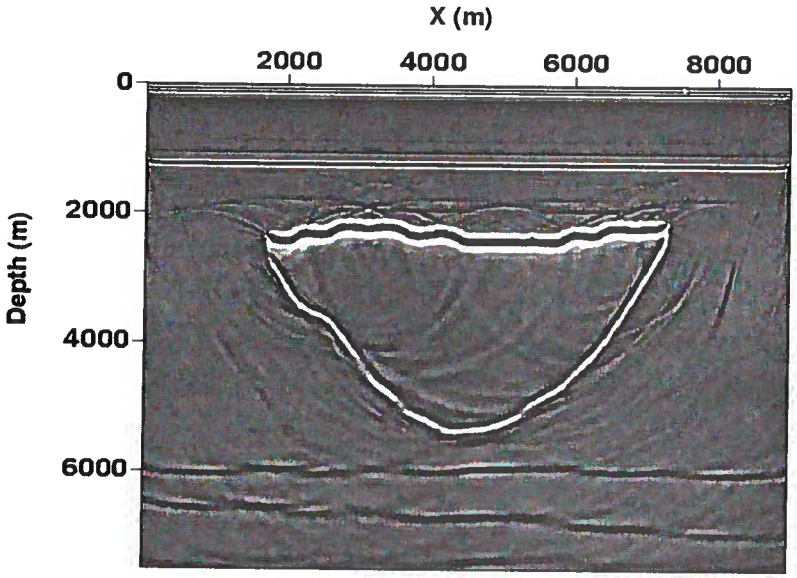

(b)

Figure 5.19. Prestack results for models having (a) +10%, and (b) −10% error in the HCZ.

is pushed down and shows smiling artifacts. Therefore, the error in the velocity model for top salt not only degrades the imaging of the base salt and beneath, but also that of the top salt itself.

Since the position of the HCZ is also erroneous, the depth of the base salt is over-estimated in Figure 5.20a and under-estimated in Figure 5.20b. In Figure 5.20a, the top salt is shifted down from the true position. This perturbation somewhat cancels out the influence on the computed traveltimes from the extra salt gained from gravity inversion. As a result, the images of the subsalt features in Figure 5.21a and 5.21b do not show significant distortion from the best-estimated image in Figure 5.14b, just a small pull-up structure in the subsalt image. Compared to the results imaged using the true velocity model, the images of subsalt features in Figure 5.21 have larger errors than in the best-estimated image in Figure 5.14b. Of importance, the 2D cross-section passes through the area in the model where errors are large in Figure 4.10. Therefore, the quality of the subsalt images in Figure 5.21 is likely poorer than we might expect elsewhere in the model. Because the 200 m is a quite large error for the top of salt in practice, the errors in subsalt imaging here are likely more severe than one may encounter in practice.

5.5 Error in density for the sedimentary section

The recovered base salt with density errors in Chapter 3 refer to those when the density contrast deviates from the true value. Because the perturbation of density is simple, i.e., constant in percentage ($\pm 10\%$ and $\pm 20\%$), the error in the recovered base salt is also simple. The cross-section chosen here passes through the area in the salt model that contains large errors attributable to error in density (see Figure 4.14). I select the migration-velocity models (see Figure 5.22) corresponding the base salt recovered when the density contrast has an error of $\pm 10\%$ of the true value (Figure 4.13). For large errors in density, the inverted base salt has huge errors, so large that the base salt almost penetrates reflector S_1 when the density contrast is 10% lower than the true value.

Since the top salt and HCZ are correctly defined, the source of error in subsalt imaging is only the inverted area of the base salt, i.e., the central part of the base salt. In Figure 5.23, note that the error concentrates in the area directly beneath the inverted area of base salt. When the density contrast is 10% lower than the true value, the extra salt gained in the base salt from gravity inversion pushes the distorted image of subsalt features deeper than the true position (Figure 5.23a). On the other hand, when the density contrast is 10% high (Figure 5.23b), a pull-up structure in the subsalt image is attributed to the missing salt. Compared with the error in base salt from gravity inversion, however, the error in subsalt imaging is again relatively much smaller. Further, although 10% error of the density contrast can well be encountered in practice, the corresponding subsalt imaging error is far larger than for results when the depth of the top salt is erroneous. Therefore, in practice, prior to the gravity inversion one should mind more the error in density than that in top salt. Because the subsalt imaging error caused by the error in the bathymetry correction or HCZ does not represent the largest error to be expected for this salt model, it is difficult to determine which is the most severe source of the subsalt imaging error in

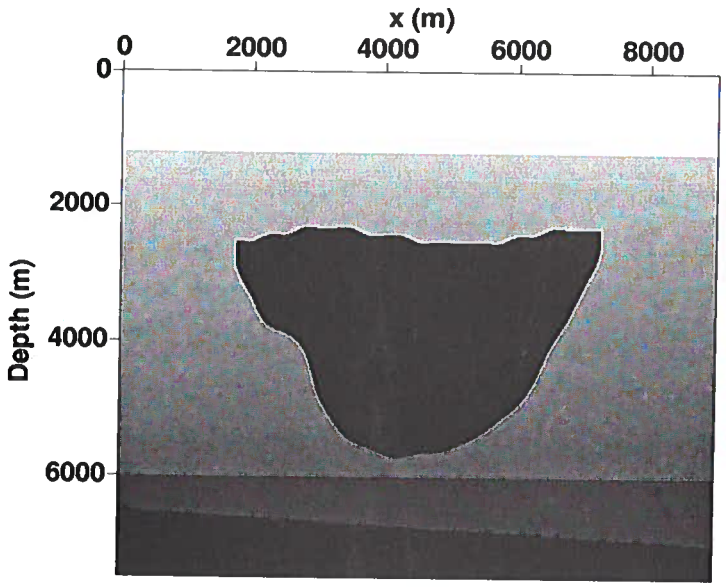

(a)

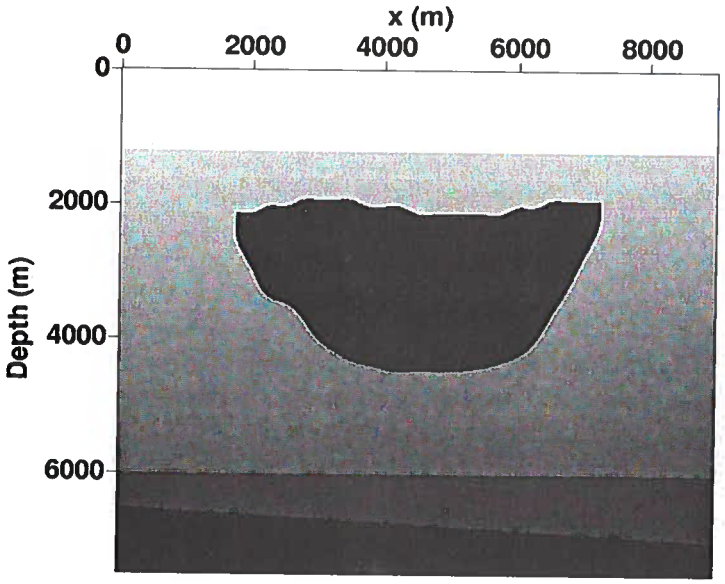

(b)

Figure 5.20. Inverted velocity models for erroneous depth of the top salt of (a) +200 m, and (b) -200 m.

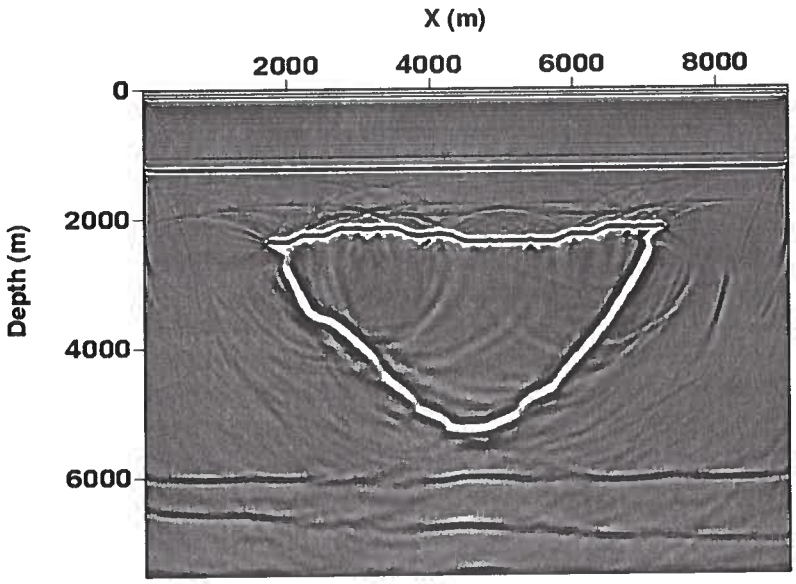

(a)

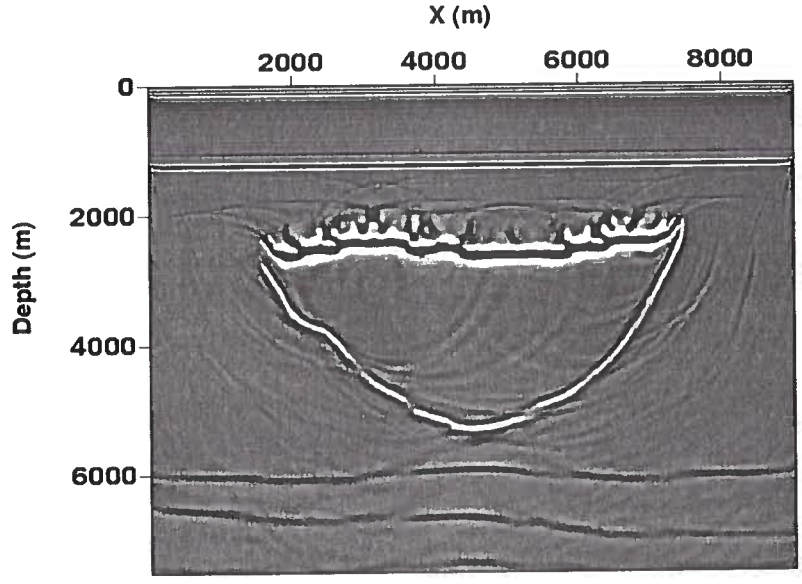

(b)

Figure 5.21. Prestack migration results based on smoothed version of the inverted models in Figure 5.20.

the three factors : bathymetry correction, HCZ, or density contrast; a 3D seismic-imaging study is desirable.

5.6 Summary

The error in subsalt imaging not surprisingly increases with the magnitude of error of the erroneously inverted base salt. Because, the error of the inverted base salt is proportional to the magnitude of the errors in the three key input factors in gravity inversion, i.e., HCZ, top salt and density, the subsalt imaging error increases with increasing error in these key factors. Large errors in the depth of base salt, however, do not necessarily imply large errors in subsalt imaging. Distortions in the images of the subsalt features are usually smaller than those in images of the base salt.

Also, one may note that the images of the subsalt features obtained with the error in bathymetry correction, HCZ, top salt, and density contain less error than that in Figure 5.14a when little information about the depth of the base salt is available from seismic data. This suggests that even with error in assumptions, gravity inversion could help the subsalt imaging; i.e., gravity inversion is robust. Since the imaging here was based on a particular 2D cross-section through the 3D salt model, the results here cannot provide general understanding about the influence of in gravity inversion. 3D imaging tests thus would be helpful.

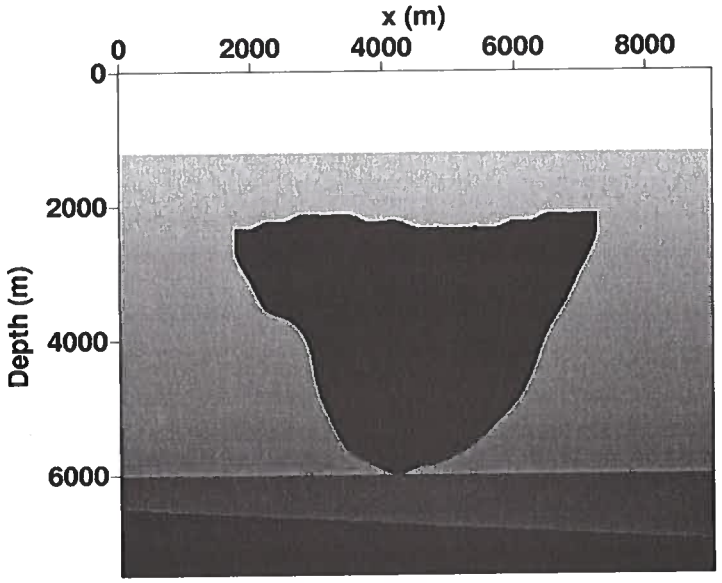

(a)

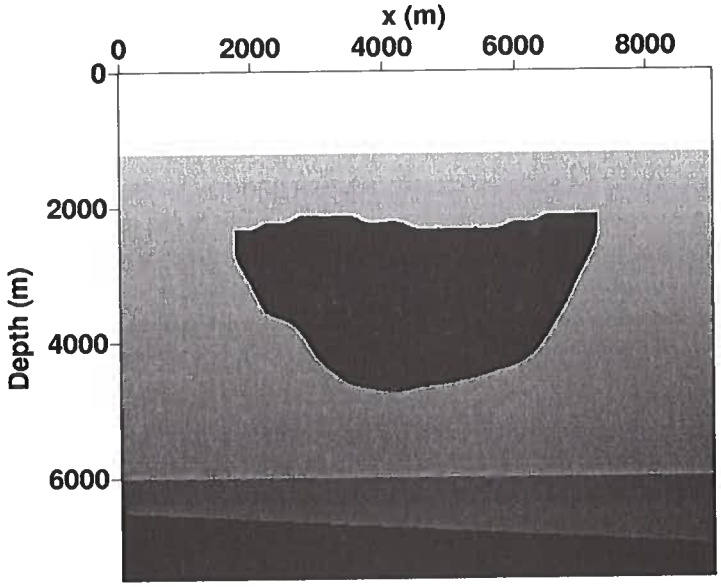

(b)

Figure 5.22. Inverted velocity models for density errors (a) +10%, and (b) −10% relative to the true density-contrast profile.

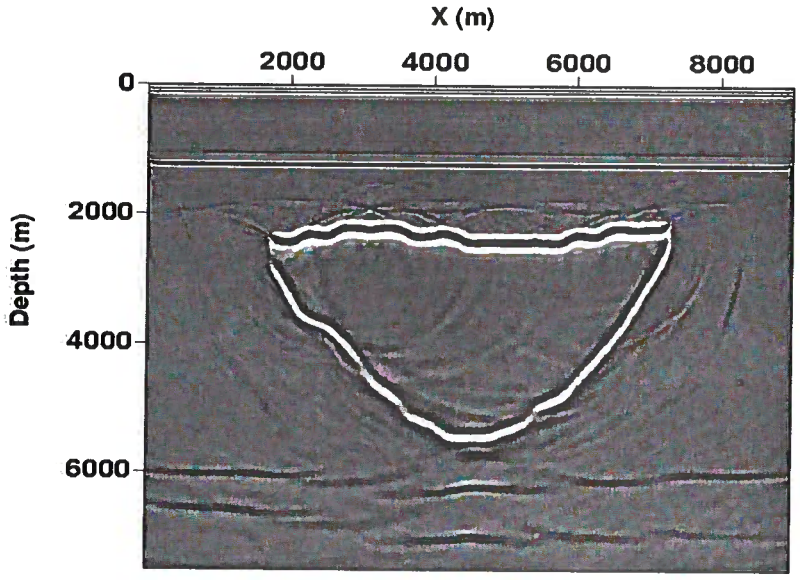

(a)

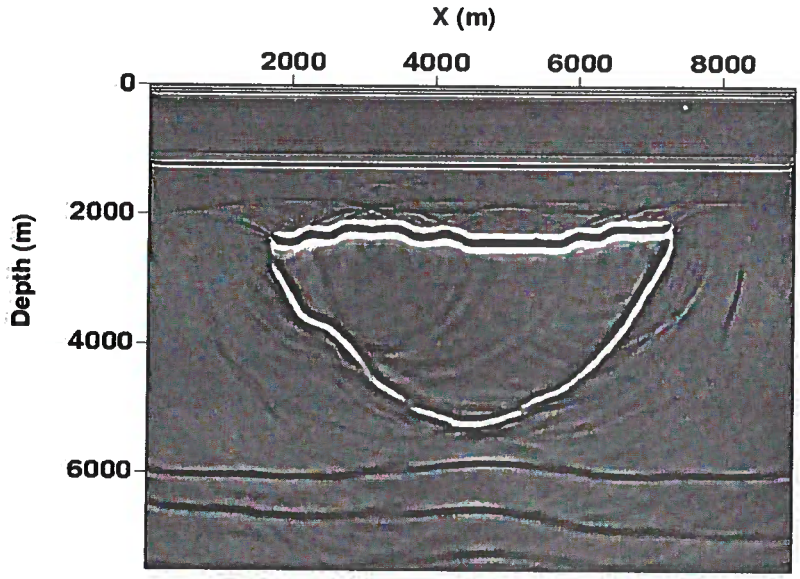

(b)

Figure 5.23. Prestack migration results corresponding to smoothed versions of the velocity models in Figure 5.22 a and 5.22 b.

Chapter 6

Discussion and conclusions

6.1 Conclusions

I have developed an algorithm for inverting gravity data to reconstruct the depth of base salt and applied the algorithm to a synthetic 3D salt model. The robustness of the algorithm derives from the use of a logarithmic parameterization and the L-curve criterion for estimating the optimal degree of regularization. The numerical experiments show that this algorithm of gravity inversion can improve the definition of the base-salt shape with use of the correct inversion parameters.

For additive uncorrelated random noise in gravity data, the standard deviation and bias of model obtained by both linearized approximation and direct evaluation increase with the noise level. The relative difference between errors in the inverted base-salt depth for different levels of data noise, however, is not so large that the uncorrelated data noise influences the inverted base salt significantly. The simulations show that small amount of correlated noise can lead to large change in the recovered base salt; thus, the recovered base salt is more sensitive to the presence of correlated noise than to that of uncorrelated noise.

I simulate the errors in prior information including the HCZ, top of salt, and density contrast. Not surprisingly, the errors in the recovered base salt increase with errors in these factors. Of more concern, small errors in these input parameters could lead to large errors in the recovered depth of base salt. Underestimating any of the three input quantities always leads to larger error in the inverted depth of base salt than does overestimating them. Thus one should avoid underestimating these model characteristics. Further, the results show that the error in the density contrast may be the most severe factor degrading the recovered depth of base salt.

I use a 2D acoustic velocity cross-section through the 3D salt model to study the influence of the inversion errors on subsalt seismic imaging. Similar to the gravity inversion, distortions in subsalt imaging increase with error in the depth of the inverted base salt. I found, however, that error in subsalt imaging is usually smaller than that of the depth of base salt. This implies that subsalt imaging may not be too sensitive to base-salt errors. Gravity inversion may help subsalt imaging as long as large-scale structures in base salt are recovered.

Moreover, it is important to understand how good gravity data need to be to aid in subsalt imaging. For this specific salt model with the reference model at fixed depth of base salt of 4000 m, the subsalt imaging error is small relative to the best image, when the standard deviation of the uncorrelated random noise in the data is 0.1 mGal. Because the

0.1-mGal standard deviation is reasonably large in practice, I conclude that uncorrelated random noise basically has no significant influence on the subsalt imaging. Second, the 200-m error in the depth of the top salt, which leads to artifacts in top-salt imaging, does not introduce severe degradation to the subsalt imaging. Since 200-m error in top salt is large in general, we can infer also that a constant shift in top salt is not a significant contributor to subsalt imaging error. For a 10% error in density contrast, the imaged subsalt features, though identifiable, have sizeable distortion. Therefore, the error in density contrast should be less than 10%. Because the cross-section does not pass through the area where the large errors in base salt are located, to determine the acceptable error in the bathymetry correction or the HCZ is difficult, and more study is desired. One also should be reminded that the choice of reference model is crucial. Different reference models lead to different quality of inversion results; e.g., if the reference model is closer to the true base salt, the error in the recovered base salt will be smaller than the results obtained here. Although the results here represent gravity inversion for just one chosen salt model, they nevertheless provide an indication of errors to be expected and serve as a guide for cases with similar salt features.

6.2 Future work

The seismic imaging in Chapter 5 is done in 2D. The results thus reflect only the influence of the erroneous inverted base salt through a 2D section. The information obtained from the tests is therefore incomplete; e.g., the influence of shadow zones may be less severe in 3D than in 2D. Study based on 3D seismic imaging could overcome this weakness and be more informative.

As shown above, the error in the inverted base-salt depth may not significantly degrade the images of subsalt features. Another factor not considered above that can influence the quality of subsalt imaging is the *shape* of the top of salt. In Figure 6.1a, while preserving the shape of the base, I perturb the shape of the top salt with a correlated Gaussian distribution. The standard deviation and the correlation radius of the perturbation are both 200 m. Applying this model in Kirchhoff migration, I obtain the image in Figure 6.1b. Because of the rugged error in top salt, both the base salt and the subsalt reflectors are poorly imaged, more so than in any of the previous tests in this thesis. One can hardly interpret the base salt and the subsalt features directly beneath the salt body. Clearly, even with the correct shape of the base salt, errors in top salt can lead to severe degradation in migrated images of the base salt and subsalt. One therefore needs to recover both the top salt and the base salt with some accuracy. A possible approach is to use gravity data and gravity gradiometry data to invert the top and base of salt iteratively. Compared with gravity data, gravity gradiometry data have higher resolution, and faster decay in dependence on the depth; therefore they are less sensitive to a deep base salt as to a shallower top salt. Given an initial guess for the base salt, one can first invert for the top salt using gravity gradiometry data using the algorithm derived above, but with an appropriately changed sensitivity matrix. Then, using the recovered top salt, a second inversion can invert for the base salt using gravity data. The two steps can be repeated using the results from the previous inversion until the model converges.

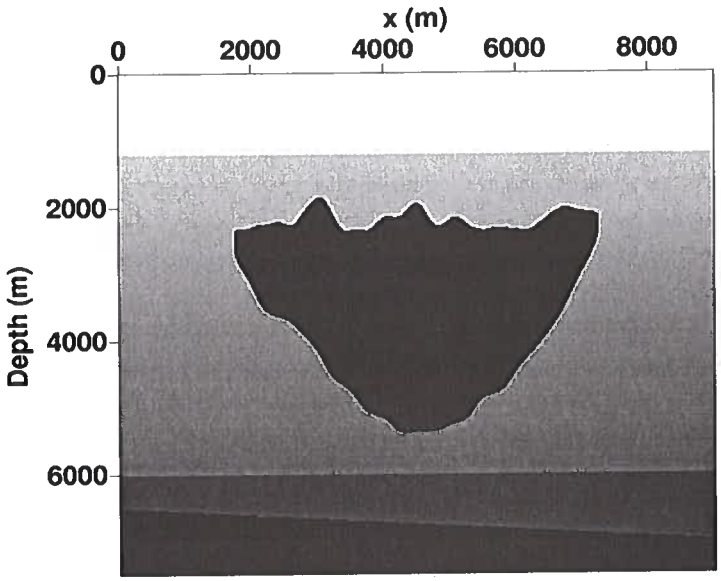

(a)

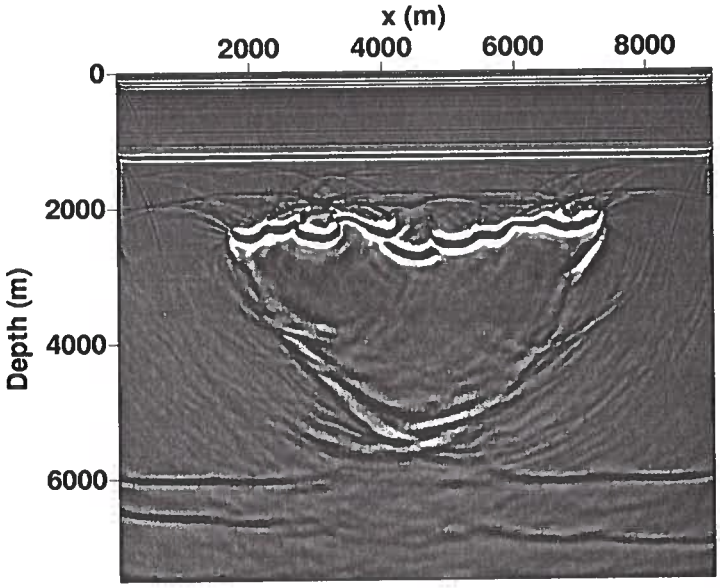

(b)

Figure 6.1. (a) Velocity model with spatially correlated perturbation to the shape of the top salt by Gaussian random noise having standard deviation of 200 m, and (b) prestack migration result. The shape of top salt in (a) is more rugose than that in Figure 5.2.

Bibliography

Alumbaugh, D. L. and Newman, G. A., 2000, Image appraisal for 2-D and 3-D electromagnetic inversion: Geophysics, 65, 1455-1467.

Albertin, U., Kapoor, S. (Jerry), Chang, W. and Beals, R., 1998, Velocity resolution and salt boundary placement in subsalt imaging, 68rd Ann. Internat. Mtg: Soc. of Expl. Geophys., 1301-1304.

Alford, R., Kelly, K., and Boore, D., 1974, Accuracy of finite difference modeling of the acoustic wave equation: Geophysics, 39, 834-842.

Aminzadeh, F., Burkhard, N., Nicoletis, L., Rocca, F., Wyatt, K., 1994, SEG/EAGE 3-D modeling project: 2nd update: The Leading Edge, 13, 949-952.

Clarke, G. K. C., 1969, Optimum second-derivative and downward continuation filters: Geophysics, 34, 424-437.

Dejong, H., Al-Kindy, I., and Biegert, E., 2000, Gravity-gradient data integrated in prestack depth migration in the southern north sea, Shell U.K. Exploration and Production.

Dianne P. O'Leary, 1996, Conjugate gradients and related KMP algorithms: The beginnings, in linear and nonlinear conjugate gradient-related methods, Loyce Adams and J. L. Nazareth, eds., SIAM, Philadelphia, 1-8.

Easley, D. H., Borgman, L. E. and Shive, P. N., 1990, Geostatistical simulation for geophysical applications - Part I: Simulation: Geophysics, Soc. of Expl. Geophys., 55, 1435-1440.

Fei, T., 1994, Elimination of numerical dispersion in finite-difference modeling and migration by flux-corrected transport: Ph.D. thesis, Colorado School of Mines.

Gardner, G. H. F., Gardner, L.W., and Gregory, A.R., 1974, Formation velocity and density - the diagnostic basics for stratigraphic traps: Geophysics, 39, 770-780.

Golub, G. and Van Loan, C., 1989, Matrix computations, second edition, The Johns Hopkins University Press.

Hansen, P. C., 1992, Analysis of discrete ill-posed problems by means of the L-curve, SIAM Review, 34, 561, 580.

Jorgensen, G. and Kisabeth, J., 2000, Joint 3-D inversion of gravity, magnetic, and tensor gravity fields for imaging salt formations in the deepwater Gulf of Mexico, 70th Ann. Internat. Mtg: Soc. of Expl. Geophys., 424-426.

Kelly, K., Ward, R., Treitel, S., and Alford, R., 1976, Synthetic seismograms: a finite-difference approach: Geophysics, 41, 2-27.

Kim, H, Song, Y., and Lee, K., 1999, Inequality constraint in least-squares inversion of geophysical data. Earth Planet Space, Vol. 51, No. 2, 255-259.

Lawson, C. L. and Hanson, R. J., 1974, Solving least-squares problems, Prebtice-Hall, Englewood Cliffs, NJ.

Li, Y., and Oldenburg, D. W., 1999, 3-D Inversion of DC resistivity data using an L-curve criterion: 69th Ann. Internat. Mtg., Soc. Expl. Geophys., Expanded Abstracts, 251-254.

Li, Y., and Oldenburg, D. W., 1999, Estimating depth of investigation in dc resistivity and IP survey: Geophysics, 64, 403-416.

Li, Y. and Oldenburg, D. W., 1998, 3-D Inversion of gravity data: Geophysics, 63, 109-119.

Li, Y., and Oldenburg, D. W., 1996, 3-D Inversion of magnetic data: Geophysics, 61, 394-408.

Liu, Z., 1995, Migration velocity analysis: Ph.D. thesis, Colorado School of Mines.

Liu, Z., 1994, A velocity smoothing technique based on damped least squares: in Project Review, May 10, 1994, Consortium Project on Seismic Inverse Methods for Complex Structures, CWP-153.

Liu, Z., 1993, A Kirchoff approach to seismic modeling and pre-stack depth migration: 63rd Ann. Internat. Mtg: Soc. of Expl. Geophys., 888-891.

Menke, W., 1984, Geophysical data analysis: Discrete inverse theory: Academic Press, Inc.

Muerdter, D. R., Lindsay, R. O. and Ratcliff, D. W., 1996, Imaging under edges of salt sheets: A raytracing study, 66th Ann. Internat. Mtg: Soc. of Expl. Geophys., 578-580.

Muerdter, D. R. and Ratcliff, D. W., 2000, Subsalt illumination determined by raytrace modeling: a catalog of seismic amplitude distortion caused by various salt shape: Internet.

Muerdter, D. R. and Ratcliff, D. W., 2001, Understanding subsalt illumination through raytrace modeling, Part 1: Simple 2-D salt models: The Leading Edge, June 2001.

Murray W., Overton M.L., 1979, Steplength algorithms for minimizing a class of nondifferentiable functions, Computing, 23, 309-331.

Oldenburg, D. W. and Li, Y., 1994, Inversion of induced polarization data: Geophysics, 59, 1327-1341.

Reamer, K. S. and Ferguson, F. J., 1989, Regularized two-dimensional Fourier gravity inversion method with application to the Silent Canyon caldera, Nevada: Geophysics, 54, 486-496.

Routh, P., Kisabeth, J. and Jorgensen, G., 2001, Base of the salt imaging using gravity and tensor gravity data, 71st Ann. Internat. Mtg: Soc. of Expl. Geophys., 1482-1484.

Scales, J., and Snieder, R., 1997, To Bayes or not to Bayes: Geophysics, 62, 1045-1046.

Sen, V., Wagner, D., Etgen, J., Rietveld, W., Fei, T., Truxillo, M., Stauber, D., Harrison, H. and Mozer, E., 2000, Velocity analysis using prestack depth migration and 3-D tomography: A case study over steeply dipping salt, 70th Ann. Internat. Mtg: Soc. of Expl. Geophys., 717-720.

Starich, P. J., Lewis, G. G., Faulkner, J., Standley, P. G. and Setterquist, S., 1994, Integrated geophysical study of an onshore salt dome: The Leading Edge, 13, no. 08, 880-884.

Talwani, M. and Kessinger, W. P., 1995, 3-D velocity model building: Defining base of salt by inverting gravity data, 65th Ann. Internat. Mtg: Soc. of Expl. Geophys., 263.

Tarantola, A., 1987, Inverse Problem Theory. Elsevier, New York.

Tikhonov A. N., and Arsenin, V. Y., 1977, Solutions of ill-posed problems, John Wiley, New York, 1977.

Wiggins, A. R., Larner, L. K., and Wisecup, D. R., 1976, Residual statics analysis as a general linear inverse Problem: Geophysics, 41, 922-938.

website: fttp://www.geop.ubc.ca/ubcgif/tutorials/invtutorial/numsol.html

Appendix A

Linearized approximation of standard deviation

Tarantola (1987) gives the covariance matrix of a nonlinear system, which could be linearly solved in the vicinity of a model. He, however, did not present the derivation. In the following, I show how to derive the covariance matrix for such a system.

For the general nonlinear inversion problem shown in equation (3.1), if the model could be resolved linearly in the maximum *a posterior* probability (MAP) model as $\vec{m}_{MAP}$, i.e., in another words when $\vec{m}$ is linearly close to $\vec{m}_{MAP}$, we have

$$F(\vec{m}) \cong F(\vec{m}_{MAP}) + G_{MAP}(\vec{m} - \vec{m}_{MAP}), \tag{A.1}$$

where G_{MAP} is the sensitivity matrix, evaluated at $\vec{m}_{MAP}$. Substituting equation (A.1) into (3.2) yields

$$\begin{aligned}\phi(\vec{m}) \cong & \left(F(\vec{m}_{MAP}) - \vec{d} + G_{MAP}(\vec{m} - \vec{m}_{MAP})\right)^T C_d^{-1} \left(F(\vec{m}_{MAP}) - \vec{d} + G_{MAP}(\vec{m} - \vec{m}_{MAP})\right) \\ & + (\vec{m} - \vec{m}_0)^T C_m^{-1} (\vec{m} - \vec{m}_0) \\ = & \left((G_{MAP}\vec{m}_{MAP} - F(\vec{m}_{MAP}) + \vec{d}) - G_{MAP}\vec{m}\right)^T \\ & C_d^{-1} \left((G_{MAP}\vec{m}_{MAP} - F(\vec{m}_{MAP}) + \vec{d}) - G_{MAP}\vec{m}\right) + (\vec{m} - \vec{m}_0)^T C_m^{-1} (\vec{m} - \vec{m}_0)\,.\end{aligned} \tag{A.2}$$

For convenience, let $\vec{d}' = G_{MAP}\vec{m}_{MAP} - F(\vec{m}_{MAP}) + \vec{d}$, (A.2) becomes

$$\phi(\vec{m}) = (\vec{d}' - G_{MAP}\vec{m})^T C_d^{-1} (\vec{d}' - G_{MAP}\vec{m}) + (\vec{m} - \vec{m}_0)^T C_m^{-1} (\vec{m} - \vec{m}_0)\,. \tag{A.3}$$

Equation (A.3) is a linear system, and according to Tarantola (1987), the *a posterior* prob-

ability density of the model is a Gaussian centered at

$$\begin{aligned}\vec{m}' &= \vec{m}_0 + \left(G_{MAP}C_d^{-1}G_{MAP} + C_m^{-1}\right)^{-1} G_{MAP}^T C_d^{-1}\left(\vec{d} - G_{MAP}\vec{m}_0\right) \\ &= \vec{m}_0 + \left(G_{MAP}C_d^{-1}G_{MAP} + C_m^{-1}\right)^{-1} G_{MAP}^T C_d^{-1} \\ &\left(G_{MAP}\vec{m}_{MAP} - F(\vec{m}_{MAP}) + \vec{d} - G_{MAP}\vec{m}_0\right) \\ &= \vec{m}_0 + \left(G_{MAP}C_d^{-1}G_{MAP} + C_m^{-1}\right)^{-1} G_{MAP}^T C_d^{-1} \\ &\left((\vec{d} - F(\vec{m}_{MAP})) + G_{MAP}(\vec{m}_{MAP} - \vec{m}_0)\right),\end{aligned} \tag{A.4}$$

and the covariance matrix is given by

$$C_M = \left(G_{MAP}^T C_D^{-1} G_{MAP} + C_m^{-1}\right)^{-1}, \tag{A.5}$$

such that,

$$\phi(\vec{m}) = C \cdot (\vec{m} - \vec{m}_{MAP})^T C_M^{-1} (\vec{m} - \vec{m}_{MAP}), \tag{A.6}$$

where C is a constant. Meanwhile, equation (2.27) in Chapter 2 gives the model perturbation in the $(k+1)$th iteration and we can rewrite the recovered model in the $(k+1)$th iteration as

$$\vec{m}^{(k+1)} = \vec{m}^{(k)} + (G_k^T C_d^{-1} G_k + C_m^{-1})^{-1}\left[G_k^T C_d^{-1}(\vec{d} - F(\vec{m}_k) + C_m^{-1}(\vec{m}_0 - \vec{m}^{(k)})\right], \tag{A.7}$$

where $C_m^{-1} = \beta W^T W$ and $C_d^{-1} = W_d^T W_d$. Manipulating equation (A.7), we obtain (Tarantola, 1987)

$$\vec{m}^{(k+1)} = \vec{m}_0 + (G_k^T C_d^{-1} G_k + C_m^{-1})^{-1} G_k^T C_d^{-1}\left((\vec{d} - F(\vec{m}_k) + G_{MAP}^{-1}(\vec{m}_0 - \vec{m}^{(k)})\right). \tag{A.8}$$

Suppose, for certain k, we have reached the MAP model in the $(k+1)$th iteration, i.e., $\vec{m}^{(k+1)} = \vec{m}_{MAP}$; then we have

$$\vec{m}^{(k+1)} \cong \vec{m}^{(k)}. \tag{A.9}$$

In another word,

$$G_k \cong G_{K+1} = G_{MAP}. \tag{A.10}$$

Substituting equation (A.10) into equation (A.8), one notes that $\vec{m}^{(k+1)}$ is exactly the same as $\vec{m}'$ in (A.4). Hence, the model is centered at the $\vec{m}_{MAP}$ solution and the covariance matrix is

$$C_M = \left(G_{MAP}^T C_D^{-1} G_{MAP} + C_m^{-1}\right)^{-1}. \tag{A.11}$$

Appendix B

Linearized approximation of bias

Suppose in the $(k+1)$th iteration, we reach the best model for equation (3.2), such that

$$\delta\vec{m}^{(k+1)} = 0. \tag{B.1}$$

According to Tarantola (1987), the recovered perturbation in the $(k+1)$th iteration satisfies

$$(G^T C_d^{-1} G + C_m^{-1})\delta\vec{m}^{(k+1)} = G^T C_d^{-1}(\vec{d} - F(\vec{m}^{(k)})) + C_m^{-1}(\vec{m}_0 - \vec{m}^{(k)}). \tag{B.2}$$

Substituting equation (B.1) in equation (B.2) yields

$$G^T C_d^{-1}(\vec{d} - F(\vec{m}^{(k)})) = C_m^{-1}(\vec{m}^{(k)} - \vec{m}_0). \tag{B.3}$$

Adding $G^T C_d^{-1} G(\vec{m}^{(k)} - \vec{m}_0)$ to both sides of equation (B.3), we have

$$\begin{aligned} &G^T C_d^{-1}(\vec{d} - F(\vec{m}^{(k)})) + G^T C_d^{-1} G(\vec{m}^{(k)} - \vec{m}_0) = C_m^{-1}(\vec{m}^{(k)} - \vec{m}_0) + G^T C_d^{-1} G(\vec{m}^{(k)} - \vec{m}_0) \\ &\Rightarrow G^T C_d^{-1}\left(\vec{d} - F(\vec{m}^{(k)}) + G(\vec{m}^{(k)} - \vec{m}_0)\right) = \left(G^T C_d^{-1} G + C_m^{-1}\right)(\vec{m}^{(k)} - \vec{m}_0). \end{aligned}$$

Assuming $\vec{d} \cong F(\vec{m}_{true}) \cong F(\vec{m}^{(k)}) + G(\vec{m}_{true} - \vec{m}^{(k)})$, we have

$$\begin{aligned} \Rightarrow G^T C_d^{-1}&\left(F(\vec{m}^{(k)}) + G(\vec{m}_{true} - \vec{m}^{(k)}) - F(\vec{m}^{(k)}) + G(\vec{m}^{(k)} - \vec{m}_0)\right) \\ &= \left(G^T C_d^{-1} G + C_m^{-1}\right)(\vec{m}^{(k)} - \vec{m}_0) \\ \Rightarrow G^T C_d^{-1}&\left(G(\vec{m}_{true} - \vec{m}_0)\right) = \left(G^T C_d^{-1} G + C_m^{-1}\right)(\vec{m}^{(k)} - \vec{m}_0) \\ \Rightarrow (\vec{m}_k - \vec{m}_0) &= \left(G^T C_d^{-1} G + C_m^{-1}\right)^{-1} G^T C_d^{-1} G(\vec{m}_{true} - \vec{m}_0). \end{aligned}$$

Subtracting $(\vec{m}_{true} - \vec{m}_0)$ on both sides yields

$$\vec{m}^{(k)} - \vec{m}_{true} = \left[\left(G^T C_d^{-1} G + C_m^{-1}\right)^{-1} G^T C_d^{-1} G - I\right](\vec{m}_{true} - \vec{m}_0), \tag{B.4}$$

where G is the sensitivity matrix. Assuming $\vec{m}^{(k)}$ is close enough to the MAP model, equation (B.4) gives the estimation of bias, and $\left[\left(G^T C_d^{-1} G + C_m^{-1}\right)^{-1} G^T C_d^{-1} G\right]$ is the resolution matrix.